Microjet Impingement Cooling of High Power-Density Electronics

by

ENS Stephen Michael Walsh, USN

B.S. Mechanical Engineering
United States Naval Academy, 2016

Submitted to the Department of Mechanical Engineering
in partial fulfillment of the requirements for the
Degree of Master of Science in Mechanical Engineering
at the
MASSACHUSETTS INSTITUTE OF TECHNOLOGY
June 2018

Author .....
Department of Mechanical Engineering
May 11, 2018

Certified by .....
Dr. Bernard A. Malouin Jr.
Technical Staff in Structural and Thermal-Fluids Engineering, MIT Lincoln Laboratory
Thesis Supervisor

Certified by .....
Professor Evelyn N. Wang
Gail E. Kendall Professor, Department of Mechanical Engineering
Thesis Supervisor

Accepted by .....
Rohan Abeyaratne
Chairman, Department Committee on Graduate Theses

Microjet Impingement Cooling of High Power-Density Electronics

by

ENS Stephen Michael Walsh, USN

Submitted to the Department of Mechanical Engineering on May 11th, 2018
in Partial Fulfillment of the Requirements for the
Degree of Master of Science in Mechanical Engineering

Abstract

The increasing power density of advanced electronics, and in particular Gallium Nitride (GaN) high electron mobility transistors (HEMTs) in RF power amplifiers, represents a major challenge in thermal management. Reducing the operating temperature, by means of effective cooling, improves both the performance and lifetime of the device. In this work, the high heat transfer capability of microjet impingement was leveraged to bring cooling directly to the backside of the electronic device. Previous experimental studies characterized the effects of geometrical factors, such as diameter, pitch, and standoff, on heat transfer performance. Insights from these studies were used to design a square array of sixteen 100 μm jets and a circular array of nineteen 116 μm jets. These designs were then built using standard silicon micro-fabrication techniques and bonded to an integrated heater, which matched the heat generation profile of a HEMT device. A fully conjugate numerical model of the fluid dynamics and heat transfer in COMSOL Multiphysics allowed for visualization of the fluid flow within the assembly. The model was used to predict heat transfer coefficients of over 250 kW/m^2-K, showing strong agreement with correlations in the microjet literature. Integration of the microjet device into a closed flow loop demonstrated modest total flow rates and pressure drops. The microjet performance was then characterized using a free space micro-Raman thermography system with spatial resolution of 1 μm. For the first time, two-dimensional scans of a device under power were taken with jet impingement cooling on the backside. The micro-Raman thermography measurements confirmed heat transfer coefficients of 250 kW/m^2-K on a device with a heat flux of 5500 W/cm^2 and a temperature rise of 46 ± 2 °C. In this thesis, practical concerns including microjet orifice clogging and backside erosion were answered through completion of a 1000-hour extended lifetime test. This thesis provides both numerical and experimental research demonstrating the impact of microjet impingement cooling and high spatial resolution micro-Raman thermography.

Thesis Supervisor: Bernard A. Malouin Jr.
Title: Technical Staff in Structural and Thermal-Fluids Engineering, MIT Lincoln Laboratory

Thesis Supervisor: Evelyn N. Wang
Title: Gail E. Kendall Professor, Department of Mechanical Engineering

Acknowledgments

This thesis was prepared at MIT Lincoln Laboratory[1], specifically with the JETS team in the Structural and Thermal-Fluids Engineering Group. Working with the JETS team was a highlight of my graduate school experience, and I truly looked forward to our weekly meetings. Bernie Malouin went above and beyond as my thesis co-supervisor. He provided much of the guidance and vision for what is included in this thesis. Eric Browne contributed greatly to my understanding of microjets and provided help with the experimental setup. Jim Smith helped with my understanding of CFD modeling and with preparing papers for publication. Tim Hennighausen helped with instrumenting the flow loop and collecting data during the 1000-hour testing. This work would not have been possible without the help and time of everyone on the team; thank you for being good mentors. I would also like to thank Donna Yost and the Lincoln Lab Microelectronics Laboratory, who fabricated the devices used in the testing.

I would like to thank Evelyn Wang, who served as my thesis co-supervisor and included me in her lab group (the DRL- Device Research Lab) for the past two years. Evelyn, through her leadership and passion for research, has cultivated an innovative and welcoming research group culture, and I learned a lot both from her and from the other members of the DRL. In particular, Kevin Bagnall provided important guidance at the start of the Lincoln Lab-campus collaboration. He also designed and built the free-space micro-Raman thermography setup used for measurements in this thesis. Lenan Zhang helped with my understanding of the micro-Raman technique and with experimental troubleshooting.

I am incredibly grateful that the Navy allowed me the opportunity to pursue my master's degree through the Immediate Graduate Education Program. Graduate school has been a period of tremendous growth, and it has changed the way I approach research, technical problems, and learning in general.

I would not have had such a great graduate school experience without my friends and family. The friends I made in Boston helped make time away from research quite enjoyable. I value these friendships immensely, except on Army-Navy or Navy-Air Force game days. Lastly, my family has been an endless source of grounding and support.

Stephen M. Walsh, ENS USN 11 May 2018

[1] DISTRIBUTION STATEMENT A. Approved for public release. Distribution is unlimited.

This material is based upon work supported by the Assistant Secretary of Defense for Research and Engineering under Air Force Contract No. FA8702-15-D-0001. Any opinions, findings, conclusions or recommendations expressed in this material are those of the author(s) and do not necessarily reflect the views of the Assistant Secretary of Defense for Research and Engineering.

Table of Contents

List of Figures

List of Tables

1. Introduction

Improvement in the materials, processes, and designs of semiconductors over the past several decades has led to the shrinking of device characteristic dimensions from micrometers to nanometers. These advancements have resulted in a high density of transistors, which serve both logic and power functions. At the die level, transistor power dissipation can result in localized hot spots with length scales of only a few micrometers, in which the power density can reach 5 to 10× the average die power density [1]. The peak temperatures experienced in these localized hot spots impact performance and reliability of the device. Thermal considerations have become a limiting factor in both the initial implementation and continued operation of devices. As a result, new cooling technologies and experimental measurement techniques have been developed to meet these challenges.

1.1. High power devices

Central to the hardware advances that have enabled the technological progress of the last few decades is the transistor. Transistors are the essential element in logic applications, power conversion, and RF power amplification. Moore's Law states that the number of transistors that can be placed on an integrated circuit chip will double every two years [2]. This higher packing density has revolutionized the microprocessor industry allowing faster and smaller devices. Over the past half century, a multibillion-dollar semiconductor industry has been built around silicon (Si) technology. Moore's Law scaling with silicon fabrication technology has continued to present day, with the recent announcement of the 5 nm transistor [3].

New semiconductor materials offer improved material properties for certain high-power and high-frequency applications, such as radio frequency (RF) and microwave communication systems, radar installations, and automotive power switching. One such class of materials is termed wide bandgap, due to the higher bandgaps (2-4 eV) compared with that of Si (1.1 eV). These materials include silicon carbide (SiC) and gallium nitride (GaN), an alloy from groups III and V in the periodic table. The relevant material properties for Si, gallium arsenide (GaAs), SiC, and GaN are summarized below in Table 1.1. Of particular note, the wide bandgap energies are roughly 3x that of Si and the breakdown electric fields are an order of magnitude higher than Si, enabling higher power operation. The comparable electron mobility and higher saturation velocity enables high-frequency operation, an important characteristic in RF power applications [4]. Lastly, the higher thermal conductivities, which can be enhanced when grown on certain substrates, of the wide bandgap materials result in improved thermal spreading.

Table 1.1: Semiconductor material properties, adapted from [5] and [6].

Material Property	Units	**Si**	**GaAs**	**4H-SiC**	**GaN**
Bandgap	eV	1.10	1.42	3.2	3.4
Breakdown electric field	MV m^{-1}	30	40	200	330
Electron mobility	cm^2 V^{-1} s^{-1}	1300	5000	260	1500
Saturated electron velocity	m/s	1.0 x 10^5	1.0 x 10^5	2.0 x 10^5	1.5 x 10^5
Thermal conductivity	W m^{-1} K^{-1}	150	50	450	130-170

A specific subset of transistors in which wide bandgap materials are making an impact is the high electron mobility transistor (HEMT), also known as a hetero-structure field effect transistor (HFET). GaN HEMTs are used in monolithic microwave integrated circuits (MMICs), which are operated in the microwave frequency range for RF power amplification, signal mixing, and power switching [7-8]. A multifingered HEMT layout is shown in Figure 1.1a. Multifingered HEMTs are often used instead of single finger HEMTs to avoid signal transmission losses and minimize magnetic time delays [6]. The main components of the HEMT are the source (S), drain (D), and gate (G). Current flows from the source fingers to the drain fingers and is modulated by voltage applied to the gate fingers. The important geometrical features are the gate length (L_G), gate width (L_W), and gate-to-gate pitch (L_P).

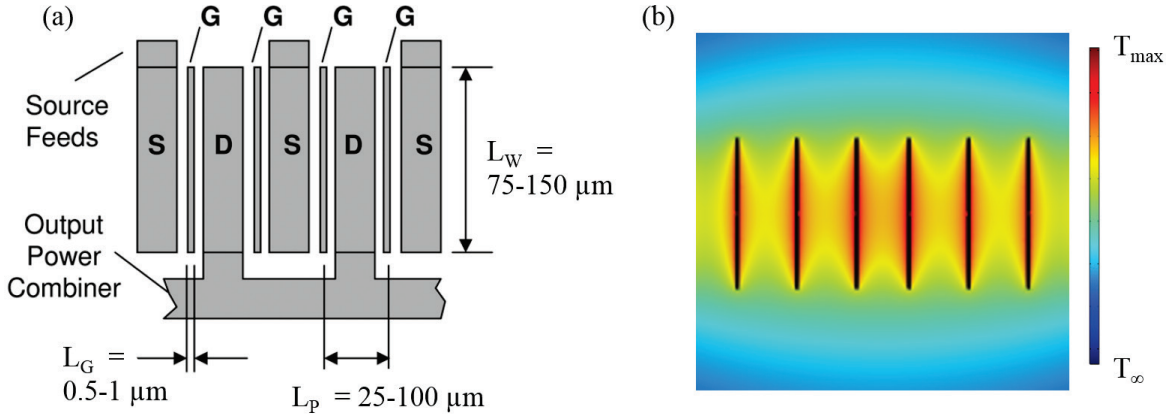

Figure 1.1: (a) Geometry of a HEMT, adapted from [9]. (b) Simulation (from this work) of the characteristic thermal profile for a HEMT geometry with heat flux applied to the gate fingers.

The majority of electrical dissipation in a multifingered HEMT device occurs in the immediate vicinity of the gate fingers. To model GaN HEMT heat generation, a constant heat flux is applied to the area (L_G x L_W) of each gate finger, as will be explained in detail in Chapter 3. The effects of this highly localized heat flux are seen in the surface temperature profile of a HEMT model in Figure 1.1b. The characteristic thermal profile shows the local maximum temperatures located in the gate finger regions. Of note, an effect known as thermal crosstalk in multifinger HEMTs, refers to the maximum temperatures occurring at the fingers near the center of the device and decreasing at the outer fingers. Due to thermal spreading, there are steep temperature gradients in the regions in between neighboring fingers. Recently, linear power densities of

over 40 W/mm of gate length have been demonstrated in the literature, resulting in temperature rises of several hundred degrees [10]. Albrecht et al. showed that the electron mobility in GaN decreased significantly as the temperature increased from 300 K to 600 K [11]. The increased operating temperature, as a result, decreases performance parameters such as the power gain and power added efficiency (PAE) [12-13]. Ditri et al. showed that by decreasing thermal resistance, and thus lowering the operating temperature, power gain increased 4.2 dB and PAE increased 3x [14].

Additionally, an active area of research within the GaN electronics community is reliability during extended DC and RF testing [15-16]. Various researchers have studied degradation drivers (such as voltage, temperature, and device geometry) that result in GaN HEMT failure [17-18]. One metric that manufacturers of GaN have used to quantify reliability is the mean time to failure (MTTF) at a specific operating temperature, where the failure criterion is defined as a 15% reduction in drain current. The manufacturer performs testing at an elevated temperature and uses it to predict the lifetime of the device at a normal operating temperature. TriQuint reported a MTTF of 1 x 10^7 hours at 150 °C, Cree reported 1 x 10^6 hours at 175 °C, RFMD reported greater than 10^6 hours at 200 °C, and Nitronex reported greater than 10^7 hours at 200 °C [16]. The variation between the reported failure temperatures could be due to the temperature method measurements used by the manufacturers. As will be highlighted later in this chapter, and throughout this thesis, current temperature measurement techniques, such as IR thermography, are limited by their spatial resolution. As a result, the measured temperature represents a spatially averaged value and most likely under predicts the true peak temperature driving the device to failure [19].

Increasing power density levels in HEMT devices has elicited the need for novel methods of cooling, which reduces thermal resistance and lowers operating temperatures. This cooling can preserve gate temperatures below 150-200 °C for extended device reliability. Equally as important, the lower operating temperatures improve RF performance, with evidence of higher power gain and power added efficiency at lower temperatures. Lastly, the decreased size scale of HEMTs has demonstrated the need for localized cooling and high spatial resolution (1-2 μm) experimental temperature techniques to understand device self heating and characterize the performance of the cooling system.

1.2. Cooling Techniques

1.2.1. Extreme Heat Density Cooling

The conventional heat rejection strategy to cool electronic components has relied on thermal conduction and spreading through multiple layers, including the substrate and material interfaces [20]. The heat is eventually dissipated through a large air heat sink or a cold plate. This cooling structure limits the operation

of the device to certain power levels, frequency bands, or duty cycles. Additionally, this conventional cooling architecture composes a significant portion of the Size, Weight, and Power (SWaP) of the system.

State-of-the-art electronics cooling solutions use liquid cooling to dissipate large amounts of heat, due to higher heat transfer coefficients with forced convection of liquids than those achieved with natural convection of free air or current liquid cold plate technologies. Two primary methods exist within forced liquid cooling to cool electronic devices: microchannels and jet impingement. Microchannels were first introduced by Tuckerman and Pease in 1981 for cooling very-large scale integrated (VLSI) circuits with a power density of 790 W/cm^2 [21]. By definition, microchannels are fluid passages with hydraulic diameters of less than 1 mm and often have channel dimensions of 100-200 μm, achieving a high surface area to volume ratio. As with fluid flow in most passages, transport properties and processes in channels improve at microscale dimensions [22]. In addition to improving convective heat transfer coefficients, microchannels can be packaged in minimal SWaP heat sinks and require low coolant supply due to the small passage diameter.

Jet impingement has been used for several decades for high heat flux applications such as turbine cooling and quenching metals, and it has recently been applied for cooling electronic components [23]. In jet impingement, a stream of fluid or gas interacts with a solid surface to transfer heat or mass. Jet impingement offers extremely high heat transfer coefficients, particularly at the stagnation point where the jet centerline intersects the heated surface. Similar to the observation in microchannels, scaling down the jet geometry generally results in higher heat transfer coefficients. Several parameters affect the heat transfer performance including jet diameter, standoff distance and center-to-center distance when used in an array. Chapter 2 will include an extensive review of microjet experimental investigations of the impact of these geometrical parameters on heat transfer performance.

Compared to microchannels, jet impingement offers higher average heat transfer coefficients. In addition, jet impingement also requires lower pressure drops compared to those required for microchannels. Another drawback of microchannels is that they can induce large temperature gradients in the direction of flow, due to the heating of fluid along the channel length. A disadvantage of jet impingement is that it can induce large temperature gradients radially outward from the impingement region. This effect, however, can be minimized through the use of multiple jets in array configurations [24].

Current approaches to extreme high heat flux cooling also include two-phase solutions. Phase-change solutions take advantage of the latent heat of vaporization that occurs when a liquid changes phase to vapor. In pool boiling, bubbles generated from liquid in contact with the heated surface are driven away by buoyancy opening up new nucleation sites. Pool boiling performance degrades significantly at the critical

heat flux (CHF) where nucleate boiling transitions to film boiling. Current pool boiling research focuses on raising the CHF through tuning surface wettability, introducing nanoparticles, and fabricating nanowire arrays [25-27]. Flow boiling, in microchannels, offers a practical phase-change option in compact packaging. Evaporation, commonly found in heat pipes, is another liquid-vapor phase change method to dissipate high heat fluxes. In a thin-film evaporation system, liquid evaporates through a thin film (~1 μm), which minimizes conduction resistance. Recently, thin-film evaporation has been demonstrated through micro-structured wicks [28] and nanoporous membranes etched in silicon [29].

There are numerous challenges with two-phase cooling solutions that must be overcome before their widespread implementation for electronics cooling. Challenges with flow boiling include several types of instabilities that can result in dry-out and significant oscillations in temperature. For example, the Ledinegg instability occurs when the slope of the demand pressure drop versus flow rate curve is negative and steeper than the supply loop pressure drop versus flow rate curve [30]. Additional instabilities include density-wave oscillations and pressure drop oscillations that can occur in flow boiling systems [31]. A significant challenge with thin-film evaporation is that because it operates with 100% vapor quality, it is susceptible to impurities and clogging [32]. A significant challenge with any two-phase cooling solution is maintaining system pressures and flow rates for both the liquid vapor and liquid phases. For these reasons, the focus of this work is on single phase cooling solutions.

1.2.2. State-of-the-Art: Embedded Single Phase Solutions

Within the past decade, DARPA has pursued several research programs to improve the thermal management of microelectronics through the creation of an Embedded Cooling portfolio. This portfolio consisted of the Near Junction Thermal Transport (NJTT) and Intrachip/Interchip Enhanced Cooling (ICECool) programs. This effort was focused on cooling GaN power amplifiers through "embedding" cooling directly into the chip or package, in close proximity to the heat generation site. The NJTT program focused on reducing the thermal resistance within the first 100 μm of the microelectronic device through transferring GaN epitaxial layers to diamond [33]. The ICECool Fundamentals program pursued the discovery and maturation of two-phase cooling technologies [34]. The ICECool Applications program pursued closer-term single phase cooling of RF devices through jet impingement and microchannels in high conductivity substrates. The following section summarizes some of the major works from the ICECool Applications program and reflects the state-of-the-art for single phase cooling solutions.

Gambin et al. (2016) led a Northrop Grumman and General Electric team in developing a cooling design for a GaN-on-SiC RF MMIC in a 20 GHz power amplifier. Their design etched microchannels into the SiC die and grew a diamond layer on the exposed surface with chemical vapor deposition (CVD). The

die was then bonded to a silicon manifold, which had been etched with 150 μm diameter jets. Their study included CFD modeling of thermal, fluid, and structural tools to predict component temperature, pressure drop requirements, and diamond stress concentrations. The authors provided experimental validation of performance using a closed flow loop with propylene-glycol coolant and thermal measurements with an IR camera (SC700, FLIR). Their microchannel-impingement system was used to cool a device with an average die level heat flux of 1.16 kW/cm^2 and a hot-spot heat flux of 52.5 kW/cm^2. This cooling enabled a 4x increase in MMIC output power [35].

Altman et al. (2015) led a Raytheon team in designing diamond microfluidic cooling of a GaN HEMT-based MMIC. Their study included modeling, simulation, and micro-fabrication. Their work increased the diamond substrate thickness from 100 μm to 300 μm without inducing additional stress or altering electrical characteristics. Their cooling design consisted of high aspect ratio microchannels etched in the diamond substrate. The microchannels employed high aspect ratios of 25 μm width and 191 μm depth. To supply fluid (ethylene glycol and water mixture), the authors fabricated and bonded a Si manifold wafer etched by deep reactive ion etching (DRIE) to the diamond substrate. Their analysis predicted a die level heat dissipation of 1.23 kW/cm^2 and hot spot cooling of 38 kW/cm^2 [36].

Ditri et al. (2016) led a Lockheed Martin team in designing, fabricating and testing a micro cooler attached to a GaN-on-SiC MMIC. Their design incorporated ninety circular 60 μm diameter jets with a 200 μm pitch and was fabricated from palladium using a custom additive manufacturing technique. The authors included 55 fluid return ports to prevent detrimental cross flow effects. The authors used ANSYS to create a CFD model to predict temperature and pressure drop requirements. Additionally, their analysis included analysis of the potential for erosion of the 4 μm gold layer acting as the ground reference plane for the RF circuit [37-38].

1.3. Embedded Microjet Impingement in Silicon

This thesis will be focused on better understanding the behavior and effectiveness of a microjet cooler embedded in silicon, which was developed at Lincoln Laboratory. This microjet cooler serves as a test device for probing the physics and behavior of microjet impingement cooling more generally. As observed in the preceding section, current single phase cooling approaches employ microchannels and jet impingement etched in high conductivity substrates such as diamond and palladium. These approaches achieve high performance, however, they employ expensive materials and advanced manufacturing techniques. In contrast, the microjet cooler in this thesis was fabricated in a relatively inexpensive silicon substrate using industry-standard processes. An illustration of the embedded microjet cooler structure is shown in Figure 1.2.

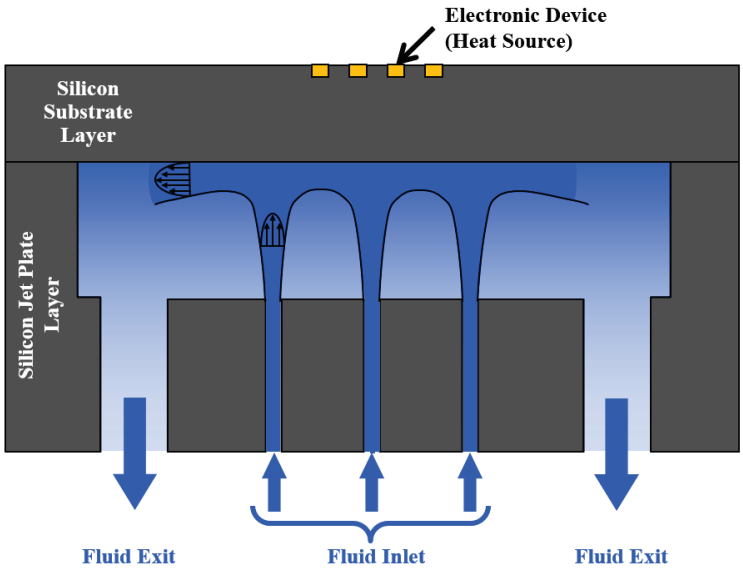

Figure 1.2: Illustration of embedded microjets fabricated in silicon.

In this arrangement, a microjet array is formed in a jet plate, which is then bonded directly to the substrate of the electronic device. A fluid reservoir is formed as flow enters through microjet orifices and exits through wider exhaust ports. The intended target for the microjet cooling is RF devices including HEMTs used in power amplifiers. The liquid (water) remains single phase, which eliminates the two-phase flow instabilities discussed in Section 1.2.1. This thesis will present additional design rationale, fabrication details, numerical modeling, and experimental characterization of the embedded microjets in silicon cooling system.

1.4. Experimental Temperature Measurement Techniques

As the size scale of electronic devices decreases, the need also arises for effective methods of experimentally determining the temperature of the device during operation. Accurate device temperature assessment is crucial for understanding the device performance, reliability, and effectiveness of thermal management techniques. Experimentally obtained temperature information can inform future designs and operating requirements. There are several well-established techniques for measuring the temperature in a semiconductor device under power, but most are not suited for measuring temperatures with high local temperature gradients, such as those found in multifingered HEMT devices. Discussed below are two broad categories of device thermal characterization: electrical methods and optical methods. Challenges in these techniques, both in practical application and theoretical spatial resolution limits, suggest that micro-Raman thermography presents the most promising solution for temperature measurements in semiconductor devices.

1.4.1. Electrical methods

Several electrical characterization based techniques exist to determine the channel temperature in electronic devices. These electrical techniques measure changes in temperature-dependent parameters such as the drain to source on-resistance or the saturated drain current [39]. These methods use a calibration step where the parameters are measured as the temperature is externally increased. Then, during operation, the temperature can be extracted based on the data from the calibration step. A disadvantage of this method is that several physical phenomena can affect the electrical parameters in addition to temperature. Another limitation with electrical methods is that they only measure the average temperature over the active region. This limitation prevents the electrical methods from providing information about true peak temperatures, temperature gradients, and distributions away from the active components. Higher spatial resolution and more versatile techniques can thus offer additional information about the heat dissipation profile occurring in the small feature size of the HEMT geometry [40].

1.4.2. Optical methods

Optical methods allow probing of the device temperature without physical contact. Perhaps the most common optical technique to assess the temperature in semiconductor devices is infrared (IR) thermography. In IR thermography, a detector measures the blackbody radiation emitted from the surface of an electronic device. The radiated light intensity scales with T^4, according to the Stephan-Boltzmann law, and thus the surface temperature can be determined by measuring the radiated energy after a calibration step. The calibration is performed at a fixed temperature and zero power on a pixel-by-pixel basis because the emissivity varies across the surface of the device. Sample movement during or after the calibration step can result miscalculated temperatures. An additional challenge in IR thermography is that metal surfaces, such as contact pads, have low emissivity. Low emissivity materials can be probed when painted with black "paint." However, a relatively thick layer of paint can impact the temperature measurement and be difficult to fully remove from the device following the IR testing. Perhaps the most significant challenge in IR thermography is the theoretical spatial resolution limit. The spatial resolution depends on the wavelength (λ) of emitted light and the numerical aperture (NA) of the microscope objective according to

$$r_{\text{lateral}} = \frac{\lambda}{2 \cdot \text{NA}} \tag{1}$$

where r_{lateral} is the lateral spot size. In the medium wavelength infrared (MWIR) range (λ=3-8 μm), the lateral spatial resolution is fundamentally limited to ~3-5 μm. An additional limitation in IR detectors is that they are susceptible to thermally-induced noise. This noise can be reduced by integrating the detector with a cryocooler, which lowers the sensor temperature to cryogenic temperatures. Even with a cooled IR detector, the most advanced IR detectors currently available are spatially limited to ~3 μm. From Equation

1, the lateral spatial resolution can be improved by increasing the NA of the objective or switching to the visible spectrum. The two primary optical methods that operate within the visible spectrum are thermoreflectance and micro-Raman thermography.

Thermoreflectance measures the temperature based on changes in the reflectivity of the sample's surface [41]. One of the major challenges in thermoreflectance is the difficulty in measuring the relatively small thermoreflectance coefficient [40]. Micro-Raman thermography, the main tool used in this thesis, will be discussed briefly here and in depth in Chapter 5. Micro-Raman thermography, which operates using visible light, is based on the principles of Raman spectroscopy. In the Raman scattering process, an incident photon is scattered to a new wavelength based on the emission (Stokes) or absorption (anti-Stokes) of a phonon. Raman is used in various disciplines including chemistry and materials science to identify and characterize molecular structure, bonding, quality, and other properties.

In micro-Raman thermography, a laser excitation source is focused to a ~1 μm spot size through a microscope and onto a material sample. The light interacts with the material and is either Rayleigh (elastic) or Raman (inelastic) scattered. The Rayleigh scattered light is filtered out through an edge filter and the Raman scattered light is analyzed by a spectrometer. The resulting spectrum for a given material shows a peak position corresponding to the phonon frequency and a linewidth corresponding to the phonon lifetime. The peak position and linewidth vary with temperature, and thus can be used as temperature probes during device operation. As will be discussed in this thesis, a major challenge in using micro-Raman thermography is understanding the contribution of stress that can bias temperature measurements. To this end, the Raman linewidth can be used to provide a stress free measurement of temperature, as it has been shown that the linewidth is stress insensitive to the first order [42].

1.5. Thesis Objectives and Outline

The increasing power density of GaN HEMTs has made thermal management a limitation in the effective operation of devices. Proper thermal management reduces operating temperatures, which improves performance, reliability, and lifetime of a device. The objective of this thesis is to characterize an embedded microjet impingement system, which is used to cool an integrated heater designed to match HEMT heat generation, both in geometry and in power density. A complement of numerical analysis and experimental techniques will be used to assess thermal and hydraulic performance of the cooling system.

In *Chapter 1*, the challenges of thermal management of advanced electronics used in communications and military hardware were discussed. Additionally, state-of-the-art cooling techniques and experimental temperature measurement techniques were presented.

In *Chapter 2*, the flow dynamics of an impinging jet are discussed. The microjet literature, focused on the confined, submerged array case, is reviewed. The design details of the microjet assembly used in this thesis, consisting of an integrated heater and microjet array formed in silicon, are explained.

In *Chapter 3*, the coupled heat transfer and computational fluid dynamics (CFD) numerical model that was built in COMSOL Multiphysics is described. The fluid and solid subdomains, and their governing equations, are discussed. The heat transfer coefficient was predicted for varying flow rates, as well as validation of Nusselt numbers with previous microjet studies.

In *Chapter 4*, the experimental setup used to evaluate the hydraulic performance is discussed. The experimental setup consisted of a closed flow loop that supplied fluid to the microjet assembly in a custom test fixture. Characterization of the pressure drop and flow rate was performed, as well as calculation of the discharge coefficient.

In *Chapter 5*, the theory of micro-Raman thermography for temperature measurements in semiconductors is discussed. The optical setup of the micro-Raman setup used in the experiments and the calibration of the silicon sample is shown.

In *Chapter 6*, the thermal and fluidic results of the microjet impingement system are presented. Additional practical concerns, such as microjet clogging and backside erosion, are addressed through an extended 1000-hour test.

In *Chapter 7*, the work is summarized and future directions for advancements in both high power-density cooling and thermal metrology using micro-Raman thermography are suggested.

2. Microjet Impingement: Design and Fabrication

Jet impingement has been the subject of research for several decades as a means of effectively transferring heat or mass between a solid surface and a fluid. Impinging jets have historically been used for cooling turbine blades [43], quenching metals [44], and drying textiles [45]. Jet impingement has recently been applied to cooling advanced electronic devices, which generate high heat fluxes [23]. Jet impingement cooling is well suited for this application due to its high heat transfer coefficients, low-pressure drops, and ability to achieve uniform surface temperatures when used in arrays [24]. Additionally, the architecture of an embedded jet impingement cooling solution removes several thermal interfaces, and their associated thermal resistances, between the heat-generating device and the coolant [46].

2.1. Jet Impingement Background

Jet impingement, by definition, consists of jet flow exiting from an orifice or nozzle that impinges on a targeted (heated) surface. This study was focused on the submerged and confined jet case in Figure 2.1, in which the jet issues into an enclosed cavity filled with the same fluid of which the jet is comprised (e.g., a water jet issues into a plenum of water).

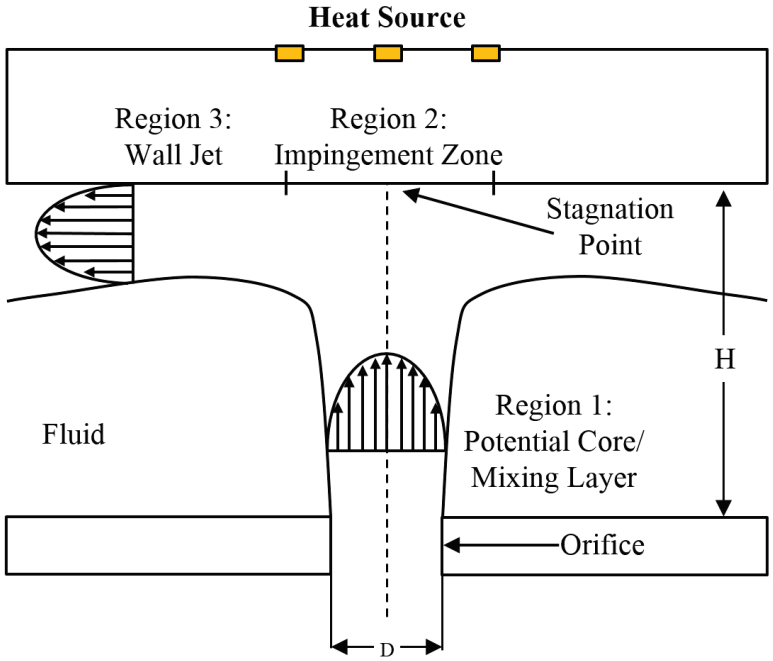

Figure 2.1: Schematic of submerged and confined jet impingement.

The characterization of flow behavior for a single jet impingement configuration is important for understanding the complex interactions that occur when jets are patterned in arrays of multiple jets. The key geometrical features identified in the illustration are the standoff, or jet-to-target, distance (H) and the

jet diameter (D). Smaller jet diameters are generally associated with higher heat transfer coefficients. The hydrodynamics of a single jet consist of several flow regions: the potential core/mixing layer region (Region 1), stagnation/impingement zone (Region 2), and the wall jet region (Region 3).

In the potential core and mixing layer (Region 1), the jet flow exits the orifice with a uniform velocity profile and enters the fluid cavity. This flow region is characterized by a velocity profile that develops, where the flow has a maximum velocity at the jet centerline and decreases at the edges. The maximum fluid velocity at the centerline is equal to the jet exit velocity, and is known as the potential core. In the lower-velocity mixing layer, the jet flow interacts with surrounding fluid of the cavity due to viscous effects. At the edges of this jet flow, recirculation zones form, entraining fluid in the jet. For jet-to-target (H/D) distances less than 6 to 8 diameters, the potential core reaches the target plate [47].

In the stagnation or impingement zone (Region 2), the jet flow strikes the impingement surface. The stagnation point is the intersection of the impingement surface and the jet centerline. The stagnation zone is a high-pressure region, where the flow slows to zero. The high pressure field suppresses the boundary layer to a very thin layer, and heat transfer is at a maximum in this zone. The stagnation zone extends vertically 1.2 jet diameters from the surface, and radially, spreads to 1.9 jet diameters [48].

In the wall jet region (Region 3), the flow is turned and directed parallel to the impingement surface due to the pressure gradient. In this region, the flow is parallel to the impingement surface, and a boundary layer develops due to viscous interactions between the wall and the fluid in the cavity. At approximately 2 jet diameters away from the stagnation point, the flow transitions to turbulence. This transition to turbulence is associated with a secondary peak in heat transfer coefficient [48].

Jets can be configured in arrays (Figure 2.2) to provide uniform heat dissipation and to increase heat transfer area. The geometry of the array, including the number of jets, jet spacing, and array type, influences its heat transfer performance. The number of jets, N_j, and total cross sectional area are important in calculating the area ratio, A_r, defined as the fraction of heater area covered by the total jet area. The center-to-center spacing, S, influences the location of secondary stagnation points identified in Figure 2.2. Secondary stagnation points are located between two primary stagnation points, and are regions where adjacent wall jets interact. Unlike primary stagnation points, secondary stagnations points exhibit decreased heat transfer performance. A study by Browne et al. showed that boiling typically began at the secondary stagnation zones [49]. They attributed the incipience of boiling at these locations to higher solid surface temperatures that occur due to lower fluid velocities, thicker thermal boundary layers, and lower heat transfer coefficients in these regions.

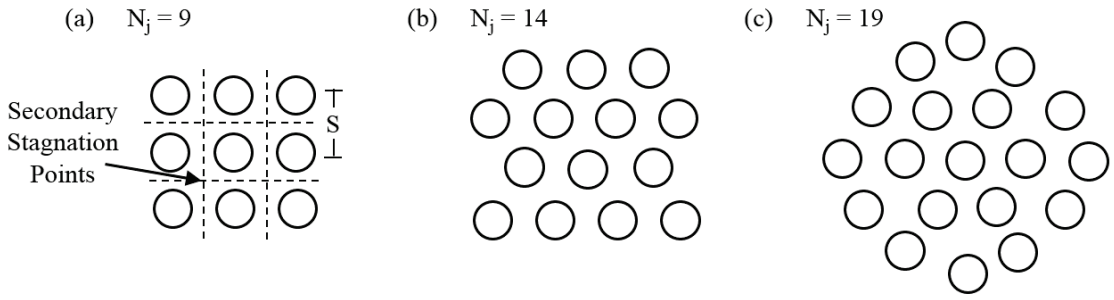

Figure 2.2: Example jet arrays (a) square array of 3 x 3 (b) staggered array of 14 jets (c) circular array of 19 jets.

One of the important considerations in implementing arrays of microjets, especially when scaling to larger areas, is proper management of the flow effluent. Crossflow is an effect where spent fluid interferes with the jet flow behavior in both the wall jet and stagnation regions and degrades heat transfer performance. Crossflow can be addressed by optimizing the array design by increasing either the jet spacing (S) or standoff (H). An alternative approach to address crossflow is to implement a manifold structure that extracts the spent fluid before it can degrade surrounding jet dynamics.

In addition to the effect of the geometrical parameters discussed above, heat transfer performance of a jet impingement system varies with fluid properties and flow velocity. The Nusselt number is often used to describe the heat transfer performance of the system. The Nusselt number is the dimensionless ratio of convective to conductive heat transfer at a boundary.

$$Nu = \frac{hD}{k} \tag{1}$$

where h is the convective heat transfer coefficient, D is the length scale of interest (jet diameter for these studies) and k is the thermal conductivity evaluated at the film temperature. Lindeman and Shedd [50] compiled numerous jet impingement heat transfer correlations, suggesting a final form of

$$\overline{Nu_D} = C\ Re_D^m Pr^n$$
$$C = f\left(A_r, \frac{H}{D}, \frac{S}{D}, \frac{L}{D}\right) \tag{2}$$
$$0.46 < m < 0.78 \text{ and } 0.26 < n < 0.48$$

where $\overline{Nu_D}$ is the area averaged Nusselt number based on the jet diameter, and a fitting coefficient (C) is a function of geometry including area ratio (A_r), jet-to-target distance (H), heater length (L), and jet-to-jet spacing (S). The fluid properties that affect the heat transfer performance are the Reynolds number (Re_d) and the Prandtl number (Pr).

$$Re_D = \frac{\rho V D}{\mu} \tag{3}$$

$$Pr = \frac{\mu\, c_p}{k} \tag{4}$$

The Reynolds number, described in Equation 3, is a dimensionless ratio of the inertial to viscous forces where ρ is the fluid density, V is the velocity at the jet, D is the jet diameter and μ is the dynamic viscosity. The Prandtl number is a dimensionless ratio of momentum diffusivity to thermal diffusivity calculated in Equation 4, where μ is the dynamic viscosity, c_p is the specific heat capacity and k is the fluid thermal conductivity. Equation 2 shows that the heat transfer performance of jet impingement has a strong dependence on Reynolds number through the relatively high exponent, m. Additionally, the fluid thermal and viscous properties have an effect on the heat transfer performance with the Nusselt number dependence on Prandtl number through the exponent, n.

The Nusselt number dependencies on the Reynolds and Prandtl numbers of the fluid highlight several design considerations when selecting a fluid and flow velocity. First, higher performance is achieved at higher jet velocities. The tradeoff with higher performance, however, is an increase in pressure drop and pumping power requirements. The fluid selection process involves weighing several thermal and viscous properties to determine their contributions to heat transfer performance. For example, having a higher viscosity fluid would increase the Prandtl number, but decrease the Reynolds number.

2.2. Jet Impingement Literature Review

Numerous researchers have conducted optimizations and experimental investigations of the heat transfer performance of jet impingement cooling systems. As discussed in Section 2.1, the three main geometrical parameters that influence heat transfer are jet diameter (D), jet-to-jet spacing (S), and jet-to-target height (H). In his 1977 seminal paper on the heat transfer of jet impingement, Martin concluded "scaling down all three lengths simultaneously results in monotonically increasing heat transfer coefficients," [51]. The following review will be focused on the specific subset of jet impingement literature of submerged, confined jets at the microscale (10^{-6} meters) consistent with the focus of this thesis. The review will explore both geometrical features and flow characteristics that influence single phase, microjet impingement heat transfer.

Womac et al. (1993) studied both submerged and free-surface jets using water and FC-77 (a dielectric, fluorinated liquid) as the working fluid at volumetric flow rates of 0.2 to 5.0 lpm. Jets with diameters of 0.513 mm and 1.02 mm were arranged in 2 x 2 and 3 x 3 square arrays at jet-to-jet spacing (S/D) ranging from 5 to 20 jet diameters. The experimental data was analyzed using an area weighted, two-region approach to account for heat transfer occurring in both the impingement and wall jet regions. In the impingement region, Nu varied with $Re^{0.5}$, while in the wall jet region, Nu varied with $Re^{0.8}$. For both the impingement and wall jet regions, Nu varied with $Pr^{0.4}$. The submerged jet arrays achieved higher heat

transfer performance than the free-surface jets. For a given volumetric flow rate, the heat transfer performance improved with decreased jet diameter and jet-to-jet spacing [52].

Fabbri and Dhir (2005) studied the heat transfer performance of 10 different microjet arrays using water and FC40 coolants. Fluorinert Electronic Liquid (FC40) is a high boiling point (165 °C) liquid used in single phase heat transfer applications. Jet diameters of 69 to 250 μm were laser drilled into a 0.5 mm thick stainless steel orifice plate in circular array patterns with a radial and circumferential pitch of 1 mm, 2 mm and 3 mm. The number of jets ranged from 61 on the 1 mm pitch to 397 on the 3 mm pitch. The maximum surface heat flux of 310 W/cm^2 was achieved with water jets at 12.5 m/s using a 173.7 μm diameter and 3 mm jet-to-target spacing. From a fit of the experimental data, Nu varied with $Re^{0.78}$ and $Pr^{0.48}$. Additional hydrodynamic analysis included calculation of the friction factor and required pumping power. The paper suggests that the optimal configuration consists of a large number of small diameter (D= 100 μm) jets [53].

Brunschwiler et al. (2006) presented results using a hierarchical branching architecture with 50,000 jets designed to minimize crossflow of the spent fluid. Deep reactive ion etching (DRIE) was used to create jets with diameters of 31 to 126 μm and cell pitches of 100 to 500 μm. The jet-to-target distances ranged from 3 to 300 μm. The maximum heat transfer coefficient was 87,000 W/m^{2}K and the maximum heat flux removed was 420 W/cm^2 at 2.5 lpm. A pressure drop analysis included contributions from both frictional and dynamic losses. A data fit of the results showed that Nu varied with $Re^{0.73}$. The authors designate an optimal jet to nozzle distance of $H/D \geq 1.2$ [54].

Robinson and Schnitzler (2007) performed a study of both submerged and free jet arrays using water as the working fluid. Jet geometries were created in a 3.0 mm thick 3-D printed plastic plate. Jet diameters were 1.0 mm, jet spacing (S/D) consisted of 3, 5, and 7 jet diameters and jet-to-target (H/D) distances ranged from 2 to 30 jet diameters. Flow rates were varied from 2 to 9 lpm. An experimental fit of the data showed that Nu varied with $Re^{0.46}$ and $Pr^{0.4}$. The study suggested that the heat transfer performance was insensitive to changes in the jet-to-target when the nozzle was close in proximity to the heat source ($2 \leq H/D \leq 3$). A pumping power analysis showed that the closely spaced submerged jet array ($S/D = 3$) achieved the highest heat transfer performance at a given pumping power [55].

Browne et al. (2010) investigated two microjet arrays using deionized water and air as the working fluids. The high area ratio jet geometry was fabricated in silicon using DRIE. The jet arrays used diameters of 54 and 112 μm, jet-to-jet spacing (S/D) of 2.2 and 4.6 jet diameters, and jet-to-target (H/D) distances of 1.8 and 3.7 jet diameters. The maximum heat flux was 1110 W/cm^2 with a heat transfer coefficient of

414,000 W/m^{2}K. For the larger diameter array, Nu varied with $Re^{0.55}$ and $Pr^{0.29}$ and for the smaller diameter array, Nu varied with $Re^{0.67}$ and $Pr^{0.51}$ [56].

Michna et al. (2011) studied inline and staggered arrays using both air and deionized water as the working fluid. The authors explored the Nusselt number dependence on the area ratio in addition to the Reynolds and Prandtl numbers. The area ratio was varied from 0.036 to 0.354 and Re varied from 180 to 5100. The Michna et al. correlation suggests that an optimal area ratio exists at approximately 0.232, but that performance is relatively high with area ratios from 0.10 to 0.30 [57].

Table 2.1: Summary of microjet studies and correlations, modified from [50].

Researcher	D (μm)	S/D	H/D	Re	Fluid	Correlation
Womac (1993) [52]	513-1020	4.95-19	1-10	500-20,000	Water, FC77	$\overline{Nu_D} = [0.5Re_D^{0.5}A_{rW} + 0.3\left(\frac{D}{L}\right)^{0.4}(1 - A_{rW})]\,Pr^{0.4}$
Fabbri (2005) [53]	69-250	4-26.2	-	43-3813	Water, FC40	$\overline{Nu_D} = 0.043\,Re_D^{0.78}Pr^{0.48}e^{-0.069\left(\frac{S}{D}\right)}$
Brunschwiler (2006) [54]	31-126	3.2-9.9	0.1-9.7	5-900	Water	$\overline{Nu_D} = 0.78\,Re_D^{0.73}$
Robinson (2007) [55]	1000	3-7	2-30	650-6500	Water	$\overline{Nu_D} = 23.4Re_D^{0.46}Pr^{0.4}\left(\frac{S}{D}\right)^{-0.4}\left(\frac{H}{D}\right)^{-0.007}\left(\frac{D}{L_h}\right)$
Browne (2010) [56]	54, 112	2.2, 4.6	1.8, 3.7	150-4900	Water, Air	$\overline{Nu_D} = 0.20\,Re_D^{0.637}Pr^{0.4}$
Michna (2011) [57]	54-112	1.8-5	2-4	50-5100	Water, Air	$\overline{Nu_D} = 0.675Re_D^{0.55}Pr^{0.243}\,cos(5.42A_r - 1.26)$

The submerged, confined microjet array literature review highlighted several design insights. Several different parameters govern the performance of the jet impingement cooling system including the jet diameter, jet-to-jet spacing, area ratio, and jet-to-target distance. These parameters and the resulting Nusselt correlations are shown in Table 2.1. Womac et al. showed that the heat transfer coefficient increased with smaller diameter jets [52] and Fabbri and Dhir suggested that the optimal jet diameter was D=100 μm [53]. Robinson and Schnitzler highlighted that the highest heat transfer coefficient was achieved with the smallest jet-to-jet pitch of S/D of 3 jet diameters [55]. Additionally, the authors showed that heat transfer performance was relatively insensitive to jet-to-target (H/D) distance when the jet-to-target distance was less than 3 jet diameters. Lastly, Michna et al. used the area ratio approach to suggest that the optimal jetted area to heated area ratio should be approximately in the range of 10-30 percent [57]. In summary, this literature review provides general principles for optimal jet diameter, jet-to-jet spacing, and jet-to-target distance when designing a submerged microjet array, which were then considered in the design of the array in this thesis in Section 2.4.2.

2.3. GaN HEMT Heat Generation

As discussed in Section 1.1, increasing power levels in high electron mobility transistors (HEMTs) with wide bandgap semiconductors such as GaN represent a pressing challenge in thermal management due to their high linear power densities. The HEMT structure consists of a horizontal electrically conducting channel with metallized source, gate, and drain. In RF applications, HEMTs are used in power amplifiers as the gain element to amplify signals, often in the frequency range of 1 GHz to 50 GHz. The RF power amplifier operates by consuming DC power and converting a portion of it to RF power and dissipating the remaining DC power as heat [58]. Self heating in GaN HEMTs is a result of Joule heating, which is calculated according to

$$H = \vec{J} \cdot \vec{E} \tag{5}$$

where H is the heat generation rate in W/cm^3, $\vec{J}$ represents the current density (A/ cm^2) and $\vec{E}$ is the applied electric field (V/cm). The physical mechanism for self heating is the gain in energy in electrons as electric field is applied and the subsequent loss of energy during collisions with the semiconductor lattice structure in drift and diffusion [59]. As discussed in Section 1.1, multifingered GaN HEMTS are used to generate larger power. The multifinger design is intended to avoid transmission losses, gate resistances, and phasing problems that would occur in an extremely wide gate. As a result of the multifingered design, there are thermal interactions between individual gate fingers known as thermal crosstalk. The effect of thermal crosstalk is higher temperature rises than in single isolated fingers and maximum gate finger temperatures occurring at the center of the device [60]. Multifingered GaN HEMTS vary in number of fingers, gate width (w), gate length (L_G), and gate-to-gate pitch (L_P). Within the HEMT, the majority of heat is generated in the highly localized regions beneath the gate fingers and these heat fluxes can be modeled as surface heat fluxes corresponding to the size (w x L_G) and position of each gate finger [9].

2.4. Microjet Assembly

In this experimental study, a microjet array was designed, fabricated, and integrated into a compact assembly. The microjet assembly consisted of two main components bonded together: the integrated heater and the microjet array. The integrated heater was a resistive heater designed to match the geometry and power dissipation profiles of advanced electronic devices, while allowing for a more instrumented experimental evaluation. Two different microjet array designs were created and are shown in their respective stack-up assemblies in Figure 2.3.

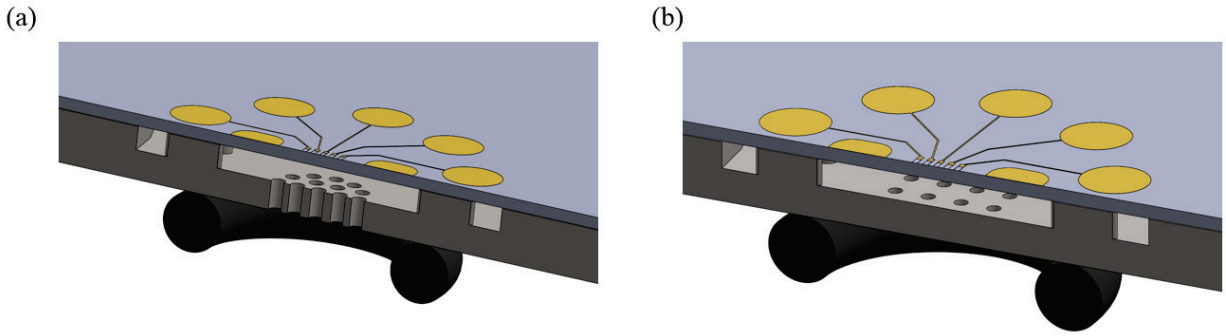

Figure 2.3: Microjet assembly with the integrated heater (top layer), microjet array (bottom layer), and inner O-ring used for fluidic sealing with two different microjet array types: (a) circular array of 19 microjets with diameter of 116 µm (b) square array of 16 microjets with diameter of 100 µm.

2.4.1. Integrated Heater Wafers

The high power-density heater was created with a titanium nitride (TiN) ceramic heater deposited on the top surface of a silicon substrate. This resistive heater formed a circuit comprised of ten finger-like segments of high resistance, connected in series by lower resistance pads designed to mimic the heat dissipation profile of a multifingered GaN HEMT discussed in Section 2.3. The heater geometry, indicating where the 150 nm thick TiN was deposited, is shown in Figure 2.4. The high resistance segments were designed to match 10 x 100 µm gate fingers with length L_G = 1 µm and width L_W = 100 µm. The pitch (L_P) between each of the segments was 40 µm, with the exception of 35 µm between the two center-most legs.

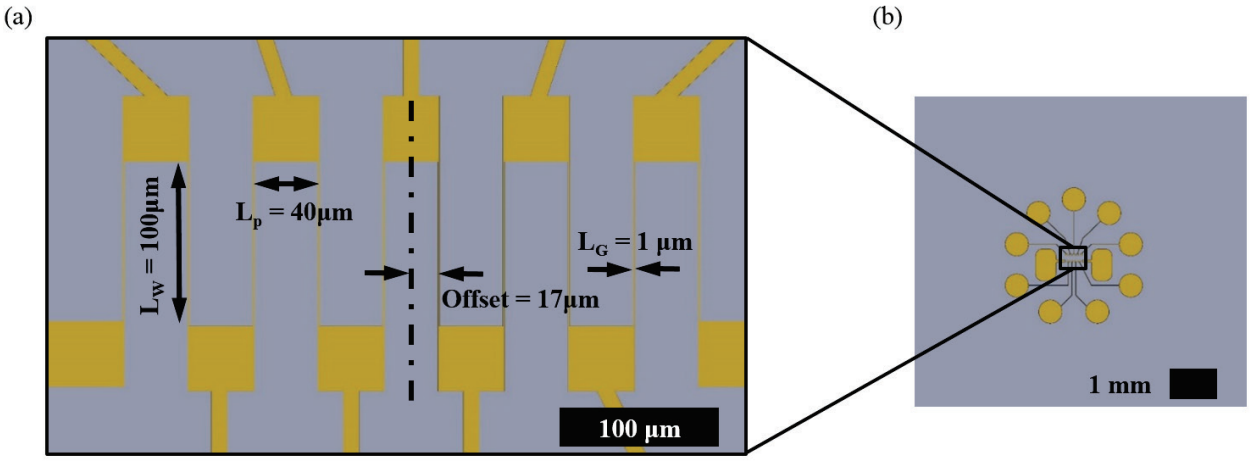

Figure 2.4: (a) Geometry of 10 heat generating "fingers," each with a gate length of 1 µm and gate width of 100 µm. (b) Low magnification view of the integrated heater and 11 surrounding contact pads on the die.

The high resistance segments were connected by lower resistance pads, each with less than 1% of the resistance of the finger-like segments, concentrating the Joule heating to the very narrow finger-like sections. This concentration created a row of ten high power-density linear segments. The power density,

or heat flux (q"), is a term used to express the power dissipation (q) through an area ($A_{fingers}$). The heat flux was calculated according to

$$q" = \frac{q}{A_{fingers}} = \frac{q}{10\ L_W\ L_G} \tag{6}$$

where the power dissipation was divided by the total cross sectional area of the 10 fingers. This concentration of heat generation resulted in very high power densities (20 kW/cm^2) at modest overall power dissipation (2W).

The high power-density heater was fabricated on a silicon substrate. The silicon wafer was thinned to a total thickness of 200 μm and encapsulated with a plasma-enhanced chemical vapor deposition (PECVD) SiO_2 protective oxide, which covered the top of the heater traces for protection. Ohmic contact pads, opened through the oxide, were located around the heater circuit, plated with 500 nm of gold, and were used to deliver a driving potential to the heater by way of DC probe tips on micro-manipulators. The high power-density heaters were diced into 20 mm × 20 mm dies.

2.4.2. Microjet Array Wafers

As discussed in Section I, the geometry of arrays of microjets has been the subject of extensive optimizations and experimental investigations. For submerged and confined microjets, optimal performance is achieved with closely spaced microjets (within 1.5-3 jet diameters), at a close standoff distance (1.5-3 jet diameters) [55]. Building off the conclusions of these optimizations, two initial geometries were chosen: one with a circular patterned microjet array and one with a square patterned array. The intent of the circular array was to facilitate using circular O-rings for fluidic sealing. The circular array, shown in Figure 2.5a, used 19 microjets, each with a diameter of 116 μm. The array was constructed with 12 microjets on an outer ring with a diameter of 720 μm, 6 microjets on an inner ring with a diameter of 380 μm and 1 microjet at the center. This resulted in an average jet-to-jet pitch, S, of 193 μm, or approximately 1.67 jet diameters. The standoff distance, H, was 200 μm, or 1.72 jet diameters. The standoff distance was achieved by centering the microjet array in a cloverleaf shaped well, shown in Figure 2.5b. The cloverleaf shaped well formed the fluid plenum between the microjet array and the high power-density integrated heater.

The cloverleaf well geometry was qualitatively designed to passively guide the fluid streamlines from the microjet array to the large exhaust ports (1 mm diameter) located in each of the four corners. The exhaust ports were sized such that the cumulative cross sectional area of the exhaust ports was an order of magnitude larger than the cumulative microjet cross sectional area. This design minimizes the required driving pressure, and localized the pressure losses within the device to the microjets. Surrounding the array of circular microjets (but inside the exhaust port pattern) exists an array of pillars. These pillars serve two

primary functions: they provide structural support within the well, and they nominally increase surface area while guiding the flow to the exhaust ports. The structural support function becomes more important for the completed assembly, where devices were installed into a test apparatus with micro O-rings. The microjet array wafers were diced into 20 mm × 20 mm dies.

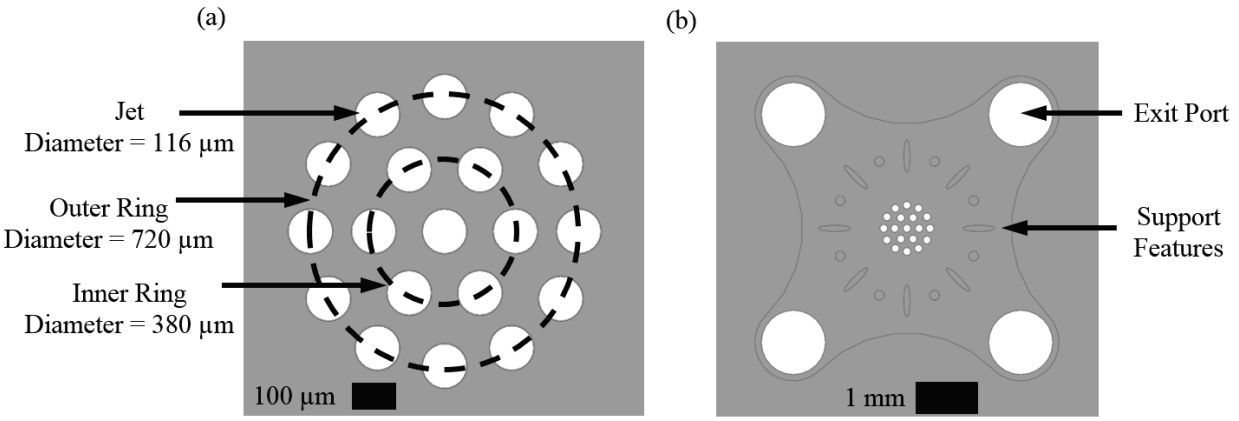

Figure 2.5: (a) Geometry of the circular array showing the two concentric rings on which the microjets are arranged. (b) View of the clover-shaped well that contains the circular microjet array, support features, and exit ports.

Another parameter that has been shown to influence heat transfer performance is the area ratio, which is the ratio of jet orifice area to the heater surface area. The area ratio was calculated for this array by dividing the total cross sectional area of the 19 microjets by the 1 mm x 1 mm heated area. The area ratio for the circular array was 0.201, which fits within the range of area ratios studied by Michna et al. [57].

A second array of 16 microjets was designed in a square array with 4 columns and 4 rows, shown in Figure 2.6a. The jet diameters were 100 μm and the pitch between each jet was 250 μm. Similar to the design of the circular array, the standoff distance was 200 μm. The design used spacing of 2.5 jet diameters and standoff distance of 2 jet diameters, which were both relatively larger than the circular array due to the smaller jet diameter. The jet array was contained in a similar cloverleaf shaped well with four exit ports at the corners and a ring of support features to enhance heat transfer. The area ratio of 0.126 for the square array was also lower than the circular array because the square array had fewer jets and the jets had smaller diameters, resulting in a lower total orifice cross sectional area for the same size heated area.

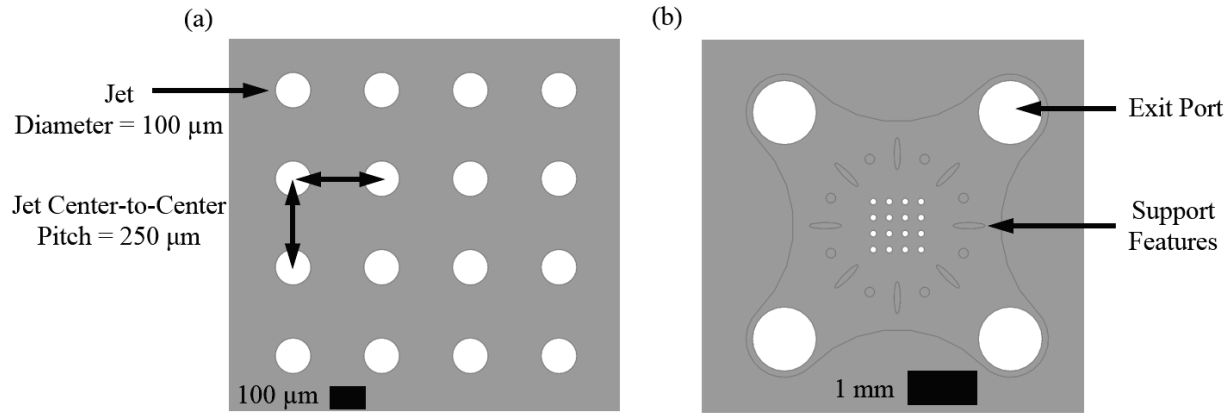

Figure 2.6: (a) Geometry of the 4 x 4 square array of microjets. (b) View of the clover-shaped well that contains the square microjet array, support features, and exit ports.

The geometry details of the two arrays are summarized below in Table 2.2. The two arrays are expected to demonstrate different heat transfer performance due to the slightly different jet diameters, jet-to-jet spacing, jet-to-target distance, and area ratios. While the chosen microjet arrays could be further improved with parametric optimization, the microjet arrays were chosen to prove the concept of fabricating in silicon substrates and bonding in a compact package.

Table 2.2: Summary of microjet geometry for circular and square arrays.

Parameter	Symbol (units)	**Circular Array**	**Square Array**
Jet diameter	D (µm)	116	100
Number of jets	N_j	19	16
Jet-to-jet spacing (average)	S (µm)	193.42 (1.67 D)	250 (2.5 D)
Jet-to-target spacing	H (µm)	200 (1.72 D)	200 (2 D)
Area ratio	A_r	0.201	0.126

Both of the microjet arrays were fabricated in a 450 µm thick silicon substrate. Deep reactive ion etching (DRIE) is a standard dry etch process used to create two-dimensional prismatic shapes with high aspect ratios in silicon. To fabricate the microjet array plate, the 200 µm deep cloverleaf shaped well was first etched into one side from the hard mask. At the center of this well, the array of microjet orifices was etched through the remaining 250 µm of silicon.

To assemble the microjet-cooled test device, the integrated heater dies and the microjet dies were aligned and bonded together. Alignment between the two dies can be accomplished with metallic fiducials, proper fixturing, or by visual alignment. By design, the alignment of the microjet array to the device does not require precise alignment, as the circular array produces an impingement zone of almost 1 mm × 1 mm on

the back side of the device (i.e., much larger than the heated zone). In these experiments, devices were aligned to within 100 μm by use of custom fixturing.

Given the smooth surfaces of each die, several strategies are available to bond the dies. Direct fusion bonding, eutectic gold bonds, indium solders, or industrial adhesives may be used. As the bond line does not participate in the thermal path (i.e., microjets impinge directly on the backside of the heaters, not through the bond), the bond material is not important for thermal performance. This key attribute allows device designers and process engineers to use bonding technologies that are driven by the device process flow, and not by thermal requirements. Here, the two dies were bonded with industrial adhesive (406 Cyanoacrylate, Loctite).

2.5. Chapter Summary

In Chapter 2, jet impingement flow dynamics and relevant microjet array literature were explored in order to guide the design of two microjet arrays. The flow physics were discussed including the three primary flow regions: the potential core/mixing layer, the impingement/stagnation zone, and the wall jet region. The effects of patterning microjets in arrays were also discussed including secondary stagnation points and crossflow. Recent microjet array investigations, and their Nusselt number correlations, for various jet diameter, jet-to-jet spacing, and jet-to-target distances were discussed as well as their recommendations for optimal microjet array design. These insights from the literature were used to guide the design of a square and circular array, which were then fabricated in silicon with DRIE. An integrated heater of TiN was designed to match HEMT heat generation in both geometry and power levels. Lastly, the microjet array and integrated heater were bonded together to form a compact assembly.

3. Numerical Analysis

A fully conjugate computational fluid dynamics (CFD) and heat transfer model of the embedded microjet impingement assembly was developed in COMSOL Multiphysics 5.2a. The numerical model was used to predict thermal performance by calculating the heat transfer coefficient. Additionally, the model was used to generate a surface temperature profile of the heater device at specific fluid inlet and power density levels for comparison with experimental measurements.

3.1. Modeling Overview

Numerical simulation of jet impingement heat transfer has been the subject of several studies [61-62]. Numerical simulations can be used to predict the heat transfer coefficient, and resulting Nusselt number, as well as pressure drop characteristics. This information provides designers important information before fabricating jet impingement hardware, as well as the critical insight to optimize jet geometry and configurations. Although jet impingement geometry is relatively simple, the underlying fluid dynamics and heat transfer processes are complex. Two major challenges in modeling jet impingement behavior are that the flow is generally turbulent and that it features steep velocity gradients.

In this study, COMSOL Multiphysics 5.2a was used to solve a fully conjugate conduction heat transfer, computational fluid dynamics (CFD), and convection heat transfer simulation for steady-state non-isothermal flow. The numerical model imported both heater device and microjet array geometry from Solidworks using the CAD Import feature. The model solves the well-established conservation of momentum, mass, and energy equations as will be discussed in this chapter. The simulation domain was divided into a fluid subdomain and a solid subdomain, the latter representing the heater. Figure 3.1 shows both a top and bottom view of the solid and fluid subdomains used in the simulations.

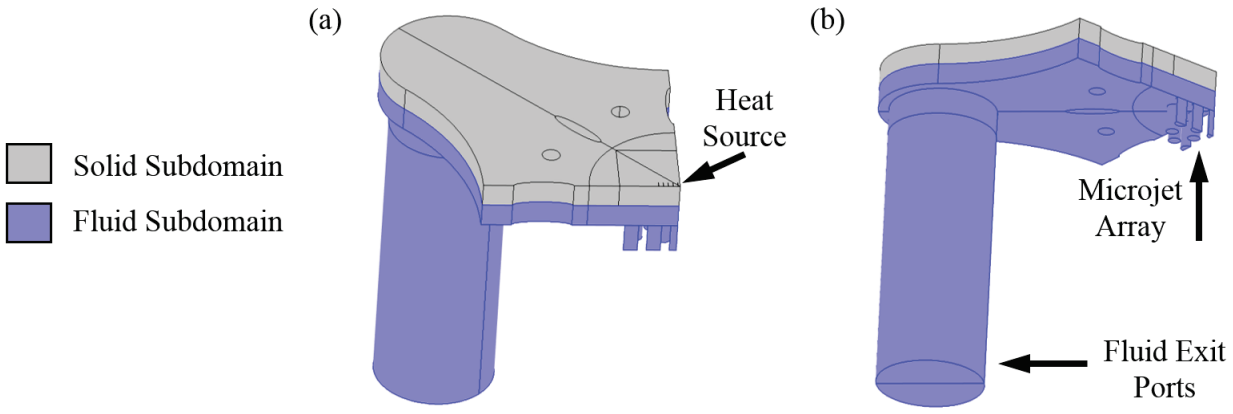

Figure 3.1: (a) Top perspective image shows the integrated heater with thin, high resistance "fingers" as the heat source. (b) Bottom perspective image shows a view of the microjet array inlet and the four fluid exit ports.

The solid subdomain is represented by the top layer of the cloverleaf shaped model in Figure 3.1a. The heater die extended 200 μm vertically, the thickness of the silicon substrate. The ring of support features discussed in Section 2.4.2 was not included in the solid subdomain. The geometry of the integrated heater is shown at the center of the cloverleaf shaped heater with ten fingers that are each 100 μm long and 1 μm wide with a 40 μm pitch. The properties of the solid subdomain are shown below in Table 3.1, for a silicon material.

Table 3.1: Silicon properties used in modeling.

Property	Symbol (units)	Value
Thermal Conductivity	k (W/m-K)	150
Specific Heat	c_p (J/kg-K)	700
Density	ρ (kg/m^3)	2329

The fluid subdomain was defined by the 200 μm deep well directly beneath the heater substrate. The microjets in this work operated in the submerged, confined condition, so this well was filled with liquid. At the center of the well, an array of cylinders protruding from the microjet array orifices represent the incoming fluid contained within the 250 μm thickness of the jet orifice plate. At the four corners of the cloverleaf shaped well are the 1 mm diameter cylinders that extend 3 mm above the fluid well. The height of the cylinder was chosen from a modeling study to ensure that flow at the outlet was normal to the boundary and unidirectional. The temperature dependent properties of thermal conductivity (k), specific heat (c_p), and density (ρ), and dynamic viscosity (μ) of the liquid (water) were taken from the COMSOL library of material properties and are shown in Table 3.2 along with the properties at room temperature.

Table 3.2: Fluid (water) properties used in modeling.

Property	Symbol (units)	Temperature Dependent Value for T (K)	Value at Room Temperature (20 °C)
Thermal Conductivity	k (W/m-K)	-0.87 + 8.95E-3T - 1.58E-5T^2 + 7.98E-9T^3	0.594
Specific Heat	c_p (J/kg-K)	1.20E4 - 80.4T + 0.31T^2 - 5.38E-4T^3 + 3.63E-7T^4	-1.98E4
Density	ρ (kg/m^3)	839 + 1.40T - 3.01E-3T^2 + 3.72E-7T^3	1000
Dynamic Viscosity	μ (Pa-s)	1.38 - 0.02T + 1.360E-4T^2 - 4.65E-7T^3 + 8.90E-10T^4 - 9.08E-13T^5 + 3.85E-16T^6	1.01E-3

3.1.1. Turbulent Flow

As previously mentioned, a major challenge in modeling jet impingement is the complexity in the flow dynamics due to the turbulence. Turbulent flow is affected by the motion of small eddies, which are difficult to model. Whether flow is laminar or turbulent is generally a function of the Reynolds number. McNaughton and Sinclair classified jets based on their Reynolds number as dissipated laminar (Re<300), fully laminar (300 < Re < 1000), semi-turbulent (1000 < Re < 3000), and fully turbulent (Re > 3000) [63].

The Reynolds number (Re) can be calculated given the fluid density (ρ), jet velocity (V), jet diameter (D), and dynamic viscosity (μ) according to

$$Re = \frac{\rho V D}{\mu} \tag{7}$$

The Reynolds number is plotted against the jet velocity from 0 to 40 m/s for the two arrays used in this thesis in Figure 3.2. As seen in the plot, the circular array has a slightly higher Reynolds number than the square array at a given jet velocity. This higher value is due to the circular array jet diameter (116 μm) being slightly larger than the square array jet diameter (100 μm). The physical intuition behind the Reynolds number dependence on jet diameter is that in smaller diameter orifices, the viscous forces dampen inertial forces. In larger diameter orifices, the inertial forces are able to overcome viscous forces, resulting in turbulent flow behavior.

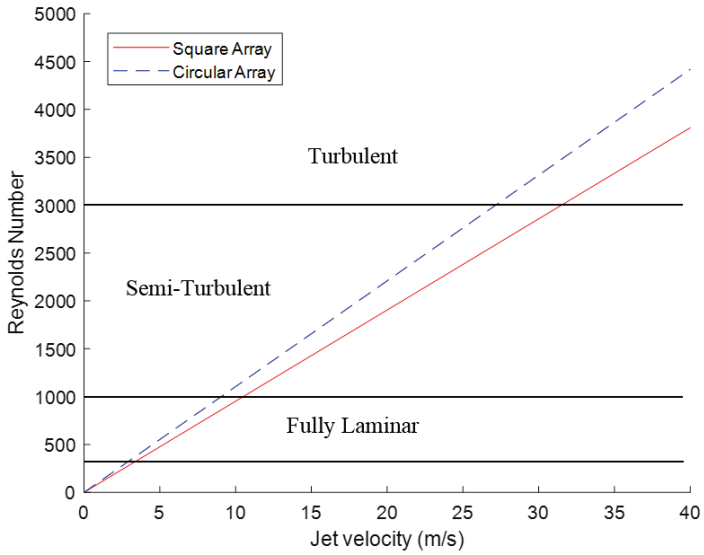

Figure 3.2: Reynolds number versus the jet velocity for the square and circular arrays. Also shown are the approximate thresholds for the fully laminar, semi-turbulent, and turbulent flow regimes.

The Reynolds number indicated that the flow was in the transition phase from laminar to turbulent. Additionally, the sharp edged orifice and small jet-to-target spacing can induce turbulence. Various methods exist for modeling turbulent flow such as the k-ω, k-ε, DNS/LES, and v^2f models. Zuckerman and Lior reviewed these models considering computational cost, accuracy of heat transfer coefficient prediction, and ability to detect secondary peaks [43]. The k-ω was highlighted for low computational time and moderate ability to predict heat transfer and secondary peaks. Additionally, the k- ω was selected as the appropriate model for flows with strong curvature, such as jets [64].

Turbulent CFD models are used to solve the Reynolds-Averaged Navier Stokes (RANS) equations for fluid flow transport. These equations, shown below, represent the conservation of mass, momentum, and energy (respectively) for steady state.

$$\frac{\partial}{\partial x_i}(\rho u_i) = 0 \tag{8}$$

$$\frac{\partial}{\partial x_j}(\rho u_j u_i) = -\frac{\partial p}{\partial x_i} + \frac{\partial}{\partial x_j}(t_{ji} + \rho\tau_{ji}) \tag{9}$$

$$\frac{\partial}{\partial x_j}\left[\rho u_j\left(h + \frac{1}{2}u_i u_j + k\right)\right] = \frac{\partial}{\partial x_j}\left[u_i(t_{ij} + \rho\tau_{ij}) + \left(\frac{\mu}{Pr_L} + \frac{\mu_T}{Pr_T}\right)\frac{\partial h}{\partial x_j} + (\mu + \sigma^*\frac{pk}{\omega})\frac{\partial k}{\partial x_j}\right] \tag{10}$$

The Boussinesq approximation was used to relate the turbulent stresses and mean strain rate. In order to complete the turbulence model, the k-ω method was chosen for the previously discussed reasons. The approach of this model is to solve for the turbulent kinetic energy (k) and the specific energy dissipation rate (ω) [43]. The equations used in the model to solve for these quantities are shown below

$$\frac{\partial}{\partial x_j}(\rho u_j k) = \rho\tau_{ij}\frac{\partial u_i}{\partial x_j} - \beta^* pk\omega + \frac{\partial}{\partial x_j}\left[(\mu + \sigma^*\frac{pk}{\omega})\frac{\partial k}{\partial x_j}\right] \tag{11}$$

$$\frac{\partial}{\partial x_j}(\rho u_j \omega) = \alpha\frac{\omega}{k}\rho\tau_{ij}\frac{\partial u_i}{\partial x_j} - \beta\rho\omega^2 + \sigma_d\frac{\rho}{\omega}\frac{\partial k}{\partial x_j}\frac{\partial \omega}{\partial x_j} + \frac{\partial}{\partial x_j}\left[(\mu + \sigma\frac{pk}{\omega})\frac{\partial \omega}{\partial x_j}\right] \tag{12}$$

To solve these equations, the default COMSOL closure coefficients were applied. The fluid boundary conditions were established at the inlet and outlet identified in Figure 3.3. The jet velocity was defined at the jet orifice face in meters per second. The fluid inlet temperature was set to 20 °C. A zero-pressure boundary was enforced on the outlet face of the fluid exit port. No-penetration and no-slip boundaries were defined on all other solid faces.

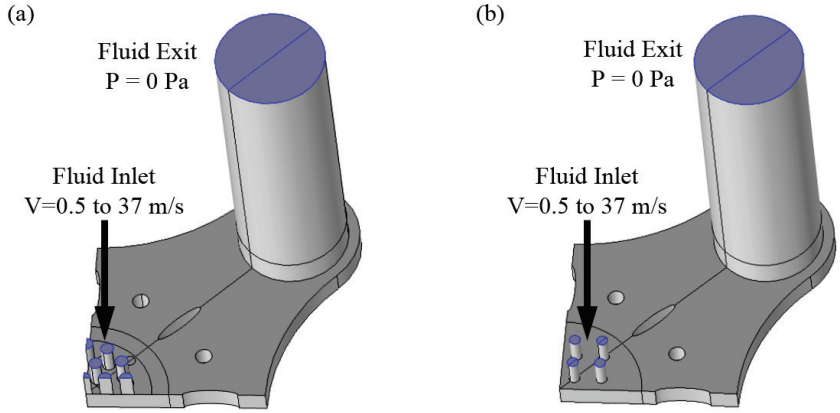

Figure 3.3: Fluid inlet and outlet boundary conditions for the (a) circular array (b) square array.

3.1.2. Heat Transfer

In the simulation, a heat generation term was applied as a uniform heat flux to the high resistance segments located at the top of the integrated heater. Chapter 2 discussed the specific geometry of the resistive heater, which was designed to match the geometry of a 10 x 100 µm HEMT, with a gate length (L_G) of 1 µm, gate width (L_W) of 100 µm, and pitch (L_P) of 40 µm.

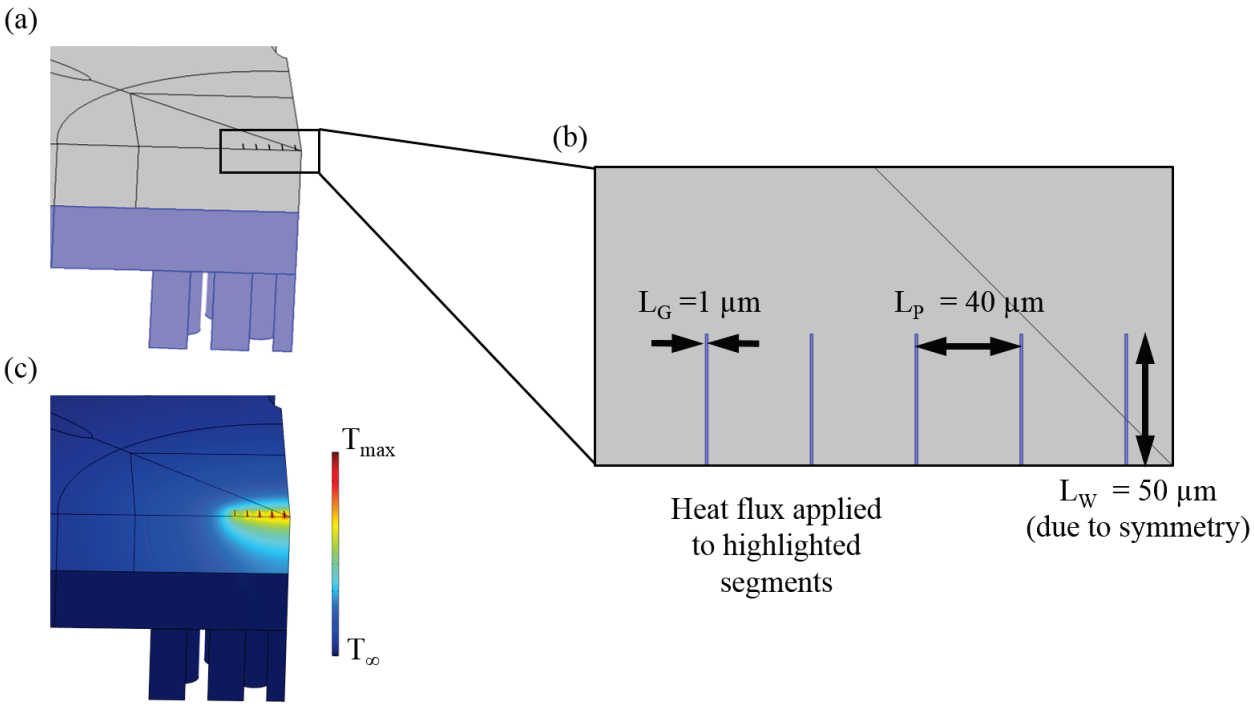

Figure 3.4: (a) Full model of solid and fluid subdomains. (b) Heat flux segments designed to match experimental heat flux in the ten 1 µm x 100 µm fingers. (c) Simulated temperature profile of the device under power.

The thermal transport, and resulting temperature distribution, occurring within the device and bulk fluid is governed by the steady state heat conduction equation shown below

$$\rho c_p \frac{\partial T}{\partial t} + \rho c_p \nabla T + \nabla q = Q \tag{13}$$

where the time dependent term, shown first, is not considered. Additionally, Fourier's law of heat conduction was used to relate the heat flux to the temperature gradient.

$$q = -k\nabla T \tag{14}$$

In this relationship, k represents the thermal conductivity of the material and T is the temperature. In the numerical model, the Joule heat generation of the HEMT geometry was included as a surface heat flux applied at the top of the device as seen in Figure 3.4a.

$$q = \frac{P_o}{A_{heater}} \tag{15}$$

In this equation, the heat flux boundary condition was a heat rate across the HEMT fingers. It was calculated by dividing the heat rate (P_o) by the area of the heater segments (A_{heater}). This structure allowed various heat fluxes to be simulated, by changing the heat rate. This also enabled straightforward comparison with experimental measurements in which a constant DC power, and resulting joule heat generation, created a constant heat flux boundary condition.

An adiabatic insulation boundary condition (i.e., $q_o = 0$ W) was enforced on external surfaces.

3.1.3 Thermal Transport at the Wall

Two-way multiphysics coupling was defined between the fluid dynamics and heat transfer models with COMSOL's non-isothermal flow feature and the Kays-Crawford heat transport turbulence model. Automatic wall treatment was used to solve for both the fluid and wall temperature according to

$$-n \cdot q = \rho c_p \beta_o^{*1/4} k^{1/2} \frac{T_w - T}{T^+} \tag{16}$$

After the solution was complete, the results were post-processed to calculate the local convective heat transfer coefficients on the 1 mm × 1 mm impingement zone above the microjet orifices.

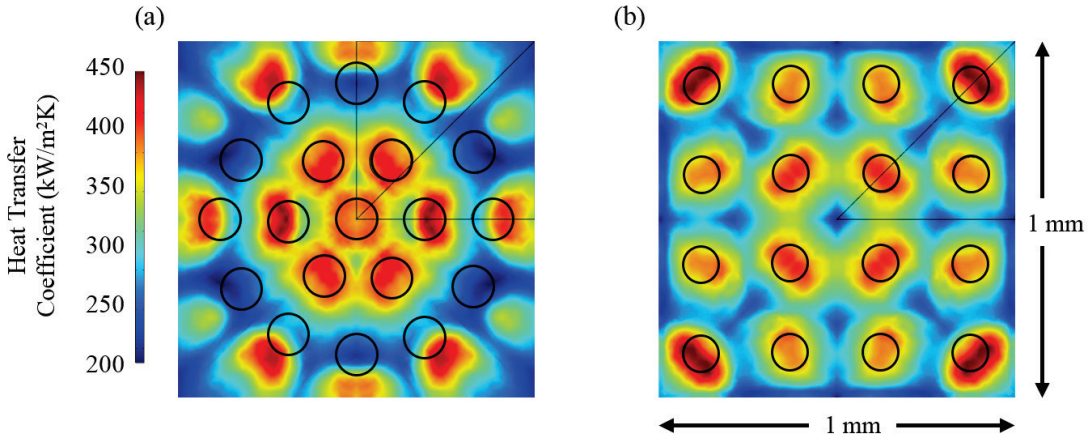

Figure 3.5: Heat transfer coefficient plots at jet velocity of 20 m/s for the (a) circular array (b) square array. Jet fluid is water. Projections of the jet locations are overlaid for visualization.

The heat transfer coefficient was calculated according to

$$h = \frac{q_z}{(T_s - T_f)} \tag{17}$$

where q is the local heat flux in the z direction, T_s is the local solid temperature and T_f is the local fluid temperature. The heat transfer coefficients are shown in surface plots in Figure 3.5, in which the fluid inlet velocity was 20 m/s. The peak heat transfer coefficient for the circular array in Figure 3.5 is 427 kW/m^{2}K and 452 kW/m^{2}K for the square array. The average heat transfer was then calculated for the entire 1 mm x

1 mm impingement zone. The average heat transfer coefficient at 20 m/s jet velocity for the circular array was 302 kW/m^{2}K and 323 kW/m^{2}K for the square array.

3.1.4 Computational Domain

Quarter symmetry of the microjet assembly was used for computational efficiency. Symmetry boundary conditions were defined as appropriate on the mirrored boundaries. The computational domain was meshed with free tetrahedral elements. In order to capture large temperature gradients near the heater segments and velocity gradients near the microjet orifices, mesh size was varied while keeping the computational time within 1-2 hours. The mesh in different regions is shown in Figure 3.6.

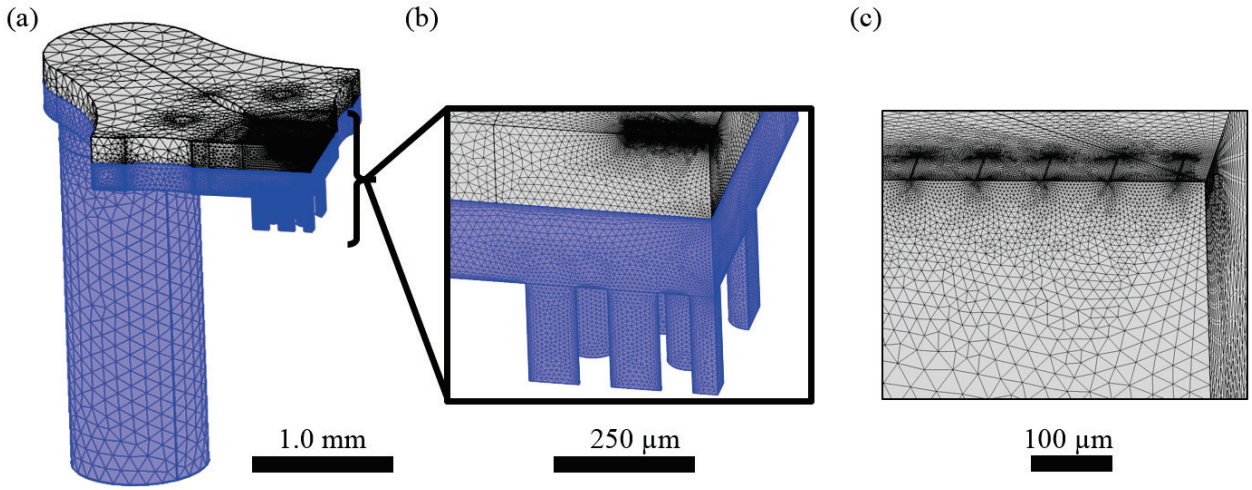

Figure 3.6: (a) Computational meshing scheme of the entire microjet assembly to capture large temperature gradients in the integrated heater and velocity gradients near the microjet orifices. (b) Higher magnification depiction of microjet and heater substrate mesh. (c) Highest magnification to show the mesh near the high resistance fingers.

For the fluid subdomain, a mesh size range of 6–25 µm and maximum element growth of 1.05 was used within and near the microjets. Downstream near the exit ports, the mesh size ranged from 25–129 µm with a maximum element growth rate of 1.1. The solid subdomain used elements between 12–25 µm with a maximum growth rate of 1.1. Each subdomain used corner refinement with an element size scaling factor of 0.35. Additionally, the fluid subdomain used boundary layer elements to more accurately capture the steep velocity and temperature gradients adjacent to the solid subdomain. The final mesh consisted of 1.3×10^6 elements.

Of particular note, even with the turbulence effects, numerical analysis of the single phase microjet system was considerably more tractable and computationally efficient than multiphase approaches. The model was solved on a workstation-class desktop with COMSOL's default convergence criteria in 1.5 hours.

3.2. Flow Visualization

The COMSOL model also allows for visualization of the flow dynamics occurring in the array of microjets. Streamlines (Figure 3.7a) were used to illustrate the fluid path from the orifice to the exit ports. For this illustration, the fluid inlet velocity was set to 20 m/s and 40 fluid streamlines were used. The streamlines show the fluid entering the cavity at uniform velocity, decreasing in velocity in the stagnation regions, and decreasing to very low velocities in the vicinity of the exit ports. A sliced view through four microjets at the center of the microjet array (Figure 3.7b) was used to visualize the flow phenomena discussed in Chapter 2. For this simulation, the inlet velocity was also set to 20 m/s.

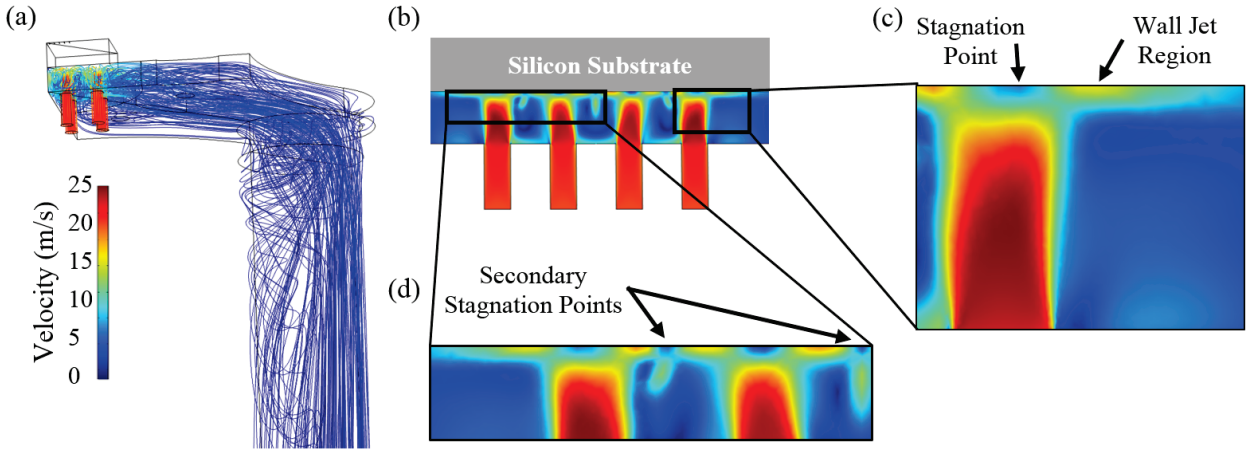

Figure 3.7: (a) Fluid streamlines for the 20 m/s fluid inlet velocity. (b) Sliced view of the microjet assembly showing the behavior of four microjets. (c) Higher magnification view of a single microjet behavior at the edge of the array. (d) Higher magnification view of secondary stagnation points between two adjacent microjets. Fluid is water.

Figure 3.7c, which shows a single microjet at the edge of the array, allows the visualization of the three flow regions discussed in Chapter 2 (the potential core/mixing layer, the stagnation/impingement zone, and the wall jet region). The potential core is observed at the jet centerline, where the fluid velocity remains approximately equal to the fluid inlet velocity. The lower-velocity mixing layer, at the edge of the potential core, is observed as the widening of the velocity profile due to viscous interactions with the surrounding fluid. The stagnation point is identified at the intersection of the potential core and the impingement surface. At the stagnation point, the fluid velocity decreases to zero, indicating a high-pressure region. The stagnation region extends vertically and radially outward from the stagnation point. As shown in the heat transfer coefficient maps in Section 3.1.3, the stagnation point is where the highest amount of heat transfer occurs due to suppression of the thermal boundary layer. Lastly, the flow is redirected parallel to the impingement surface in the wall jet region and a boundary layer develops.

In Figure 3.7d, a higher magnification view shows the jet-to-jet effects that occur within the array. As identified in the figure, secondary stagnation points occur between two primary stagnation points. At the

secondary stagnation points, adjacent wall jets interact and the flow is directed away from the surface. The secondary stagnation points exhibit lower heat transfer performance. An additional observation from the fluid velocities is that the primary stagnation points of the central microjet is pushed outward. This effect could be due to the lack of fluid exit ports within the array itself. The effect could be mitigated through more highly optimized geometry, such as slightly increasing the jet-to-jet and jet-to-target distances.

The numerical model was also used to visualize fluid flow dynamics that occur within the submerged cavity at various flow rates. For this study, the jet velocity was adjusted from 10, 15, 20, and 25 m/s.

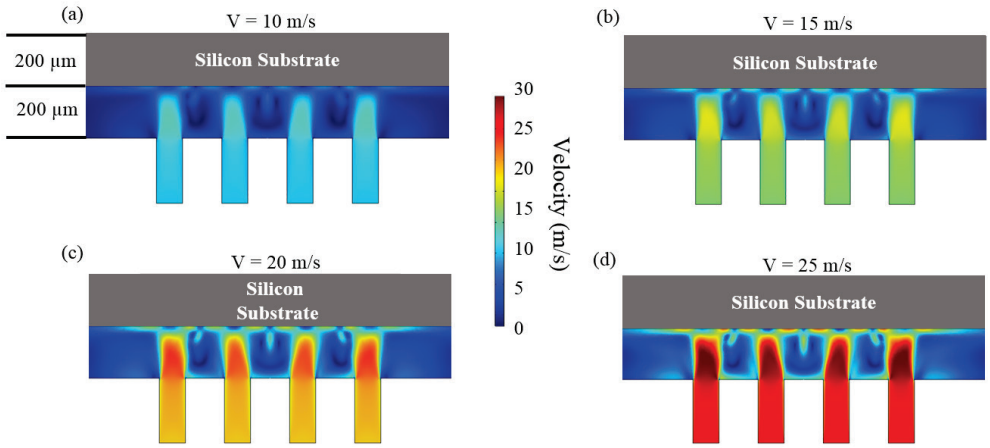

Figure 3.8: Maps of fluid (water) velocity magnitude with a fixed scale at (a) 10 (b) 15 (c) 20 (d) 25 m/s.

3.3. Validation with Empirical Correlations

Modeling results were compared with previous experimental work to evaluate the accuracy of the numerical model. The square array geometry compared well with microjet array geometry from the study of Michna et al. previously discussed in Section 2.2 [57]. The jet array configuration was the same (4 x 4), the diameter was slightly smaller (100 µm compared to 112 µm), the jet-to-jet spacing was equal (250 µm), the jet-to-target spacing was equal (200 µm), and the area ratio was within the range of ratios studied (0.126 within 0.036-0.35). Water was used as the working fluid in both the Michna et al. study and the model developed in this thesis. Lastly, the Reynolds numbers studied varied from 50 to 3500. The correlation resulting from this work is shown below in Equation 12.

$$Nu_d = 0.675 Re_d^{0.55} Pr^{0.243} \cos(5.416 A_r - 1.259) \quad (18)$$

The correlation includes a term to relate the effect of area ratio. To compare the modeling results with this work, the inlet velocity was varied from 0.5 to 37 m/s, resulting in Reynolds numbers from approximately 50 to 3500, to calculate the average heat transfer coefficient at each jet velocity. The Nusselt number and Reynolds number were calculated for these results for comparison with the Michna et al. correlation.

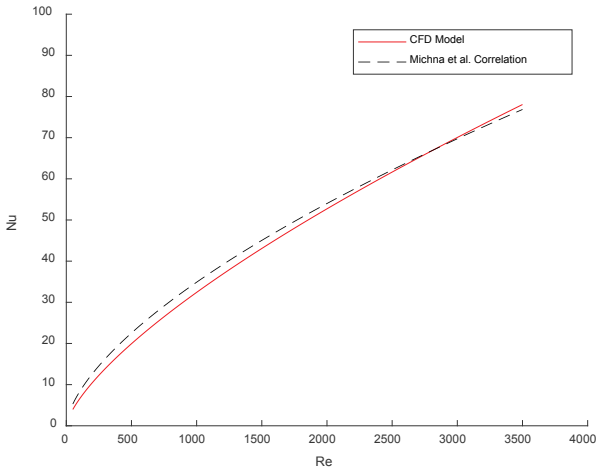

Figure 3.9: Comparison of Nu vs. Re of the model and Michna et al. correlation [57].

The modeling results showed strong agreement with the Michna et al. experimental correlation, particularly in the range of $1000 < Re < 3000$. The modeling results of this study were within 7% of the experimental Nusselt numbers of Michna et al. in this range of parameters. The Reynolds number dependence, from a data fit, was slightly higher for the CFD modeling results with $Nu \propto Re^{0.67}$ compared to $Nu \propto Re^{0.55}$ for the experimental results. The higher Reynolds dependence was closer to values seen by Fabbri and Dhir with $Nu \propto Re^{0.78}$ [53] and Brunschwiler et al. with $Nu \propto Re^{0.73}$ [54]. The Reynolds dependence is also consistent with a predictive model developed by Lindeman et al, which used $Nu \propto Re^{0.7}$ [65].

3.4. Chapter Summary

In Chapter 3, a numerical model of the microjet assembly (described in Chapter 2) was built to analyze the conjugate fluid dynamics and heat transfer. The fluid subdomain was determined to be in the turbulence regime based on the Reynolds number and cavity geometry, and the k-ω turbulence model was used to solve the conservation of mass, momentum, and energy equations. The boundary conditions for the fluid were a specified jet velocity and zero pressure condition on the exit ports. The solid subdomain included the integrated heater geometry, to which an applied heat flux was applied as a boundary condition. In total, the model consisted of 1.3×10^6 elements and took approximately 90 minutes to compute. The numerical model was used to predict the heat transfer coefficient occurring at the impingement surface. The predicted heat transfer coefficient showed strong agreement with the Nusselt correlation of Michna et al. [57] for a similar designed array over the same Reynolds numbers. Lastly, the flow dynamics within the microjet assembly were visualized with the model, highlighting the three flow regimes: the potential core/mixing layer, the impingement/stagnation zone, and the wall jet region.

4. Experimental Setup and Pressure Drop Analysis

An experimental flow loop was built to deliver, manipulate, and measure both electrical power and fluid flow to the microjet assembly in order to characterize its fluidic and thermal performances. The microjet assembly, seated in a test fixture, was installed in a closed flow loop and connected to a recirculating chiller to supply the microjet orifices with water at controllable flow rates and temperatures. The flow loop was instrumented to collect fluidic flow data including the volumetric flow rate, inlet temperature, outlet temperature, upstream pressure, and downstream pressure. The experimental setup also included equipment to supply voltage across the device and to measure the dissipated power. Lastly, the experimental setup included optical access to measure the surface temperature using micro-Raman thermography, which will be discussed in Chapter 5. The experimental setup was designed for extensive characterization of both thermal and hydraulic performance of the embedded microjet impingement system.

4.1. Flow Loop

Throughout the jet impingement literature, several types of experimental flow loops have been constructed to characterize and measure the heat transfer performance of the system. The purpose of the flow loop is to provide coolant to the jet orifices at a specific flow rate to achieve a desired jet velocity at the orifice exit. One of the primary design choices for the flow loop was whether it would be an "open loop" or "closed loop" system. In an open loop arrangement, a pressure gradient drives fluid from a supply tank at a higher pressure to a different receiving tank at a lower pressure. Browne et al. and Michna et al. pressurized the upstream tank with helium gas to drive degassed, deionized water to a receiving tank in their experiments [56-57].

The alternative method to deliver water to the jet orifices is a closed flow loop arrangement. In this type of system, the fluid is continually recirculated throughout the loop. It eliminates the supply and receive tank, but involves adding a pump to create a pressure driven flow and a heat exchanger to cool the heated liquid back to the desired coolant temperature. Fabbri et al. used a variable speed gear pump and a heat exchanger to achieve a specified water temperature [53]. Ditri et al. used a heated reservoir and pump to supply the 40% propylene glycol, 60% water (PGW) coolant [38]. Gambin et al. used a gear pump to supply the PGW coolant to the microjet manifold [35].

A closed flow loop configuration was selected for the experimental investigation of the microjet performance in this study for several reasons. The primary advantage of the closed flow loop is that since the liquid is continually recirculated, it allows for extended testing to be performed. This enables two dimensional thermal scans, which take several minutes, of a test device with jet impingement. This

characteristic also allows for lifetime testing, exceeding 1000-hours, to investigate the effects of clogging and erosion. Lastly, the closed flow loop configuration allows for greater control of the fluid temperature. The flow loop, shown in Figure 4.1, included instrumentation for analyzing both the thermal and hydraulic performance.

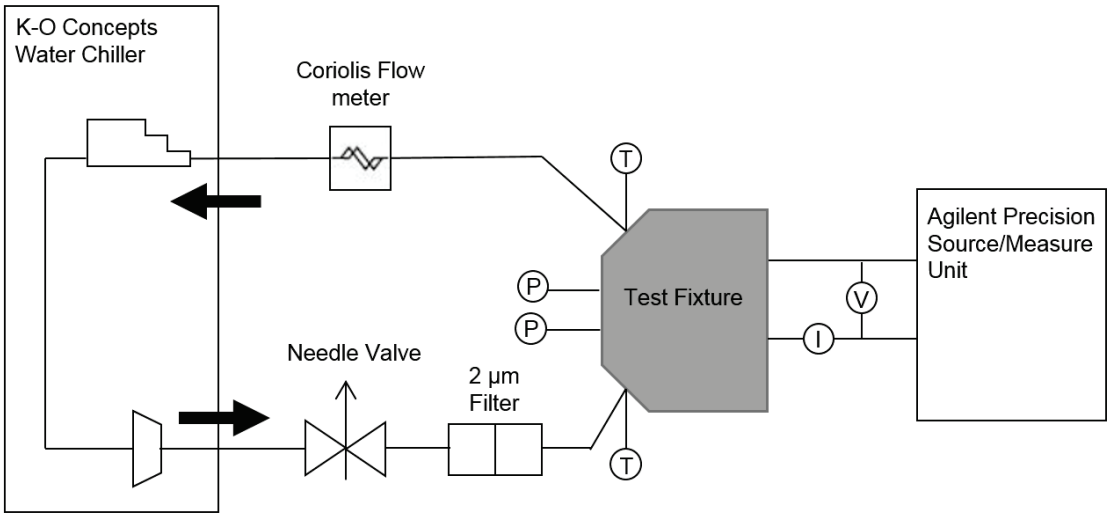

Figure 4.1: Closed flow loop used in the experimental testing.

In the flow loop, the recirculating chiller delivered water to the microjets, which were contained in a test fixture. The needle valve provided fine flow rate control. The sintered metal filter eliminated particles larger than 2 µm from the flow loop to prevent clogging of the microjet orifices and to protect the system pump. The test fixture was instrumented to record the temperature and pressure of the fluid both upstream and downstream of the microjet orifice array. The Coriolis flow meter was used to determine the flow rate. To supply power to the device, two custom probe micro-manipulators were adjusted to make contact with the integrated heater contact pads and supply voltage from the source/measure unit.

4.1.1. Recirculating Chiller and Flow Rate Control

The recirculating chiller (LCR-8-G2, K-O Concepts) was equipped with both a compressor and a positive displacement pump and delivered water to the microjets with a 20 °C set point and ±0.1 °C process control. The chiller was capable of cooling an 800 Watt heat load with a rotary compressor. The standard positive displacement pump was capable of supplying up to 4.16 liters per minute (lpm) at 100 psi. To control the flow rate, an integral bonnet needle valve (SS-1RS6, Swagelok) was installed in the flow loop. The needle valve could adjust the flow rate within 0.01 lpm through the range of 0.03 lpm to 0.30 lpm. Additionally, a ball valve (SS-44S6, Swagelok) was installed in the flow loop to provide an emergency shutoff option.

4.1.2. Flow Meter

The Coriolis flow meter (Micro Motion CMFS025M, Emerson) was used to characterize the mass flow rate in the loop. Within the Coriolis meter, the flow is split into two tubes, which oscillate as a result of the flow driving a magnetic coil. As the tubes oscillate, voltage is generated in the form of a sine wave. The time delay between the two sine waves is proportional to the mass flow rate. The resulting mass flow rate is accurate within 0.1% over the full scale, per the manufacturer's data sheet. Although the accuracy is high, the Coriolis meter is expensive and requires rigid mounting. The Coriolis flow meter was used for baseline pressure vs. flow rate characterization, but a more mobile option was needed for transportation to MIT campus for micro-Raman temperature measurements. The paddle flow meter (FTB321, Omega) presents a more portable volumetric flow rate option. The paddle flow meter operates with an infrared light beam detecting the rotational speed of the paddle wheel as it is accelerated by the flow. The drawback to the paddle wheel flow meter is decreased accuracy, 6% over the full scale. A comparison was performed between the Coriolis flow meter and the paddle wheel flow meter over the range of interest from 0.03 lpm to 0.30 lpm shown below in Figure 4.2.

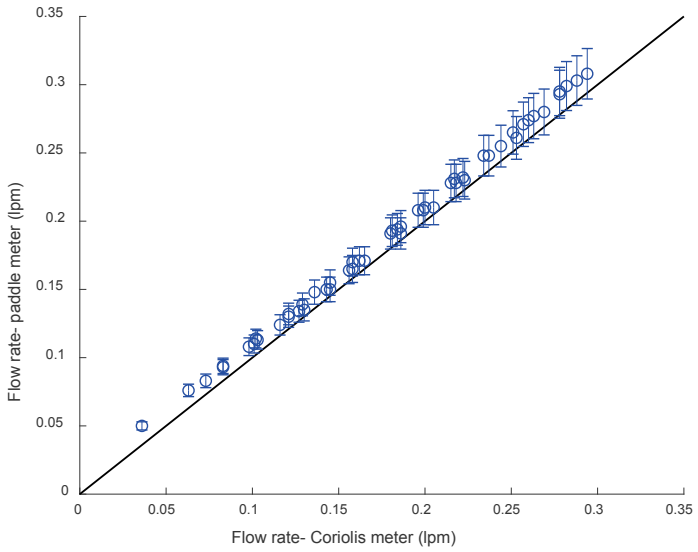

Figure 4.2: Comparison of the Coriolis flow meter and paddle flow meter.

As seen in the comparison plot, the paddle flow meter measurements were offset above the Coriolis flow meter measurements. The reason for the disagreement could be slight error in the calibration of the flow meter from the factory. Most of the thermal performance measurements were taken with flow rates between 0.1 and 0.2 lpm, where the paddle flow meter was well within the advertised 6% error. The flow meter comparison study showed that the paddle flow meter, which is relatively inexpensive and flexible to

mount, serves as an effective flow meter for the campus thermography measurements where the flow rate was held constant throughout the testing.

4.1.3. Filtration

Clogging of the microjets and erosion of the electronic device backside present two practical challenges for adoption of microjet cooling technology. Clogging occurs when particles are introduced into the flow loop (from outside, or generated within the loop) impeding flow through one of the 100-116 μm diameter jets. A consequence of clogging would be a sudden increase in the required driving pressure of the system, due to the corresponding decrease in microjet cross sectional area. Alternatively, with a fixed driving pressure, the flow rate through the microjets would decrease. More importantly, in both cases, clogging can adversely affect the array's ability to provide uniform cooling of the electronic device.

Flow induced erosion is often cited as a concern with employing microjets due to their impact with the backside of the electronics at relatively high jet velocities. The continual impacts of contaminant particles may erode the wall and cause anomalous device behavior, or, in severe cases, eventual leakage of fluid out of the device. Ditri et al. used a computational approach (Lagrangian Particle Tracking) to explore the effects of erosion for particle sizes ranging from 0.5 to 5.4 μm on the back of the gold ground plating [38]. They determined that erosion was insignificant for steel particles less than 2 μm mean diameter.

To mitigate effects of both clogging and erosion, sintered metal filters (SS-6TF-2, Swagelok) were used to filter out particles larger than 2 μm from the flow loop. The sintered metal filters were Tee-type, meaning the filter element could be replaced without removing the filter body from the system. The filters are available in 0.5 to 90 μm nominal pore sizes.

4.1.4. Test Manifold

A custom manifold was designed and machined to hold the microjet assembly in place while allowing surface temperature measurements to be taken of the integrated heater. The manifold stack-up is shown in Figure 4.3 with the main components: the test fixture, nitrile O-rings, the microjet assembly, and the cover plate.

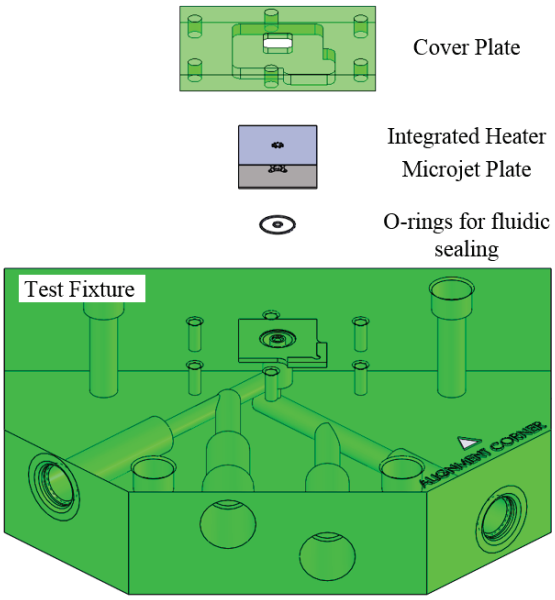

Figure 4.3: Translucent, exploded view of the test fixture and manifold stack-up.

The test fixture is made of polyether ether ketone (PEEK). Peek is a dimensionally stable, high melting point (T_{mp} = 343 °C) plastic. It was chosen for its low thermal conductivity (k = 0.25 W/m-K) in order to minimize conduction losses in the system. The main features of the test fixture are the fluid inlet and outlet channels, which are bored into the 45° faces. Tee fittings (SS-600-3TTF, Swagelok) were secured to the inlet and outlet channels. Rugged pipe plug Type K thermocouples (TC-K-NPT-U-72, Omega) were inserted into the Tee fitting, in order to provide inlet and outlet fluid temperatures at the center of the channels. Pressure taps, shown at the front face of Figure 4.3, connected to the fluid inlet and outlet channels. Pressure transducers were inserted into the pressure taps in order to measure the fluid upstream and downstream of the microjet array. Upstream, the pressure transducer was rated to 100 psia (PX329-100A5V, Omega), and downstream, the pressure transducer was rated to 30 psia (PX329-030A5V, Omega). The inlet fluid channel met with an inner cylinder bored into the topside of the test fixture. The inner cylinder encapsulated the entire microjet array, which was aligned by a raised corner of the fixture. An outer annulus captured the exit port effluent of the microjet array, routing it to the fluid outlet channel on the opposite side of the fixture. On the top of the fixture, a 20 mm x 20 mm platform served as the base for the microjet assembly. A detailed Solidworks drawing of the fixture is attached as Appendix A.

O-rings, made of Buna-N, were used to provide fluidic seals to isolate the incoming fluid from the outgoing effluent. The inner O-ring had an inner diameter of 0.069" (R00069-020-70BNB, Apple Rubber) and the outer O-ring had an inner diameter of 0.315" (R00315-020-70BNB, Apple Rubber). The microjet assembly was manually aligned in the center of the fixture above the center annulus with the raised corner of the platform. A 50 mm by 35 mm cover plate was designed to hold the microjet assembly in compression

(against O-rings) while water was supplied to the microjet orifices. The cover plate contained a well on its underside, which had a depth chosen to cover the raised platform on the fixture, the microjet assembly, and the compression of the O-rings. The cover plate was secured with 6 fasteners. The cover plate was also designed with a 12.5 mm x 7.5 mm optical viewport. This viewport allowed both for application of DC power through the use of probe manipulators and for the Raman temperature measurement discussed in Chapter 5.

4.1.5. DC Power and XY Stage Mount

To provide heat flux to the device through Joule heating, DC power was applied with custom probe micro-manipulators. The 0.0005" tungsten probe tips (SPAR11-51-003, Rucker and Kolls) were used to connect to the contact pads of the integrated heater. The micro-manipulators were connected to a precision source/measure unit (B2902A, Agilent), which applied constant voltage (V) across the device and measured the resulting current (I), which were then used to calculate the dissipated power (P).

$$P = I \cdot V \tag{19}$$

A key challenge in using the micro-manipulators was contact with the device under the working distance, 8.3 mm, of the microscope objective. The probe contact with electrical pads, even with the microscope objective constraint, was achieved through altering the height of the manipulator base stands and adjusting the angle of contact within the manipulator arms.

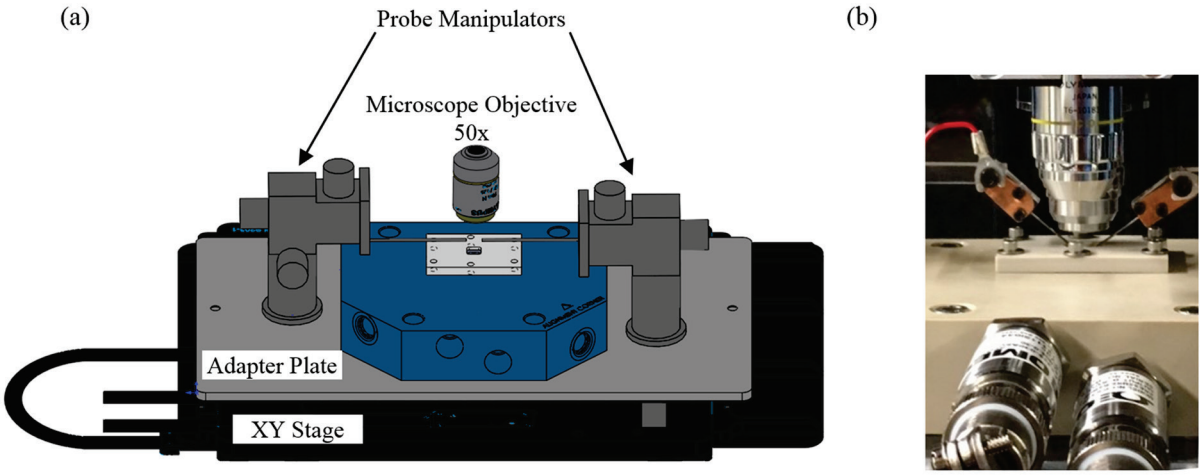

Figure 4.4: (a) Solidworks rendering of microjet assembly mounted to XY stage. (b) Experimental picture showing the clearance with the microscope objective and design of probe manipulators.

The test fixture and probe manipulators were mounted to a movable XY stage (MLS203-1, Thorlabs) through the use of an adapter plate shown in Figure 4.4a. The XY stage has a range of 110 mm x 75 mm and can be moved in 0.1 μm increments. The XY stage was connected to a brushless DC servo controller

(BBD202, Thorlabs) with control of the spatial position through the Kinesis software package. The movable XY stage allowed temperature measurements to be taken in scanning sequences to provide a spatial map of the surface temperature.

4.1.6. Data Collection

Fluidic data measurements were taken with a multifunction switch/measure unit (34980A, Keysight). The temperature of the fluid inlet and outlet channels were collected from the Type K thermocouples. The fluid pressure of the inlet and outlet taps were collected from the pressure transducers. The Keysight software Benchlink Data Logger 3 was used to collect and analyze the experimental data. Measurements were taken while the system was at steady state and the sampling rate of the data collection was 1/10 Hz. Lastly, the volumetric flow rate, displayed on the output screen of the digital flow meter, remained constant throughout the temperature mapping sequences. The flow rate was recorded before the experiments and monitored periodically during the experiments. The source/measure unit was used to record the voltage and resulting current in the device during operation.

4.2. Pressure Drop Analysis

An important metric in implementing microjet cooling technology is the pressure drop through the orifice plate. The pressure drop (ΔP) was calculated by subtracting the fluid outlet pressure (P_{out}) from the fluid inlet pressure (P_{in}), measured with the pressure transducers placed in the press ure taps of the fixture.

$$\Delta P = P_{in} - P_{out} \tag{20}$$

The pressure drop was used to calculate the required ideal pumping power. The ideal hydraulic power (Q_{pump}), often expressed with the unit Watts, is related to the pressure drop across the jet orifice plate and the total volumetric flow rate in the loop, $\dot{V}$, calculated with

$$Q_{pump} = \Delta P \dot{V} \tag{21}$$

The magnitude of the pumping power to achieve certain heat transfer performance is of interest for meeting certain electronic packaging constraints such as volume requirements or energy consumption.

4.2.1. Pressure Drop versus Flow Rate

A characterization was performed to relate how the pressure drop varies with system flow rate. In the experiment, the needle valve was adjusted to achieve fine flow rate control, which was measured with the Coriolis flow meter. The pressure drop was calculated from the pressure transducers in the taps of the fixture. The results for both the square array and the circular array are shown below in Figure 4.5. The

second order polynomial fits of the pressure drop in psi to flow rate in liters per minute are shown in the upper left hand corner of each plot along with the quality of the fit.

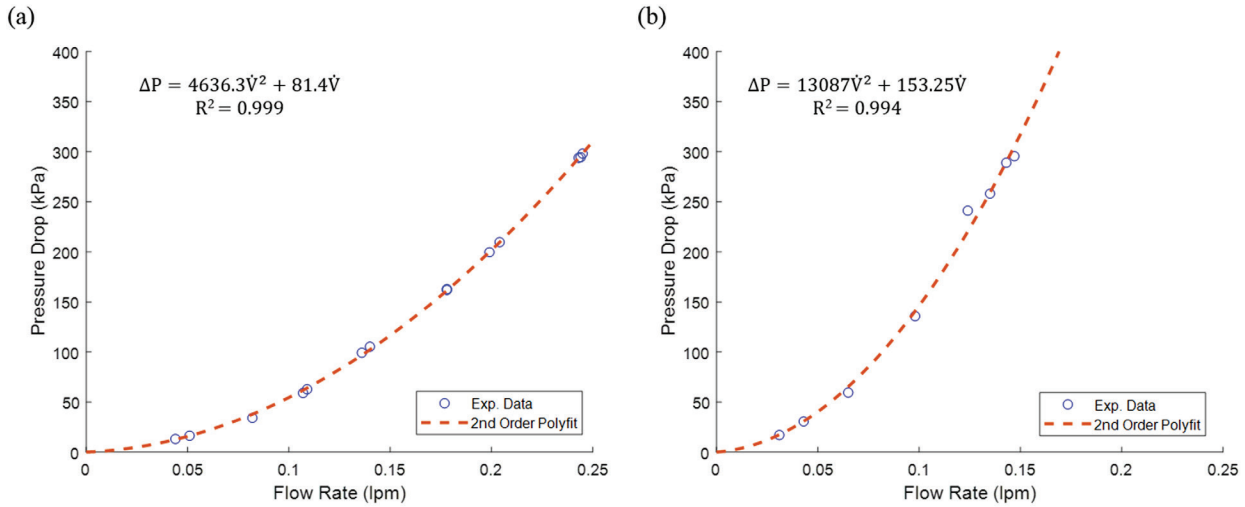

Figure 4.5: (a) Pressure versus flow rate data for the circular array. (b) Pressure versus flow rate data for the square array. Fluid is water.

As noticed in the curves and polynomial fit equations, the pressure drop was higher through the square array compared to the circular array for a particular flow rate. This higher pressure drop occurs due to the square array having a smaller cross sectional area than the circular array because of both the decreased jet diameter and number of jets. The pressure drop as a function of the jet velocity was calculated by dividing the flow rates by the total cross sectional area for each microjet array.

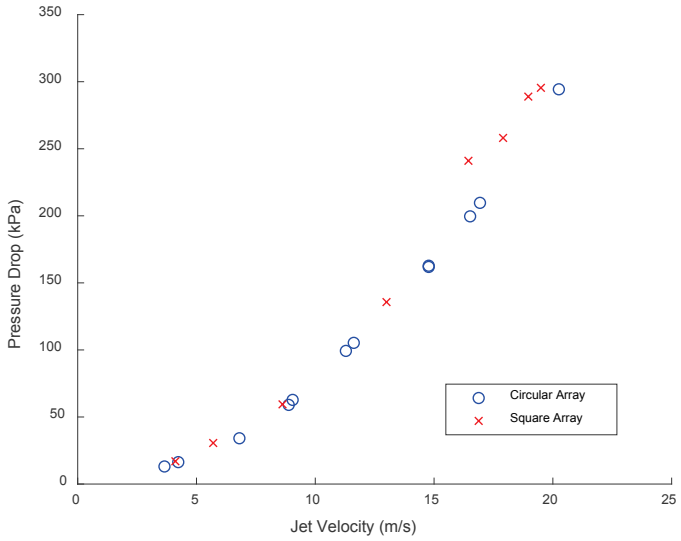

Figure 4.6: Pressure drop versus jet velocity for the square and circular arrays. Error bars are smaller than the data markers. Fluid is water.

As observed in Figure 4.6, the pressure drop to achieve a jet velocity was approximately equal for both the square array and the circular array. The pressure drop develops based on the constriction in size as the tube size decreases through each of the jet orifices. The results of Figure 4.6 make physical sense because the calculation of the jet velocity normalizes the system flow rate by the cross sectional area of the jets. The aberration that occurs at the higher jet velocities may be due to variations in etching of the jet orifices or variations in the surface roughness on the backside of the heater.

4.2.2. Discharge Coefficient Calculation

The mechanism for the pressure drop through the microjets can be quantified with the discharge coefficient (C_D). The discharge coefficient is used in nozzle characterization, and represents the ratio of the actual discharge to the theoretical discharge. The discharge coefficient relates the average velocity at the orifice exit to the pressure drop experienced across the orifice plate according to

$$C_D = \sqrt{\frac{\rho V^2}{2\Delta P}} \tag{22}$$

where ρ is the fluid density, V is the jet velocity, and ΔP is the pressure drop. The discharge coefficient was calculated based on the pressure drop and flow rate data, and is shown for both the circular and square arrays in Figure 4.7. The error bars are calculated using the Kline and McClintock vector summing technique [66].

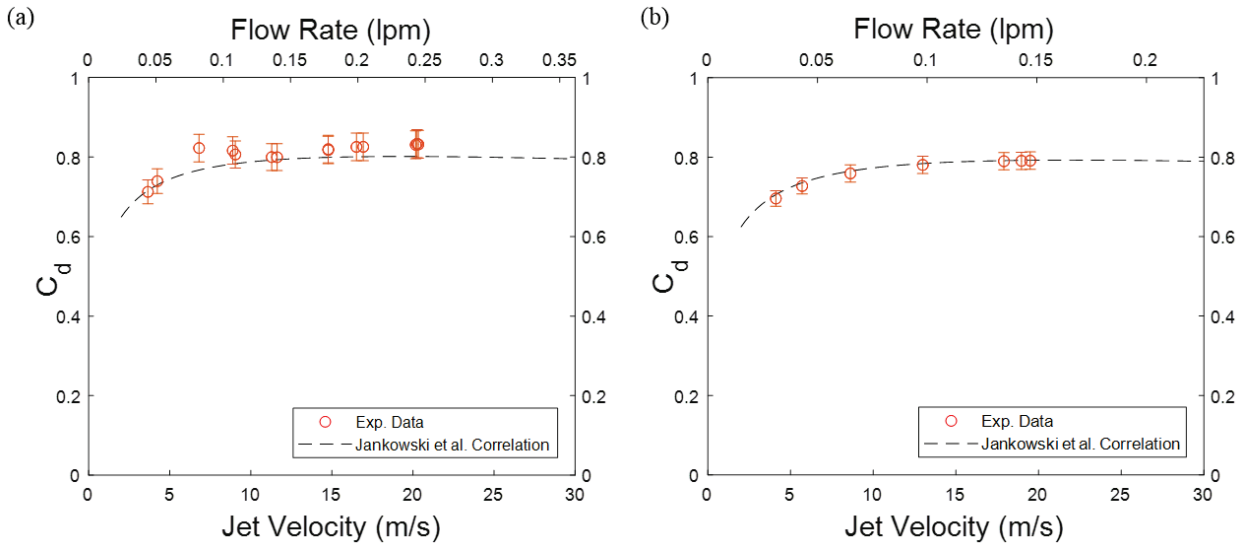

Figure 4.7: Discharge coefficient plotted versus jet velocity on the bottom x-axis and system flow rate on the top x-axis for the (a) circular array (b) square array.

Also included in Figure 4.7 is the discharge coefficient calculated by a model developed by Jankowski et al. [67]. The Jankowski et al. characterized pressure drops through micro-orifices in which diameters

ranged from tens to hundreds of microns. Specifically, the model seeks to address flow through orifice tubes, where the length-to-diameter (L/D) ratio is greater than zero. For the arrays in this thesis, the length-to-diameter ratios were 2.15 for the circular array and 2.5 for the square array. The model resulting from Jankowski et al. is a semi-empirical correlation for describing the pressure losses through sharp edged orifices.

$$C_D = \left(\frac{1}{C_{D,S}^2} - f\frac{L}{D} \right)^{-1/2} \tag{23}$$

Shown in Equation 23, the model developed by Jankowski sums the two main contributors to the pressure drop in series: pressure drop through a sharp-edged orifice and pressure drop due to friction that occurs for developing flow through walls of a finite length orifice. The two contributions are calculated separately and summed using the relationship shown above. The sharp-edged orifice pressure losses are calculated from a four parameter correlation for configurations with small diameter ratios (where the upstream diameter is significantly larger than the cumulative cross sectional diameter of the microjets). The friction losses depend on the ratio of orifice length to orifice diameter. The Jankowski model predicts the discharge coefficient within 7% for each data point. The experimental discharge coefficients may vary slightly, due to a slight taper that occurred during fabrication, which decreased the sharpness of the orifices.

4.3. Chapter Summary

In Chapter 4, an experimental flow loop was built to measure the fluidic and thermal performance of the microjet cooling system. A closed flow loop design was chosen to enable extended thermal scans and lifetime testing for erosion. The loop itself consisted of a pump to circulate flow, needle valve to control the flow rate, flow meter to measure the flow rate, and inline filter to remove particles larger than 2 μm from the flow loop. The microjet assembly was seated in a test fixture, made of PEEK plastic, with sensors to measure the pressure and temperature upstream and downstream of the microjets. The test fixture was then integrated with micro-manipulators to deliver power and optical access for micro-Raman thermography measurements (discussed in the following chapter). The fluidic performance was evaluated with a plot of the pressure drop against flow rate for both the square and circular arrays. Lastly, the discharge coefficient was calculated to relate the pressure drop to the jet velocity. The experimental results showed strong agreement with a semi-empirical model from Jankowski et al. [67], which predicted discharge coefficients in micro-orifices with sharp edges.

5. Raman Thermography- Theory and Experiment

To examine the performance of the embedded microjets, micro-Raman thermography was used to measure the surface temperature profile of the fabricated test device. Micro-Raman thermography is one of the most promising techniques to overcome the limited spatial resolution of electrical techniques and IR thermography by using visible laser excitation with a diffraction limited spot size of ~1 μm [40,68]. Micro-Raman thermography also offers the advantage of being a non-contact measurement method, with limited sample preparation. Variations of this technique have become increasingly popular for assessing temperature in semiconductor devices such as silicon [42,69] and GaN HEMTs [70-71].

5.1. Raman Theory

Light interacts with matter through several interactions: reflection, absorption, transmission and scattering. Within scattering, the dominant mechanism is Rayleigh, or elastic, scattering, in which the energy of the photon is unchanged. A second type of scattering, termed Raman scattering, was discovered by C.V. Raman in 1928. In his seminal paper published in *Nature*, Raman discussed his experimental setup in which he focused sunlight through a refracting telescope and blue-violet filter to achieve a violet light source. The violet light passed through and interacted with a liquid sample, which extinguished the track of light. When Raman placed a yellow filter between the observer and the sample, the track of light reappeared. He concluded from these experiments the existence of a "modified scattered radiation" [72]. The ability to use Raman scattering as an analytic tool in modern research is the result of replacing the sun and filters with a single wavelength diode laser and replacing human eye observation of the track of light with a high-resolution spectrometer and CCD camera. Raman spectroscopy is widely used for identifying molecular structures and examining electrical and mechanical behavior in semiconductors.

5.1.1. Quantum Theory

Quantum theory specifies that vibrational energy levels are quantized; that is, they are discrete states and cannot be continuous. Spectroscopy provides insight into the transition from one discrete vibrational state to another. When a photon interacts with a molecule during scattering, it distorts the molecule's surrounding electron cloud and forms a temporary "virtual state" with the molecule. This virtual state is highly unstable and the photon is reradiated almost instantaneously. The energy of the incoming photon is defined by the following relationship

$$E = h\nu = \frac{hc}{\lambda} \tag{24}$$

where h is Planck's constant, ν is frequency, c is the speed of light and λ is wavelength. The majority of scattered photons have the same energy as the incoming photons during the Rayleigh scattering case in Figure 5.1a. In Rayleigh scattering, the molecule (initially in the ground state), is radiated with a photon to form a momentary virtual state, and then de-excites back to the ground state and the photon has the same energy as before the interaction.

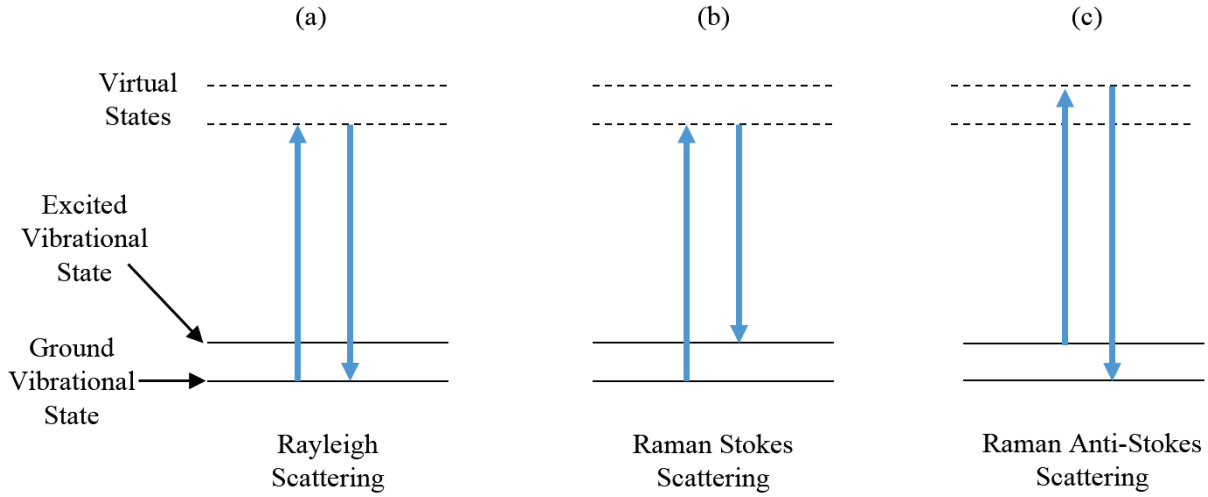

Figure 5.1: Energy band diagrams for scattering types: (a) Rayleigh (b) Raman Stokes (c) Raman Anti-Stokes.

However, approximately one in every 10^6-10^8 scattered photons is reradiated at a different energy level in what is known as Raman scattering. Raman scattering consists of either Stokes (Figure 5.1b) or anti-Stokes (Figure 5.1c) scattering. In the Raman Stokes scattering case (Figure 5.1b), the molecule is initially in the ground state and the photon transfers energy to the molecule, so when the molecule de-excites, it is in a higher vibrational state. As a result of the interaction, the scattered photon has lower energy, or a longer wavelength than the incident photon. The Raman Stokes process can also be understood as the emission of a phonon.

In the Raman anti-Stokes scattering process (Figure 5.1c), the molecule is initially in the excited vibrational state and de-excites to the ground vibrational state. The resulting anti-Stokes scattered photon has a higher energy and a shorter wavelength than the incident photon. At room temperature, the majority of the molecule population is in the ground state, and Stokes scattering is more prevalent than anti-Stokes scattering. As will be discussed briefly in Section 5.2, the ratio of Stokes to anti-Stokes scattering can be used to deduce temperature based on the temperature dependent changes in population.

5.1.2. Physical Basis of Raman Spectrum Features

In Raman scattering, a photon with incident wavelength (λ_o) is scattered inelastically to a different wavelength (λ). In Stokes scattering, the wavelength is longer and in anti-Stokes, the wavelength is shorter.

The difference of the inverse wavelengths is calculated with Equation 25 shown below and is called the Raman shift, or wavenumber, with units of cm^{-1}.

$$\begin{matrix} Raman\ Shift \\ (Wavenumber) \end{matrix} = \frac{1}{\lambda_o} - \frac{1}{\lambda} \tag{25}$$

In most Raman spectroscopy systems, the light is dispersed in a spectrometer and captured by a CCD. The CCD array converts the intensity into an electric signal and a computer package computes the wavenumber and plots the intensity, measured in counts, versus the wavenumber on the x-axis, shown in Figure 5.2. Software then fits a Gaussian or Voigt profile to find the center of the peak position. The precision of a Raman peak position measurement depends on CCD pixel size and spectrometer optical characteristics including grating groove density, focal length, and slit width. Additionally, features of the Raman peak itself including intensity, linewidth, and effect of other peaks, can affect the precision of the measurement.

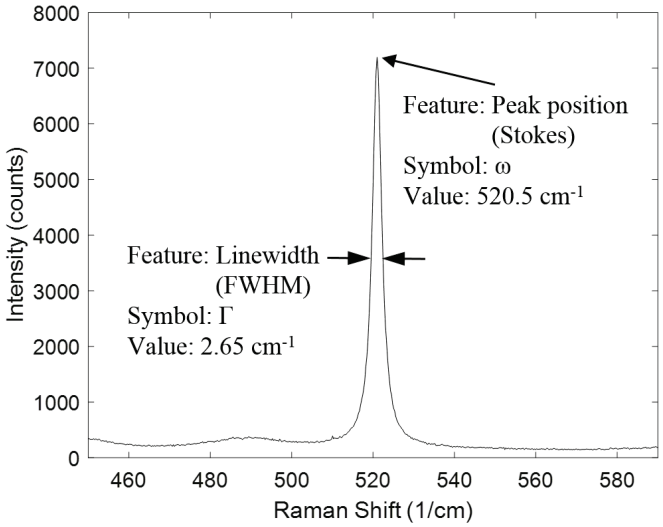

Figure 5.2: Sample spectrum of Si, showing peak at ~520 cm^{-1}.

In the plot, there is a clear peak position () with a centroid at ~520 cm^{-1}. This peak is material dependent, and thus changes depending on the material being examined. For example, diamond has one peak at 1330 cm^{-1}, TiO_2 has one peak at 144 cm^{-1}, and GaN has three peaks at 144, 568, and 734 cm^{-1}. The peak position is proportional to the phonon frequency for each optical phonon mode allowed by Raman scattering selection rules for the particular material.

The physical basis for the peak position has two major contributions: volumetric and phonon-phonon interactions. The volumetric contribution refers to changes in the interatomic forces in the crystal lattice of the material. These forces change due to changes in the equilibrium atomic positions as the material is heated (lattice expansion) or cooled (lattice contraction). The phonon-phonon interaction contribution

refers to changes to interatomic forces due to changes in phonon population. The phonon population is governed by the Bose-Einstein thermal distribution and thus changes based on temperature.

Of particular note, the volumetric aspect of peak position makes is susceptible to any changes in peak position including material stress/strain. The material stress/strain includes several types of strain including mechanical, thermoelastic induced, and piezoelectric strain [73]. The stress/strain effect on the peak position, when not properly accounted for, can result in bias errors when using the peak position to determine temperature [42].

The other key feature identified in Figure 5.2 is the Raman linewidth, or Full Width at Half Maximum (FWHM). The physical basis for the linewidth (Γ) is its inverse proportionality with the lifetime of the phonon mode. The Heisenberg uncertainty principle dictates that a photon's energy must be measured within a finite measurement time period to achieve specificity. The relationship between energy and measurement time is shown according to

$$\Gamma = \frac{\hbar}{\tau} \tag{26}$$

where Γ is the linewidth, $\hbar$ is the reduced Planck constant and τ is the phonon scattering time. The scattering time is dependent on microstructural defects, material boundaries, and phonon-phonon interactions. The dominant mechanism is phonon-phonon interactions, which directly depend on the Bose-Einstein distribution population. As temperature increases, phonon interactions T increase and the scattering time decreases, resulting in a wider linewidth [73]. The effects of both the peak shift and linewidth broadening at elevated temperatures are shown below in Figure 5.3. The Raman peak position shifted from 521 cm^{-1} to 520 cm^{-1} and the FWHM widened from 2.82 to 3.21 cm^{-1} as the temperature increased from 20 °C to 45 °C. The trends that occur in the Raman features, and their physical origins, are tabulated in Table 5.1.

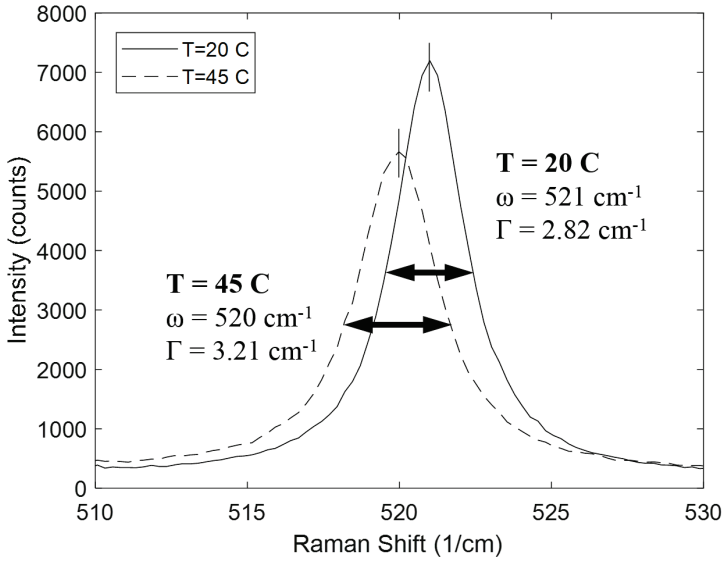

Figure 5.3: Raman spectra of silicon showing the peak position (ω) and linewidth (Γ) decreasing and widening, respectively, with an increase in sample temperature from 20 °C to 45 °C.

Table 5.1: Summary of Raman spectral feature trends, modified from [73].

Spectral Feature	Symbol	Increased Temperature Effect	Physical Basis for Change
Peak Position	ω	↓	Changes in interatomic forces due to volumetric and phonon-phonon interactions
Linewidth (FWHM)	Γ	↑	Decreased scattering time due to high population of phonons

5.2. Raman Temperature Techniques

Raman thermography is the applied use of Raman spectroscopy to measure the device temperature by measuring changes in the previously described features. The earliest studies of Raman thermography, such as Kuball et al. in 2002, used changes in the Raman peak position to measure the temperature [74]. An empirical correlation was used to determine the temperature dependence of the Stokes peak position

$$\omega = A(T_\omega - T_o) + \omega_o \tag{27}$$

where ω is the peak position at temperature T, ω_o is the peak position at reference temperature T_o, and A is a material coefficient experimentally obtained through calibration. With this method, the peak position (ω_o) was measured as a reference state and then the new peak positon (ω) was measured while the device was biased under power. As discussed in the previous section, the peak position is a function of the energy of the zone center optical phonons, and thus is influenced by interatomic forces or changes in the equilibrium atomic spacing. The challenge in using the peak shift method to measure temperature is that

the peak shift is a convolution of temperature and stress, which both influence the energy of the optical phonons.

When aware of the convolution of both stress and temperature effects on the peak position, there are several methods to achieve accurate temperature measurements. When multiple peaks are present in the material, for example GaN exhibits the E_2 (high), A_1 (LO), and E_2 (low) peaks, there are several methods to decouple the effects of both temperature and stress. Batten et al. [75] and Choi et al. [76] suggested a two peak fitting method to measure both temperature and thermoelastic stress using the E_2 (high) and A_1 (LO) modes according to

$$\Delta\omega_{E_2(high)} = K_{E_2(high)}\sigma + A_{E_2(high)}\Delta T \tag{28}$$

$$\Delta\omega_{A_1(LO)} = K_{A_1(LO)}\sigma + A_{A_1(LO)}\Delta T \tag{29}$$

where the additional terms K and σ refer to the biaxial stress coefficient and thermoelastic stress in the c-plane. The peak position dependence on stress and temperature was determined for both the E_2 (high) and A_1 (LO) modes. For these measurements, it is important to note that the reference state is the pinched OFF state to remove the effect of inverse piezoelectric (IPE) stress that occurs between the pinched OFF state and the zero bias state.

Bagnall et al. introduced that the peak position varies linearly with an additional term, the vertical electric field, from ± 5 MV/cm [77]. Understanding the physical contributions of temperature rise, inverse piezoelectric stress, thermoelastic stress and electric field, Bagnall et al. created a novel methodology for characterizing the physical state of the device [70]. The unique aspect of this approach, compared to the two peak method, is including the peak shift of the weaker E_2 (low) mode of GaN.

$$\Delta\omega_n = K_n\sigma + A_n\Delta T + B_n E_Z \tag{30}$$

n = E_2 (high), A_1 (LO), and E_2 (low) modes

where changes in the peak position of the three GaN modes are used to deduce the temperature rise, stress state, and vertical electric field of the device simultaneously. For each of the modes, the temperature rise coefficient (A) is determined experimentally, while the stress coefficient (K) and vertical electric field coefficient (B) are determined from density functional theory (DFT) calculations.

When only one Raman peak is available for the material, for example in Si, other features that are insensitive to stress can be used to deduce the operating temperature of the device. Beechem et al. reported using the linewidth technique to measure the operating temperature in both Si [42] and GaN [71] devices. This technique uses an experimental determination of the Raman linewidth dependence on temperature according to

$$\Gamma = B(T_\Gamma - T_o)^2 + C(T_\Gamma - T_o) + \Gamma_o \tag{31}$$

where Γ is the linewidth, T is the temperature and B and C are calibration constants. As discussed in Section 5.1, the Raman linewidth varies inversely with phonon scattering time, and thus the linewidth widens as the temperature increases. To use this technique, the linewidth at a reference state (Γ_o) is measured at the reference temperature (T_o) and then measured again when the device is powered.

Another method to achieve a stress independent temperature measurement is the ratio of the intensity of the Stokes Raman peak (I_S) to the intensity of the anti-Stokes peak (I_{AS}) calculated according to

$$\frac{I_S}{I_{AS}} = \left(\frac{\lambda_S}{\lambda_{AS}}\right)^4 exp\left(\frac{h\omega_o}{k_B T}\right) \tag{32}$$

where λ_S and λ_{AS} are the Stokes and anti-Stokes shifted scattered light, respectively [78]. Because this technique is solely dependent on phonon population, it is insensitive to stress. However, the collection of the weaker anti-Stokes intensity requires long integration times and additional experimental setup. This longer integration time makes taking multiple temperature measurements and spatial scans prohibitively time consuming. This thesis will focus on the peak shift and linewidth methods to measure the temperature of the device.

5.3. Micro-Raman and Experimental Optical Setup

Micro-Raman thermography, an extension of Raman thermography theory discussed in Sections 5.1 and 5.2, involves focusing a laser excitation source through a microscope to achieve a micron size spot on the sample. The Rayleigh scattered light is blocked with a notch or edge filter at the selected laser wavelength. The Raman scattered light is directed into a spectrometer, where it is dispersed into a spectrum and captured by the CCD array.

The micro-Raman measurements in this work, shown in Figure 5.4, were performed in the 180° backscattering configuration with a custom free space micro-Raman system consisting of a stabilized diode laser (SLM-FS, REO, λ_o = 632.9 nm), an optical microscope (Olympus BX41), and a 750 mm focal length spectrometer (Acton Spectra-Pro SP-2750, Princeton Instruments) with a 1800 G/mm grating. The spectrum was captured by a thermoelectric cooled CCD (PIXIS 400, Princeton Instruments). A 50x zoom, 0.55 numerical aperture (NA) microscope objective was used to focus the laser excitation on the sample. An appropriate dichroic beam splitter (LPD02-633RU-25, Semrock) and edge filter (LP02-633RU-25, Semrock) separated the Raman scattered light from the laser excitation. The Raman peak was calibrated with spontaneous emission lines of a neon calibration lamp (Oriel 6032, Newport Corporation).

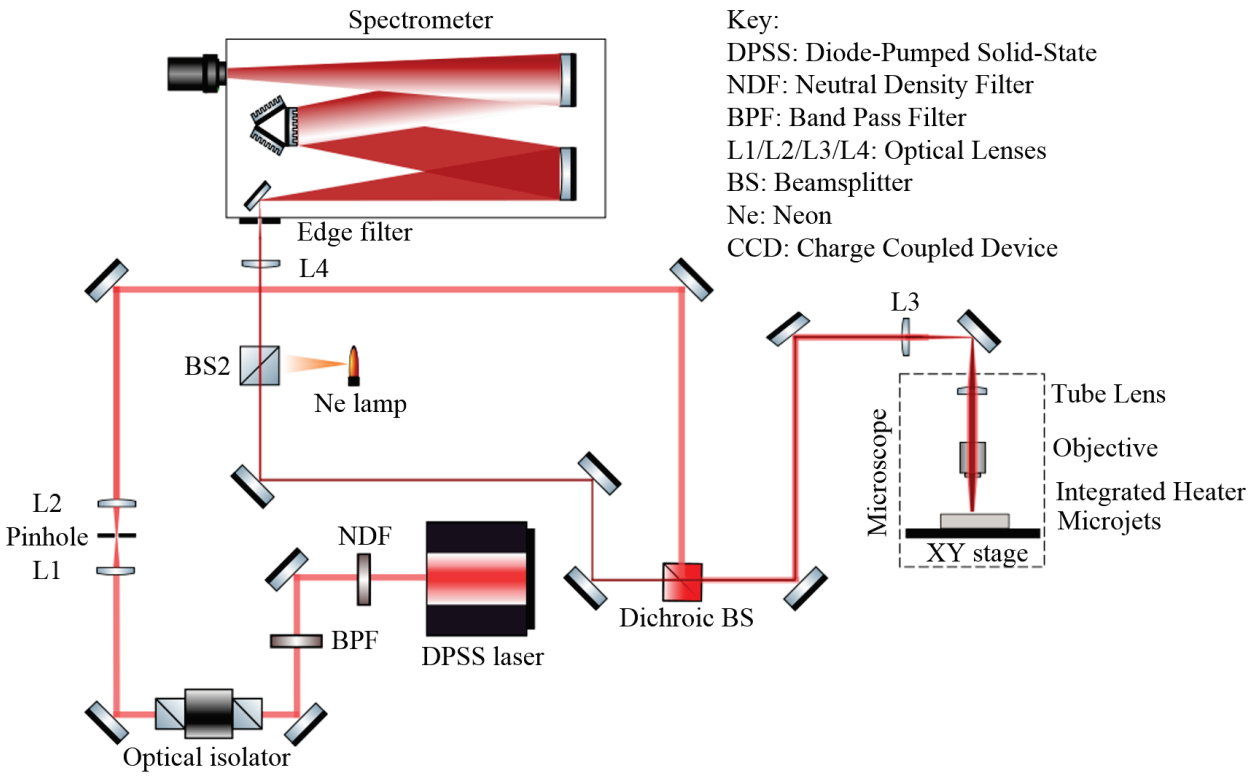

Figure 5.4: Raman optical path where the light source originates at the laser and the Raman scattered light is directed into the spectrometer entrance. The abbreviated terms are identified in the key.

The intent of the optical path is to fill the back pupil diameter (P.D.) of the objective with the laser beam. The P.D. is calculated according to

$$P.D. = 2 \cdot NA \cdot F \tag{33}$$

where NA is the microscope numerical aperture and F is the focal distance of the objective lens. For the 50x objective (LMPLFLN50XBD, Olympus), the pupil diameter was 3.6 mm. The beam diameter exiting the laser was 1.2 mm and was increased through the spatial filter to 3.0 mm with the lenses L1 and L2 shown in Figure 5.5a. Additionally, a 50 µm pinhole was used at the center of the spatial filter to achieve a clean Gaussian beam by eliminating noise at the fringes of the beam. The beam diameter was then increased to 3.6 mm with the L3 lens and the internal tube lens in the microscope to fill the back diameter of the objective as seen in Figure 5.5b. Lastly, the L4 lens decreased the beam diameter from 3.0 mm to approximately 50 µm to enter into the slit. A summary of the optical lenses used in the micro-Raman setup are shown below in Table 5.2. Achromatic convex doublets were used due to their higher optical performance over singlet lenses and improved off axis performance over aspheric lenses.

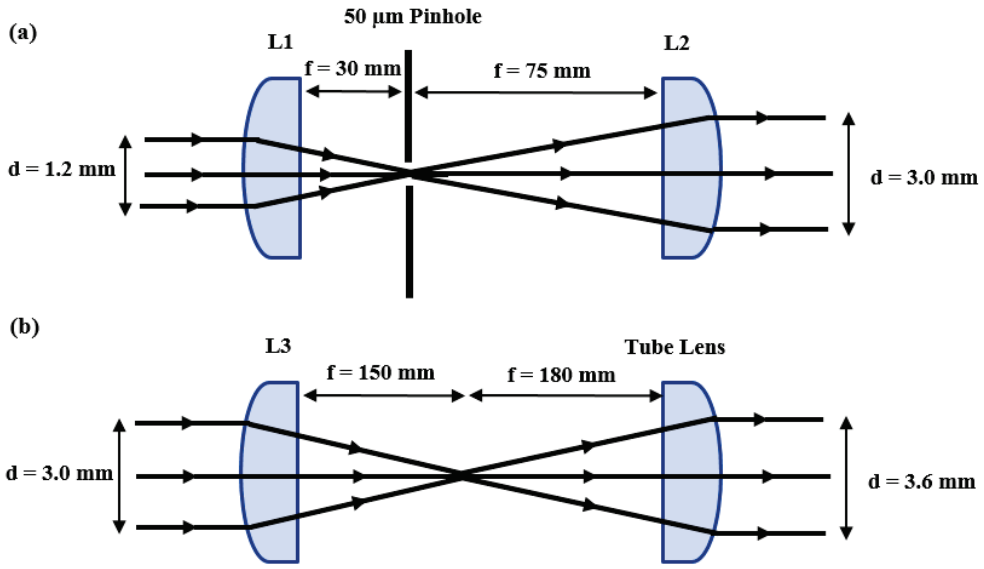

Figure 5.5: (a) Spatial filter used to produce a clean Gaussian beam and increase the beam diameter to 3.0 mm. (b) Lens combination to fill the 3.6 mm pupil diameter of the microscope objective.

Table 5.2: Optical lenses used in micro-Raman optical path.

Symbol	Lens Type	Focal Length	Manufacturer	Part Number
L1	Aspheric Convex Doublet	f = 30 mm	Thorlabs	AC254-030-A-ML
L2	Aspheric Convex Doublet	f = 75 mm	Thorlabs	AC254-075-A-ML
L3	Aspheric Convex Doublet	f = 150 mm	Thorlabs	AC254-150-A-ML
L4	Aspheric Convex Doublet	f = 50 mm	Thorlabs	AC127-050-A-ML

Additional optical equipment was used to control optical properties of the beam and to protect the laser. An O.D. 2 neutral density filter (NE20B, Thorlabs) reduced the optical power to approximately 0.5 mW to balance the signal intensity with laser heating of the sample. The band pass filter (LL01-633-12.5, Semrock) ensured that the wavelength of the laser was at 632.8 nm and eliminated optical noise. The optical, or Faraday, isolator (IO-3D-633-PBS, Thorlabs) allowed light to travel in only one direction with 88% transmission. This isolator prevented damage to the laser that can occur due to back reflections.

5.3.1. Spatial and Axial Resolution

In the micro-Raman thermography system used to take measurements in this work, the lateral spatial resolution depends on the laser spot size based on the $1/e^2$ width of the Gaussian beam profile shown below

$$d_{opt} = \frac{1.22\lambda}{NA} \tag{34}$$

where d_{opt} is the lateral spatial resolution, λ is the laser excitation wavelength and NA is the numerical aperture of the objective. The experimental measurements used a 633 nm red laser and a 0.55 NA microscope objective giving a lateral spatial resolution of ~1.4 μm. Improved spatial resolution can be achieved with a shorter wavelength laser excitation source or higher NA microscope objectives. Higher NA objectives of the same 50x magnification are available, however, working distance becomes a limiting factor for operation due to the use of electrical probes to apply power. Smaller working distances also introduce physical constrains on fixtures used to hold the sample.

The depth of field (DoF) of the measurement is calculated according to

$$DoF = \frac{4\lambda}{NA^2} \tag{35}$$

and thus also depends on the wavelength of the laser excitation source and the numerical aperture of the microscope objective. With the 633 nm laser and 0.55 NA objective, the depth of field of the measurement was approximately 8.37 μm. An important note with the axial resolution is that while the depth of field describes the optically viewable region, the depth of the actual measurement depends also on the absorption depth based on material properties. Kuball and Pomeroy [40] report that the axial spatial resolution for an above bandgap laser wavelength is described by

$$r_{axial} = \frac{1}{2\alpha} \tag{36}$$

where α is the absorption coefficient of the material. They provide the example of GaAs (bandgap = 1.42 eV, $\alpha = 1 \times 10^5$ cm^{-1}) being probed using a 488 nm (2.54 eV) excitation source, resulting in an axial spatial resolution of 50 nm. As a result, the measurement is mostly surface sensitive when the laser excitation is above the bandgap of the material. The experimental setup probed silicon (1.1 eV) with a 633 nm excitation (bandgap = 1.1 eV, $\alpha = 1 \times 10^4$ cm^{-1}) resulting in an axial resolution of 0.5 μm.

An important observation from the calculation of the spatial resolution of the measurement is the dependence on excitation wavelength. In the micro-Raman measurements, the laser excitation source is often in the visible range (λ=400-700 nm) whereas in infrared thermography measurements, the wavelength is in the medium wavelength infrared (MWIR) range (λ=3-8 μm) resulting in lateral spatial resolutions an order of magnitude larger. Although there is still spatial averaging occurring in the micro-Raman thermography measurements, the ~1 μm spot size reduces the averaging effect and shows a value closer to the actual peak temperature in the device.

5.4. Calibration

The Raman peak position coefficient (A) and the linewidth coefficients (B and C) from Equations 27 and 31, respectively, were experimentally obtained using the optical setup shown in Figure 5.4. A temperature controlled stage (Mk1000, Instec) allowed for precision control of the temperature from room temperature (~20 °C) to 140 °C in increments of 10 °C. The peak position and linewidth were measured and recorded at each temperature. The measurements were completed with a 1s exposure time, meaning the shutter on the CCD was open to light for this interval. The measurement was taken three times, averaged, and then repeated 5 times.

5.4.1. Raman Peak Shift

The Raman peak position (ω) is plotted versus the difference above room temperature ($T-T_o$) in Figure 5.6. The peak position followed the expected linear trend as temperature was increased from room temperature to 120 °C above room temperature. The Raman peak position was approximately 521 cm^{-1} at room temperature and shifted to 518.2 cm^{-1} at 140 °C. An experimental fit of the data gave a fitting coefficient of A = -0.0235 cm^{-1}/K, which compares well with other experimental results including Abel et al. who reported -0.0232 cm^{-1}/K for silicon [79] and Beechem et al. who reported -0.022 cm^{-1}/K for silicon [42]. Error bars resulting from the standard deviation of the measurement are smaller than the symbols in the plot.

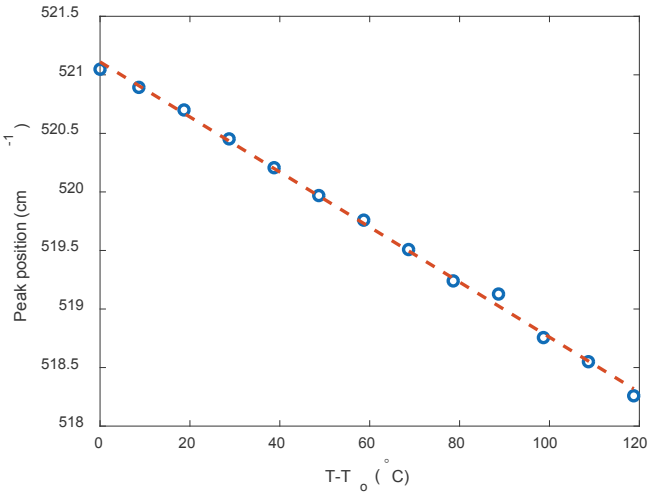

Figure 5.6: Calibration of the Si Stokes peak at temperatures ranging from 20 °C to 140 °C.

5.4.2. Raman Linewidth

The linewidth (Γ) was also collected at each of the successive temperatures and is plotted in Figure 5.7. The linewidth was initially at 2.99 cm^{-1} and widened to 4.03 cm^{-1} at 120 °C above room temperature. The linewidth followed the second order polynomial shape predicted by Equation 31. A fit of the equation

resulted in coefficients of B = 8.51×10^{-6} cm^{-1}/K^2 and C = 9.18×10^{-3} cm^{-1}/K, which agree in order of magnitude with the results of Beechem et al. who reported B = 6.70×10^{-6} cm^{-1}/K^2 and C = 4.14×10^{-3} cm^{-1}/K for silicon [42]. Beechem et al. notes that the linewidth is dependent on both crystalline quality and spectrometer slit width, and thus the fitting coefficients may vary from sample to sample and experimental setup to experimental setup.

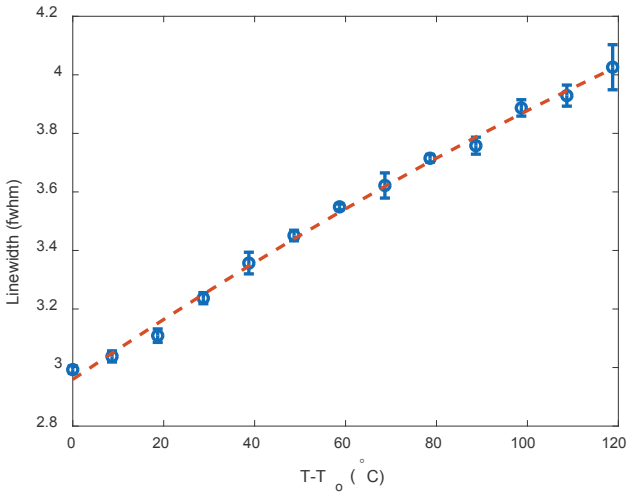

Figure 5.7: Calibration of the Si linewidth at temperatures ranging from 20 °C to 140 °C.

Contained in Table 5.3 are the fitting parameters for both the Raman peak position and the linewidth according to Equations 27 and 31. The uncertainty of each parameter was calculated using the error estimation structure in MATLAB, based on the quality of the fit. An observation is that the relative uncertainties of the two linewidth coefficients are higher than the uncertainty of the peak position coefficient. As will be discussed in the next section, the uncertainty of the temperature measurement using linewidth is higher than the uncertainty of the temperature measurement using the peak position shift method.

Table 5.3: Coefficients of temperature dependence for Raman features.

Coefficient	Value	Uncertainty	Units
A	-0.0235	3.33×10^{-4}	cm^{-1}/K
B	8.51×10^{-6}	1.95×10^{-5}	cm^{-1}/K^2
C	9.18×10^{-3}	1.38×10^{-3}	cm^{-1}/K

5.5. Data Reduction

At the start of every measurement period and throughout the measurements a reference peak position, ω_o, and linewidth, Γ_o were measured in an unpowered state. The reference peak position ranged from

520.81 to 520.98 cm^{-1} and the reference linewidths ranged from 2.807 to 2.858 cm^{-1}. During the experimental measurements, the device experienced a temperature rise of the device due to the joule heat generation from the DC electric power applied to the heater. The surface temperature was then calculated with both the Raman peak shift and linewidth broadening methods previously discussed:

$$T_{rise} = \left(\frac{\omega - \omega_o}{A}\right) \tag{37}$$

$$T_{rise} = \frac{-C + \sqrt{C^2 - 4B(\Gamma - \Gamma_o)}}{2B} \tag{38}$$

The temperature rise from the peak position is calculated from the experimentally obtained coefficient, *A*, in Table 5.3 and the change in peak position. The temperature rise from the linewidth in Equation 38 is from solving the quadratic equation in Equation 31 and the experimentally obtained coefficients *B* and *C*.

5.6. Uncertainty Analysis

The calculation of the uncertainty of the Raman temperature measurement is shown below following Kline and McClintock's vector summing technique [66]

$$dT_\omega = \sqrt{\left(\frac{\partial T}{\partial A}\delta_A\right)^2 + \left(\frac{\partial T}{\partial \omega}\delta_\omega\right)^2 + \left(\frac{\partial T}{\partial \omega_o}\delta_{\omega_o}\right)^2} \tag{39}$$

$$dT_\Gamma = \sqrt{\left(\frac{\partial T}{\partial C}\delta_C\right)^2 + \left(\frac{\partial T}{\partial B}\delta_B\right)^2 + \left(\frac{\partial T}{\partial \Gamma}\delta_\Gamma\right)^2 + \left(\frac{\partial T}{\partial \Gamma_o}\delta_{\Gamma_o}\right)^2} \tag{40}$$

Within this method, the derivative of temperature with respect to each constituent term was multiplied by the uncertainty of the term. The uncertainty of the temperature rise calculated from the change in peak position in Equation 39 was calculated by taking the sum of the squares of the partial derivatives for each parameter in Equation 37. The uncertainty due to the A coefficient (δ_A) was from the fitting of the calibration. The uncertainties of the peak positions (δ_ω) and (δ_{ω_o}) were calculated based on the standard deviation of the multiple Raman measurements taken. The uncertainty of the temperature rise calculated from the change in linewidth was calculated using the same process. The uncertainty due to the fitting coefficients (δ_C) and (δ_B) were from the fit of the calibration line shown in Figures 5.6 and 5.7. The uncertainties due to the linewidth measurements (δ_Γ) and (δ_{Γ_o}) were calculated from the standard deviation of the multiple Raman measurements at each point.

The uncertainty for both the peak position and linewidth methods depend on the temperature difference. As a result, the uncertainty increased at higher temperatures. At an elevated temperature of 45 °C, the

uncertainty of the temperature rise from the peak change was approximately ± 2 °C and the uncertainty of the temperature rise from the linewidth change was ± 10 °C. Although the peak position method offers lower uncertainty than the linewidth method, the peak position includes the effects of stress, whereas the linewidth method is stress free. In order to use strictly the peak position method, one must determine whether stress affects the sample at the applied power level through using a stress free method, such as the linewidth method. In this thesis, both the peak position and linewidth methods were used to calculate the temperature rise in the device.

5.7. Chapter Summary

In Chapter 5, the principles of micro-Raman thermography were reviewed and the experimental setup and calibration of the silicon samples in this thesis were presented. The physical interactions leading to Raman scattering (including Stokes and anti-Stokes scattering) were used to provide background for the temperature dependent features of the Raman spectrum as analyzed by a CCD. In particular, the peak position and linewidth features, and the physical basis for their trends, were demonstrated for the silicon sample in this thesis. Next, methods to address the stress contribution to the peak position were reviewed for materials with both multi-peak and single peak Raman responses. The experimental setup used for the micro-Raman measurements in this thesis was discussed including the optical components used to control the beam size and block out Rayleigh scattered light. The peak position and linewidth of the sample were measured for the sample on a heating stage at temperatures from 20 °C to 140 °C. Lastly, the uncertainty of both the peak position (± 2 °C) and linewidth (± 10 °C) methods for calculating temperature rise were presented. Although the peak position method offers lower uncertainty than the linewidth method, one must use a stress free measurement method (such as the linewidth method used in this thesis) in order to understand the contribution of stress to the measurement.

6. Results

The performance of the microjet cooling system was characterized both thermally and fluidically. The micro-Raman technique was used to scan the surface temperature profile with 1 µm spatial resolution and a 5 µm step size with 1.95 W of DC power applied and microjet cooling on the backside. This technique was performed at several different power levels, showing strong agreement with the numerical model. Next, the model was used to explore the heat transfer dependence on velocity. This velocity dependence was balanced with the tradeoff of increased driving pressures obtained experimentally and ideal pumping power. Lastly, the results of an extended 1000-hour test are presented to address common concerns of clogging and erosion.

6.1. Raman 2D Temperature Scanning

In addition to the validation with the Nusselt correlation of Michna et al. shown in Chapter 3, the micro-Raman setup enables additional experimental data for validation of the CFD model. The experimental setup included the integrated heater with the circular microjet array mounted in the test fixture and attached to the movable XY stage. The experimental conditions were an overall flow rate of 0.184 L/min, equating to flow rate per jet of 9.7 mL/min, a jet velocity of 16 m/s, and a Re of 1900. A voltage difference of 90 V was applied across the device with the source/measure unit and probe manipulators. A current of 21.7 mA was measured, resulting in a Joule heating rate of 1.95 W.

The boundary conditions of the numerical model were adjusted to match the experimental heat generation. To match the heat generation profile, a heat rate of 0.488 W for the quarter symmetry model (1.95 W total) was applied to the "fingers" of the integrated heater. The fluid boundary conditions were set with an inlet jet velocity of 16 m/s and a zero pressure condition on the exit ports. The simulation results were post processed to show the surface temperature profile, which could then be compared with the micro-Raman thermography surface profile measurement.

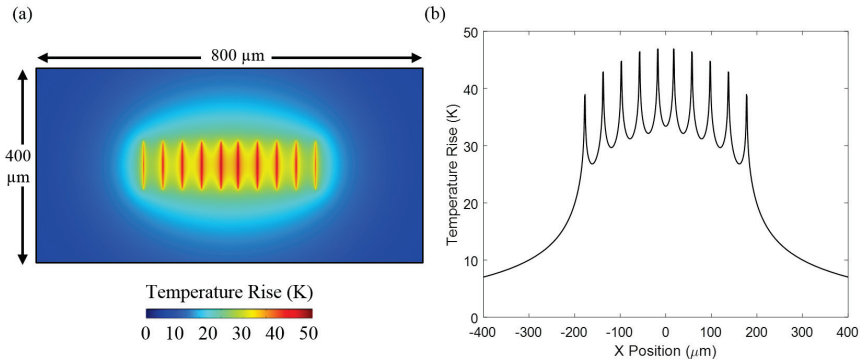

Figure 6.1: (a) Surface temperature profile of the integrated heater with 1.95 W heat rate applied and jet velocity of 16 m/s. (b) Temperature rise of a horizontal slice through the midsection of the integrated heater.

In Figure 6.1a, the surface temperature rise over the fluid temperature is shown with color contours, showing the highest temperature rise of approximately 46 K at the two central fingers. A horizontal slice through the midsection of the integrated heater shows the temperature gradients in proximity to the fingers in Figure 6.1b. The peaks in temperature at the fingers are highest in the center and decrease towards the periphery. This is most likely due to the effect of thermal crosstalk and reduced spreading effects of the closely spaced fingers.

One can extract the heat transfer coefficient from the numerical model as shown in Figure 6.2. The microjets produced extremely high local heat transfer coefficients, approximately 380,000 W/m^2-K located at the centerline of the central microjet cluster. The average heat transfer coefficient across the entire 1 mm × 1 mm square was 260,000 W/m^2-K. Although excellent heat transfer was experienced with the central cluster of microjets, the outer ring of microjets exhibits some effects of crossflow – that is, the effluent from the central microjets deflected the outer microjets radially outward. Improved array geometries could minimize this effect, and produce even higher average heat transfer coefficients.

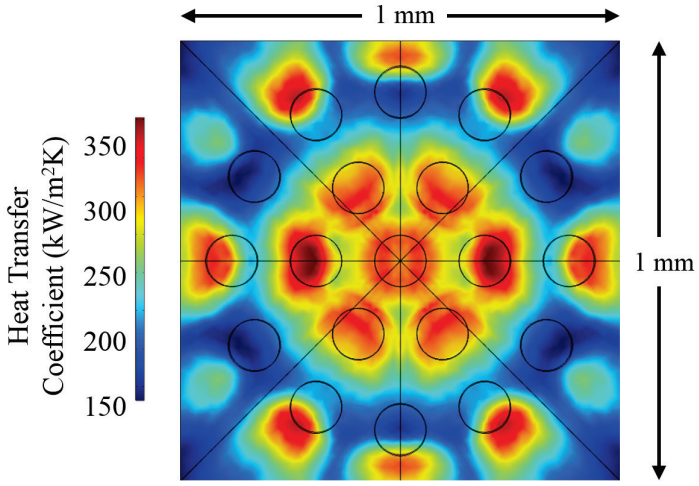

Figure 6.2: Heat transfer coefficient map for the circular array at the conditions of 1.95 W (total) and jet velocity of 16 m/s. Fluid is water.

To support these numerical results, micro-Raman thermography was used to obtain the corresponding surface temperature measurement of the integrated heater. A schematic of the test device heater is shown in Figure 6.3a. Being the center-most heater strip (or, "finger"), the sixth vertical strip in the sequence was expected to be the warmest. Figure 6.3a also indicates the position of the detailed horizontal slice through the center of the device and vertical slice adjacent to the sixth finger.

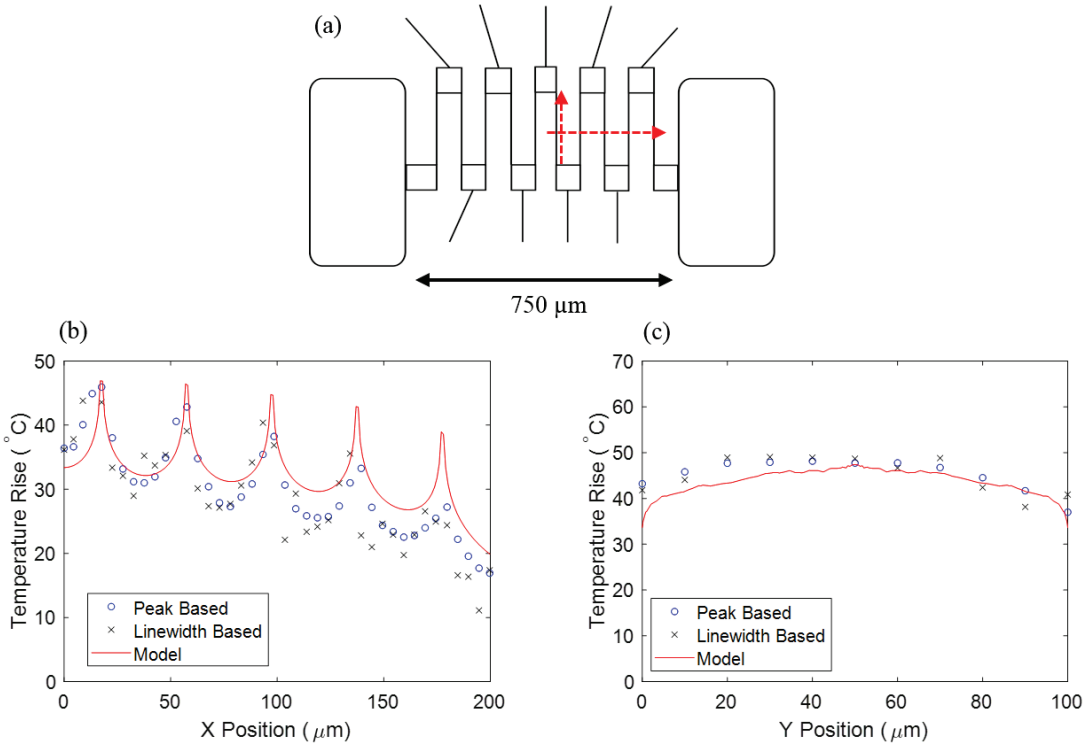

Figure 6.3: (a) Device schematic showing the location of the horizontal and vertical slices. (b) Horizontal slice through the device showing local maxima at the finger locations. (c) Vertical slice along the central finger of the device.

For the horizontal temperature slice shown in Figure 6.3b, micro-Raman measurements were made at the vertical center of the device, located 50 µm through the 100 µm finger length. The temperature rise was calculated using both the peak shift (blue circles) and linewidth broadening methods (black x's) discussed in Chapter 5. A surface temperature profile was taken using 5 µm increments from the middle of the device to the periphery. Consistent with expectations, the measured temperatures exhibit a temperature rise when approaching the heater fingers (i.e., where the heat is being generated). Local minima are observed in between the heater fingers. Moreover, the global maximum, or peak, temperature is observed at the sixth (center-most) heater finger, with decreasing finger temperatures away from the center of the heater. Additionally, the measurements in the y-direction (Figure 6.3c) show that the temperature was highest at the center point of the sixth leg. For the 1.95 W dissipation rate (a heat flux > 5 kW/cm^2), the peak temperature rise was measured to be 45.9 ± 2 °C at this position.

Agreement with numerical predictions (solid red line in Figures 6.3b and 6.3c) is good, lending strong support to the predicted heat transfer coefficients. Losses, including heat conduction through the PEEK fixture and natural convection with free air at the heater surface (not accounted for in the model) may contribute to the model's over-prediction of the heater's surface temperature, particularly at the periphery closest to the contact with the fixture. Additionally, somewhat lower measurements may be expected in the experiment due to the area enhancement of the jet plate support pillars, which were not included in the

numerical study. Future refinements to the computational model will include these contributors for comparison with the experiment.

Also observed in Figures 6.3b and 6.3c is the consistency between the Raman peak position method and the linewidth method in calculating the temperature. The peak position method included the stress contribution, whereas the linewidth method was stress independent but with higher uncertainty. Agreement between the two methods suggests that stress was not a contributing factor to the peak shift in this device at this power level, and thus both methods can be used to calculate the temperature of the device in the powered state.

6.2. Temperature vs. Power

To further validate the accuracy of the numerical model, the temperature rise at the previously identified hottest location (adjacent to the sixth finger) was probed for increasing power levels. This location is highlighted with the red dot in Figure 6.4a. Experimentally, the applied voltage was varied from 10 V to 110 V, with the measured current ranging from 2.89 mA to 25.6 mA. The variation in voltage resulted in power ranging from 0.03 W to 2.81 W across the fingers of the heater. The flow rate was maintained at 0.184 lpm, or a jet velocity of 16 m/s, for this testing.

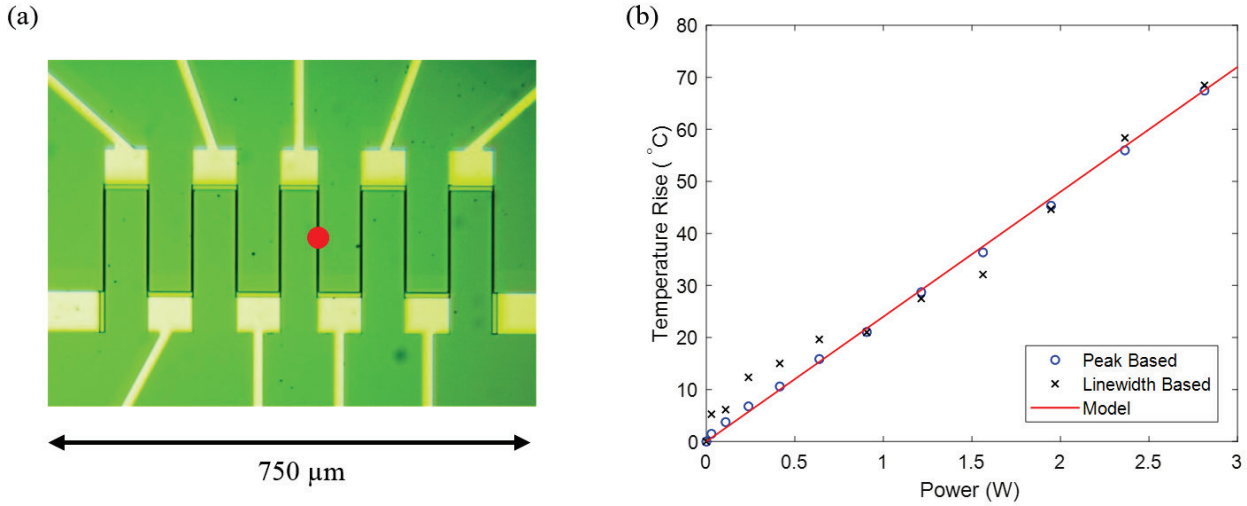

Figure 6.4: (a) Microscope 10x image of the device with red dot indicating the measurement location. (c) Peak temperature rise versus power level for the location depicted in (a).

As the power level was applied, the temperature was measured using both the Raman peak shift and linewidth broadening techniques. The temperature rose linearly with increasing power levels as observed in Figure 6.4b. The numerical model was used to predict the temperature rise for varying power levels (shown with the solid red line in Figure 6.4a) for the same fluid boundary conditions. A fit of the data showed that the temperature rose approximately 24 K per watt of power applied. The agreement of the

numerical model results and the experimental results (both the peak position and linewidth methods) builds additional confidence in the validity of the computational model.

6.3. Varying Heat Flux

The micro-Raman thermography setup was utilized to experimentally validate the surface temperature profile at varying heat fluxes. In this testing, the voltage difference across the DC probes was varied and the resulting current was measured. The voltages studied in this section were 40 V (I = 10.35 mA), 60 V (I = 15.17 mA), 80 V (I = 19.62 mA), and 100 V (I = 23.73 mA). The electric power was dissipated as heat and was used to calculate the four different power levels: 0.41, 0.91, 1.57, and 2.37 W, respectively. The numerical model simulated each of these four different heat rates and generated surface temperature profiles of the integrated heater. The fluid boundary conditions were identical to the 2D scan in Section 6.1 with a jet velocity of 16 m/s and zero pressure condition on the fluid exit. The temperature profiles show an increase in temperature experienced at the heater fingers as well as the areas surrounding the heater fingers.

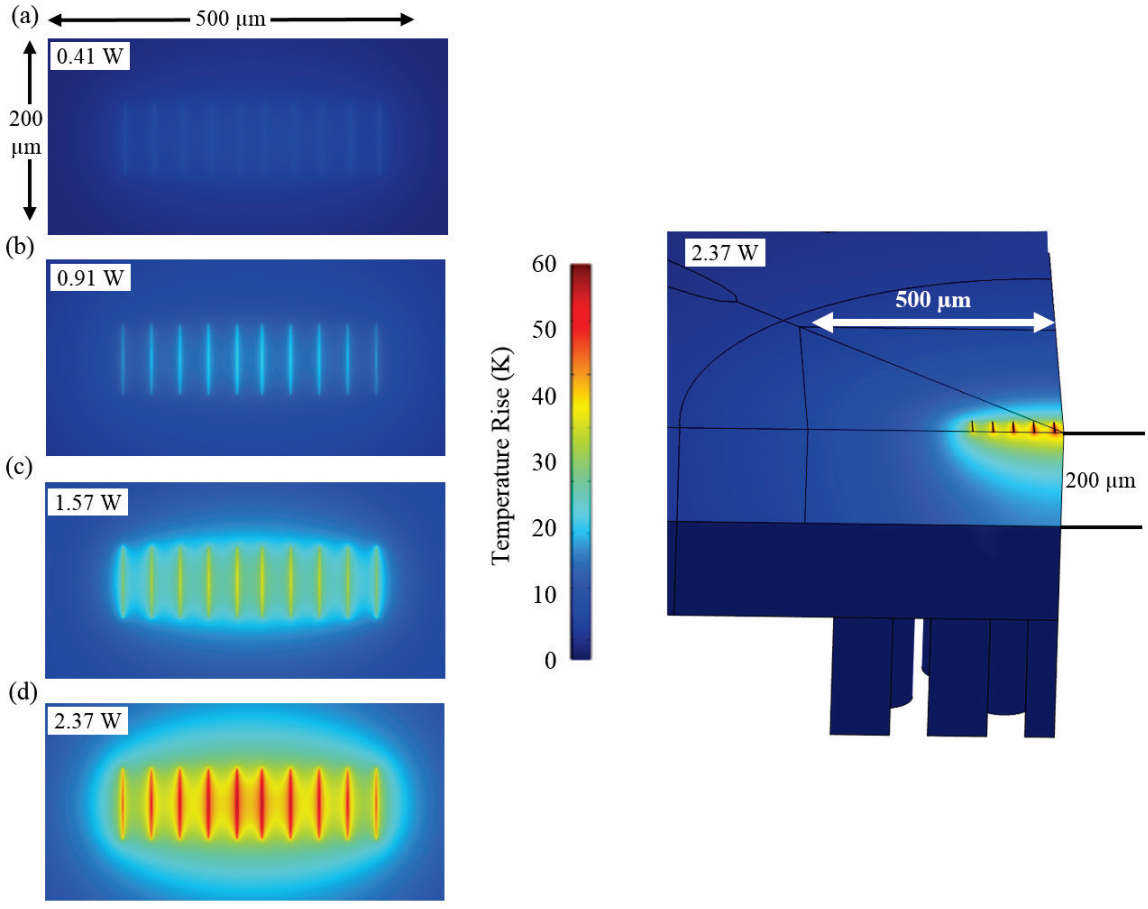

Figure 6.5: Surface temperature profile at varying heat rates from the numerical model for varying power levels of (a) 0.41 W (b) 0.91 W (c) 1.57 W (d) 2.37 W.

The micro-Raman measurements of the integrated heater were taken with 5 µm increments at each of the different heat fluxes. The first measurement was in the center of the device and the subsequent measurements were taken in an x direction horizontal scan through the first two fingers. The numerical simulations were processed through the rest of the fingers and are shown in Figure 6.6b. Agreement between the experimental and simulated temperatures builds additional confidence in the computational model.

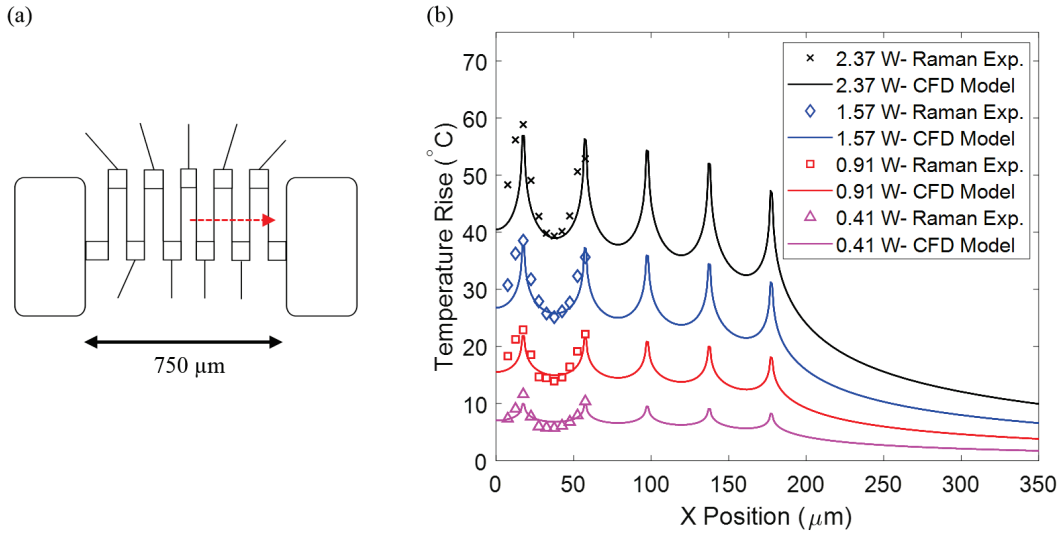

Figure 6.6: (a) Device schematic showing the location of the horizontal slice location. (b) Surface temperature profile at varying heat rates of 0.41 W, 0.91 W, 1.57 W, and 2.37 W for the slice shown in (a).

An important observation in the varying heat flux scans is the increase in both peak temperature and temperature gradients in between the fingers. At the maximum heat flux applied (2.37 W), the peak temperature of 56.9 °C at the sixth finger changes to 39.0 °C at the local minimum in between the sixth and seventh fingers. This temperature difference of 18 °C is experienced over a spatial distance of 20 µm. As discussed in Chapter 1, traditional temperature techniques such as IR thermography are limited to a spatial resolution of 3-8 µm. Using a technique such as IR thermography results in the inability to resolve these steep temperature gradients and will under-predict the true peak temperature.

To quantify the averaging effect that occurs in the two experimental measurement techniques, an average temperature was predicted from the simulation for a 1 µm spot size for the Raman measurement and a 5 µm pixel size for the IR measurement. The average temperature for a measurement around the sixth finger (from the numerical simulation temperature profile) was then calculated according to

$$T_{Raman,pred} = \frac{\int_{-0.5}^{0.5} T(x)dx}{1} \tag{41}$$

$$T_{IR,pred} = \frac{\int_{-2.5}^{2.5} T(x)\,dx}{5} \tag{42}$$

where T(x) is the local temperature around the central finger and the integral is evaluated before and after the sixth finger. The effects of spatial averaging are shown in Table 6.1.

Table 6.1: Effect of spatial averaging on temperature measurement. Temperatures are in K.

Power Level (W)	$T_{CFD, Max}$	$T_{Raman, Exp}$	$T_{Raman, Pred}$ ($T - T_{CFD, Max}$)	$T_{IR, Pred}$ ($T - T_{CFD, Max}$)
0.41	9.94	11.6 ± 2	9.80 (-0.14)	9.16 (0.78)
0.91	21.8	22.9 ± 2	21.5 (-0.30)	20.1 (-1.70)
1.57	37.7	38.5 ± 2	37.2 (-0.50)	34.7 (-3.0)
2.37	56.9	58.9 ± 2	56.2 (-0.70)	52.5 (-4.4)
8.34 (CFD Only)	*199.7*	*N/A*	*198.2 (-1.50)*	*184.3 (-15.4)*

The influence of spatial averaging on the temperature measurement, as explored in this study, highlights the importance of using a high spatial resolution thermometry technique. At the power levels achieved with the current experimental setup, an IR measurement would under predict the true peak temperature rise of 56.9 K by 4.4 K at an input power of 2.37 W. At a simulated higher power level of 8.34 W, the IR measurement would under predict the true peak temperature rise by 15.4 K, whereas the Raman measurement would under predict by just 1.5 K due to averaging. Of note, these results are for the HEMT geometry in this thesis, future HEMTs, with higher power-densities, are expected to generate even steeper temperature gradients. This study only included the effect of averaging perpendicularly to the HEMT fingers and did not account for averaging that occurs in the parallel direction to the gate finger. As shown in Figure 6.3, the temperature gradients are much steeper in the perpendicular direction than the parallel direction.

6.4. Flow rate scalability

To understand the effect of flow rate on heat transfer performance, the inlet flow velocity in the numerical model was varied from 0.5 to 35 m/s. The results were post-processed to calculate and plot the heat transfer coefficient at 5, 10, 15, 20, and 25 m/s in Figure 6.7.

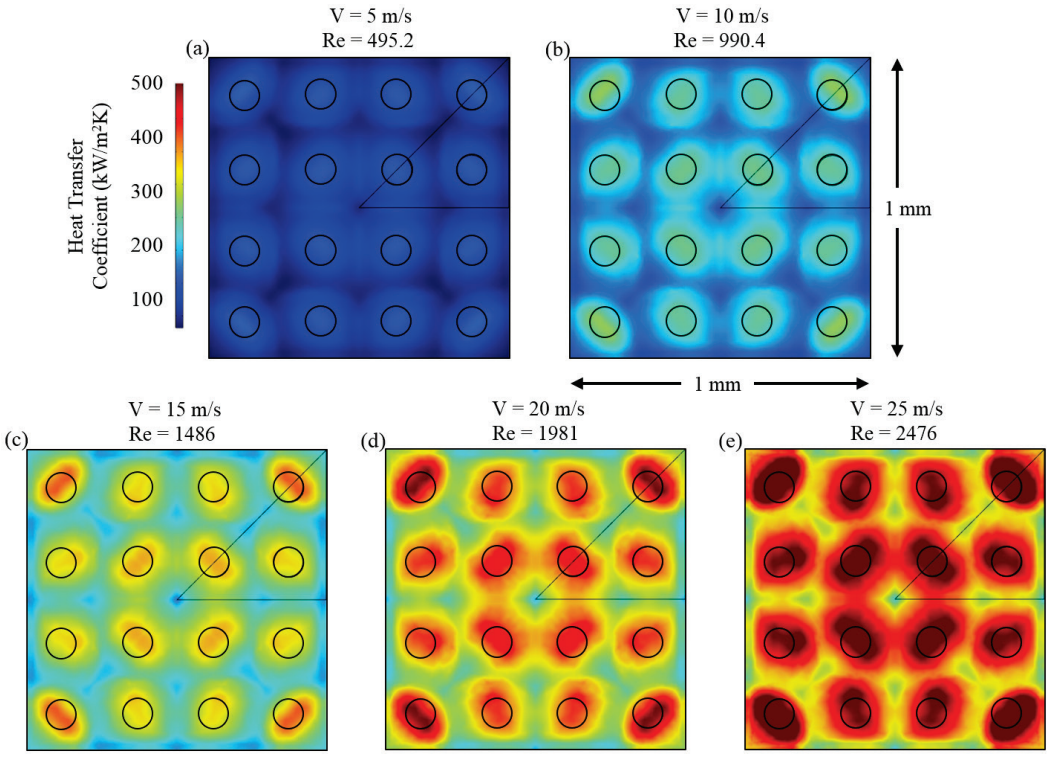

Figure 6.7: Heat transfer coefficient maps (with a fixed scale) for the 1 mm x 1 mm impingement zone at (a) 5 m/s, (b) 10 m/s, (c) 15 m/s, (d) 20 m/s, and (e) 25 m/s. Locations of the jet orifices are shown in black circles. Fluid is water.

The black circular outlines in Figure 6.7 show the location of the jet orifices for the square array. The highest heat transfer coefficients are observed directly underneath the jet centerline. As expected, the heat transfer coefficient increases at the higher jet velocities. This increase in heat transfer applies to both the peak heat transfer coefficient and the average for the entire impingement zone. The average heat transfer coefficients were plotted against jet velocity below in Figure 6.8.

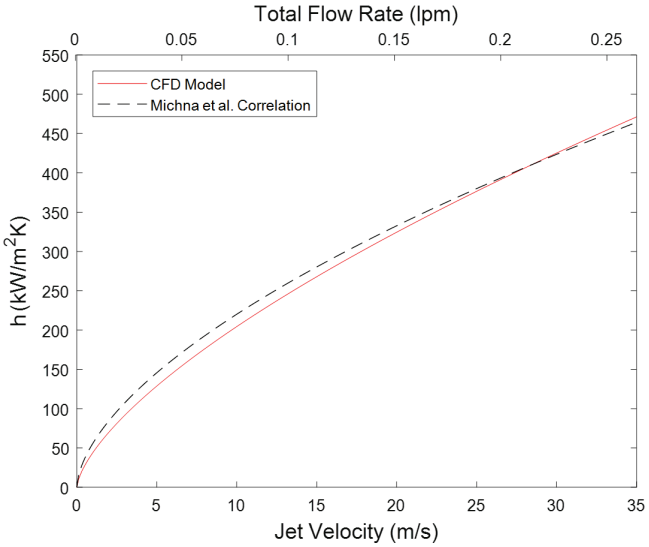

Figure 6.8: Average heat transfer coefficient plotted versus the jet velocity on the lower x-axis and total flow rate on the upper x-axis.

Area averaged heat transfer coefficients, extracted from the numerical model, are shown in the dashed line in Figure 6.8 from 0.5 to 35 m/s. The heat transfer coefficients is shown to scale with $V^{0.67}$. Also shown in the plot is the comparison with the empirical correlation of Michna et al., which is used to calculate the heat transfer coefficient according to

$$h = \frac{D}{k} 0.675 Re_D^{0.55} Pr^{0.243} \cos(5.416 A_r - 1.259) \tag{43}$$

An important note with the calculation of the heat transfer coefficient based on this correlation is that the Reynolds number is based on fluid inlet properties, whereas the Prandtl number is evaluated at film temperatures.

As demonstrated with experimental results in Chapter 4, the pressure drop across the microjet device scales with V^2. At the upper end of the jet velocities shown in Figure 6.9, the system reaches high pressure drops of 900 kPa. The heat transfer coefficient from the numerical model was plotted against the pressure drop in Figure 6.9a. The heat transfer coefficient was plotted against the ideal pumping power, calculated from the pressure drop and system flow rate, in Figure 6.9b.

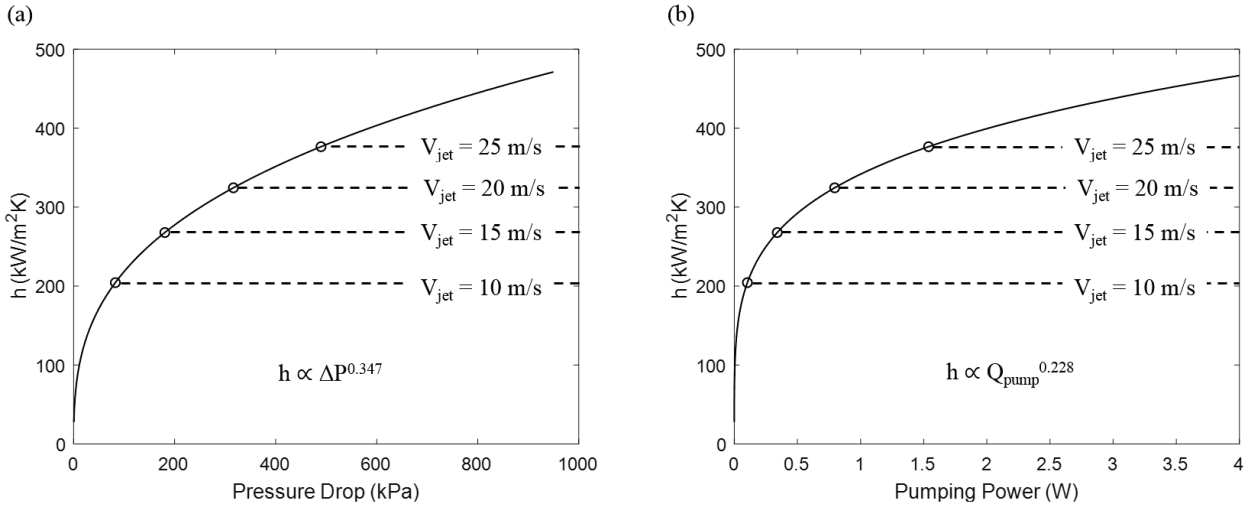

Figure 6.9: Heat transfer coefficient plotted against (a) pressure drop across the microjets (b) ideal pumping power.

The pumping power shown in Figure 6.9b indicates that high heat transfer performance can be achieved even at low pumping powers (0.1 W), with an average heat transfer coefficient of 2.05 x 10^5 W/m^{2}K with a jet velocity of 10 m/s and a modest overall flow rate of 0.076 lpm. The pumping power relationship illustrates that although doubling the jet velocity from 10 to 20 m/s improves the heat transfer by 1.6x, the required pumping power increases 8x. Both plots in Figure 6.9 demonstrate the tradeoff between the improved heat transfer performance achieved at higher jet velocities, with the cost of increased system pressures and pumping powers. These higher (but still modest) pressure drops require more powerful pumps capable of supplying fluid at higher pressures and flow rates, and require additional electrical power

to operate. The increased demand for pumping power reduces the coefficient of performance (COP) of the system, which is a ratio of the useful heat removed by the system to the work required by the system. At the lower end of the flow rate limit, low flow rates may exceed the thermal capacity of the fluid and rise in temperature before exiting the fluid cavity. At extremely low flow rates, the fluid can potentially boil depending on the temperature of the impingement surface.

A second metric of thermal performance used in thermal management literature is the thermal resistance from the junction to inlet fluid temperature. This metric is used by Brunscwhiler et al. to evaluate the performance of a microjet cooling manifold [54] and an ultrathin microchannel manifold [80]. This term is used to estimate the temperature rise for a given heat flux, and the units are K-cm^2/W. The calculation of the thermal resistance from junction to inlet is shown below

$$R_{th\,total} = R_{convective} + R_{conductive} = \frac{1}{h} + \frac{t}{k_{si}} \tag{44}$$

where the total thermal resistance has a convective contribution and conduction contribution that are summed. The convective thermal resistance is the inverse of the heat transfer coefficient. The conductive contribution is a measure of the resistance through a substrate of thermal conductivity (k) and a thickness (t). For this experiment, the thickness of the silicon substrate was 200 µm and the thermal conductivity of silicon (k_{Si}) was 150 W/m-K, resulting in a conductive thermal resistance of 0.013 K-cm^2/W. The total thermal resistance and its two contributions are shown in Figure 6.10. Also shown on the plot are the results of Brunschwiler et al. [54]. Of note, the substrate used in the Brunschwiler et al. experiment was thicker (720 µm compared to 200 µm in this thesis), resulting in a conductive thermal resistance of 0.055 K-cm^2/W.

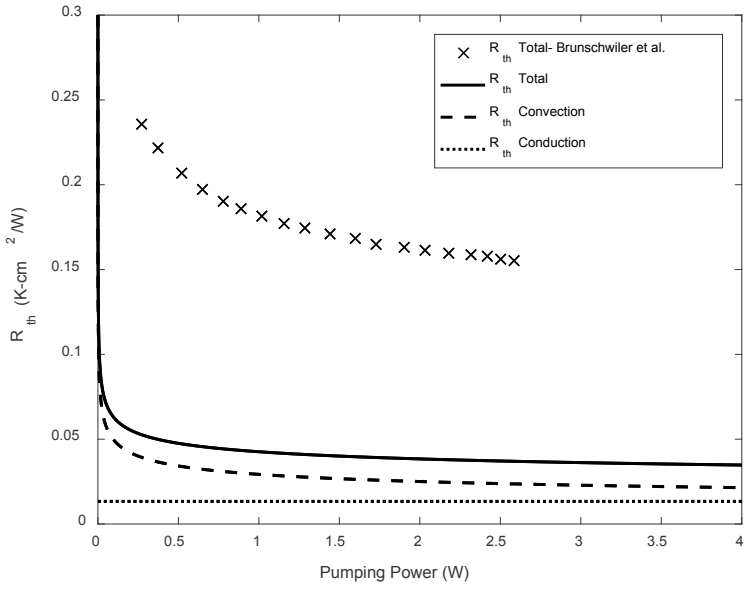

Figure 6.10: Total thermal resistance from junction to fluid inlet and its two contributions of conduction through the silicon substrate and convection with the liquid, per the Brunschwiler et al. model [54].

The thermal resistance analysis shows an asymptotic trend at the higher pumping power levels, where the total thermal resistance approached 0.035 K-cm^2/W. The total thermal resistance is fundamentally limited by the conduction resistance through the heater substrate. This conduction resistance can be decreased by decreasing the thickness of the substrate or changing to a higher thermal conductivity substrate. The thickness of the substrate is governed by structural requirements. The substrate thermal properties can be improved by switching to materials such as silicon carbide (4H SiC, k = 380 W/m-K) or diamond (k = 2000 W/m-K) [81]. Assuming the same substrate thickness of 200 μm, the thermal resistance would decrease from 0.013 K-cm^2/W for Si to 0.005 K-cm^2/W for SiC and 0.001 K-cm^2/W for diamond. Although these materials have improved thermal conductivities, difficulties in implementation can arise due to mismatch of coefficients of thermal expansion when attached to different materials. Additionally, the fabrication processes for these materials are relatively immature compared to silicon fabrication processes.

While the thermal resistance model is a useful approach to understand the relative contributions of the conductive and convective thermal resistances, it provides a limited framework for assessing temperature rises in devices. One of the limitations is that although the embedded cooling approach removes several layers of thermal resistance, there are additional thermal interfaces (including the interfacial resistance of the GaN to its substrate) that are not included in this model. One of the other limitations of the thermal resistance model is that it fails to account for near junction spreading resistance. This spreading resistance can contribute significantly to temperature rises in devices. In order to truly evaluate the effectiveness of a cooling technology, a complement of numerical and experimental analysis (as in this thesis) must be performed.

6.5. Extended Lifetime Testing

As demonstrated, microjets offer extremely high heat transfer performance, even at lower pumping powers. They achieve such high levels of performance due to momentum and energy exchanges that occur when the high velocity jet interacts with the wall. The performance dependence on velocity raises two practical concerns when considering implementing microjets: clogging and erosion.

A frequently cited concern with implementing jet impingement for electronics cooling is the susceptibility to clogging. Clogging occurs when particles are introduced to the flow loop (from outside, or generated within the loop) impeding flow through one of the 100-116 μm diameter jets. A consequence of clogging would be a sudden increase in the required driving pressure of the system, due to the corresponding decrease in microjet cross sectional area. Alternatively, with a fixed driving pressure, the flow rate through the microjets would decrease. More importantly, in both cases, clogging can adversely

affect the array's ability to provide uniform cooling. Here, we provide experimental evidence of extended, clog-free operation of microjets using only commercially available, low-cost filters.

The concern for erosion exists because of the momentum exchange that occurs at the impact of high velocity streams of water with the wall when used continually. The erosion concern was investigated in a numerical study performed by Ditri et al., who implemented a similar jet impingement based system using jet diameters of 60 μm [38]. Ditri et al. used Lagrangian Particle Tracking for particle sizes ranging from 0.5 to 5.4 μm to track the impact of jet impingement on the back of the gold ground plating. The density of the particles was set to match steel (7800 kg/m^3) and they determined that erosion was insignificant for particles less than 2 μm mean diameter. Their study also coupled a stress analysis to show that the impact stress was well below that allowed for the device. In this thesis, two extended tests were performed allowing for maximum particle sizes of 2 μm and 10 μm.

To experimentally investigate the viability of microjet impingement as a long-term electronics cooling solution, a 1000-hour test was performed. This test was meant to simulate operating conditions for an extended period, with the 1000-hour threshold chosen as a common level for demonstrating lifetime workmanship. In this test, the microjet device was secured in the fixture and the recirculating chiller was operated for 1000 cumulative hours. The flow rate and pressure drop across the orifice were monitored throughout the experiment and are plotted in Figure 6.11.

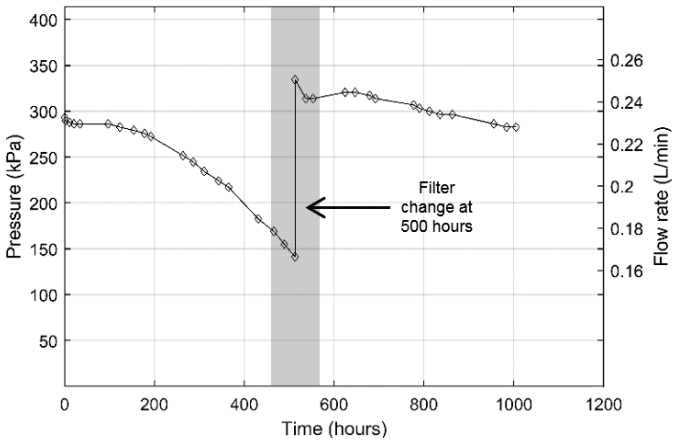

Figure 6.11: Pressure drop and flow rate recorded during the 1000-hour of continuous microjet impingement.

The reason for the sudden change that occurs approximately 500 hours into the test is that the 2 μm filter was changed at the halfway point. The decrease in pressure drop and flow rate that occurs in the first half of the test is due to this inline filter, rather than the microjets, collecting particles greater than 2 μm. When the filter was replaced, the pressure drop and flow rate were fully restored to higher than their initial values. The reason that the pressure drop and flow rate were restored to higher values is that the filters had

been in operation before the start of the test (for example, during the pressure flow rate characterization in Chapter 4) and were likely partially clogged before the test. The 2 μm filter (SS-6TF-2, Swagelok) was relatively inexpensive, ~$10, and can be replaced easily. The filter could also be replaced with a large particle size filter of 5-10 μm pore size to decrease replacement frequency with minimal effect on clogging. The microjet orifices were examined visually before and after the 1000-hour test shown in Figure 6.12.

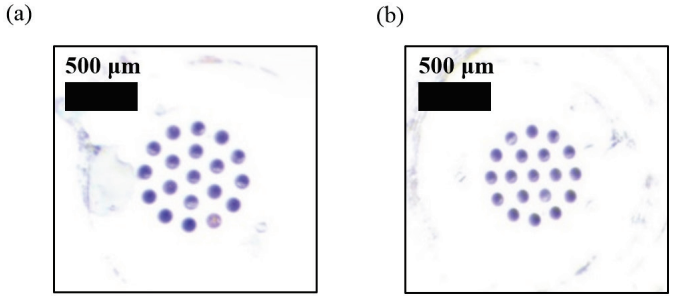

Figure 6.12: (a) The microjet array before the 1000-hour test. (b) The microjet array after the 1000-hour test with no indications of clogging.

The 19 microjet orifices were visually inspected for debris or indications of clogging, and they were clear both before and after the extended testing. The visual inspections and the monitoring of the pressure drop and flow rate throughout the 1000-hour testing suggested that the microjets themselves did not clog. The takeaway from this portion of the study was that proper filter selection can effectively mitigate the risk of clogging in microjet systems. Such filters can be compact in size, inexpensive, and easily replaceable. This study suggests proper clogging mitigation with filters of pore size less than D/10.

Continual impacts of contaminant particles can erode the wall and cause anomalous device behavior, or, in severe cases, eventual leakage of fluid out of the device. Throughout the 1000-hour test, the area immediately around the microjet assembly was monitored for signs of leaking. The area remained dry the entire 6 weeks, indicating that no catastrophic failures occurred such as the device rupturing. To examine whether there were more subtle indications of erosion, at the conclusion of the test, the microjet array and integrated heater were diced through their centerline as shown in the scanning electron microscope (SEM) image in Figure 6.13.

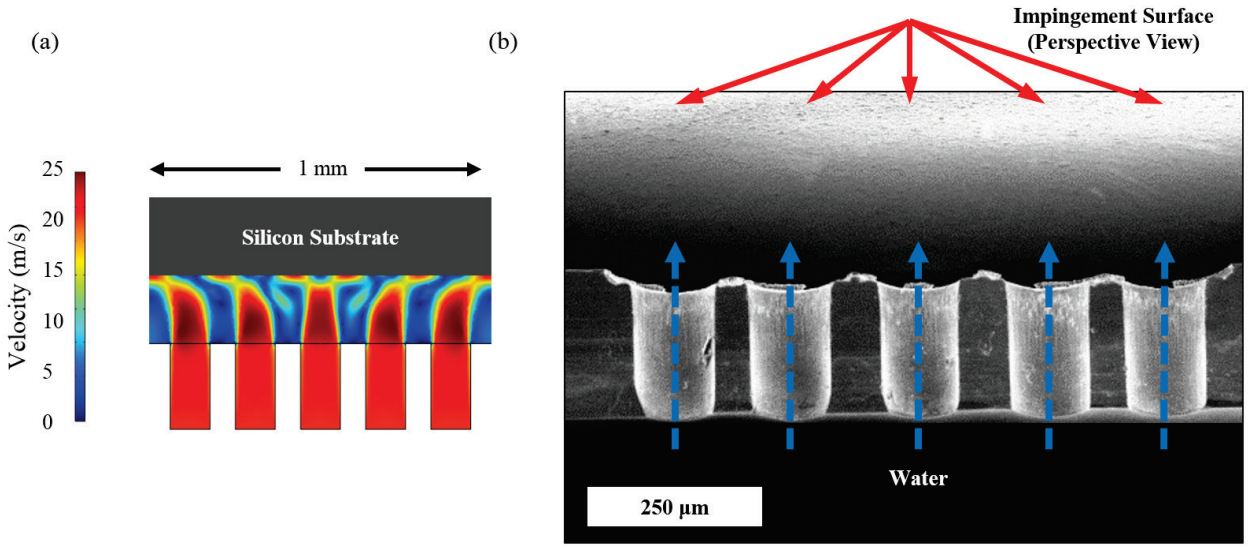

Figure 6.13: (a) Velocity profile for an inlet velocity of 20 m/s within the microjet cavity from the computational model. (b) Scanning electron microscope (SEM) image showing a perspective view of the impingement regions after 1000 hours of runtime.

The velocity profile from the CFD model in Figure 6.13a shows the areas of concern for erosion, which are directly opposite the microjet orifices. Any particles contained in the fluid would experience their greatest impact with the wall at these locations, which are identified in the SEM image in Figure 6.13b. If there were erosion, due to particle blasting, then it would occur in a pattern similar to the microjet array. The SEM image shows a uniform surface profile at the backside of the heater, without any indentations on the impingement surface. This shows that the surface of the silicon heater was robust to the continual impact of the high pressure and high velocity jets of water, with no signs of erosion when filtered to 2 µm.

6.6. Chapter Summary

In Chapter 6, the effectiveness of microjet cooling was demonstrated through experimental and numerical analysis of the integrated heater. Micro-Raman thermography was used to scan the surface temperature profile of the device in the horizontal and vertical directions with 1 µm spatial resolution and a 5 µm step size showing strong agreement with the numerical model. Peak temperature measurements and additional thermal scans were performed at varying heat fluxes and built additional confidence in the numerical model. The heat transfer coefficient dependence on velocity was explored, noting the tradeoff with higher system pressures and ideal pumping powers. A simplified thermal resistance model from junction to inlet temperature was used to understand the two contributions of conductive and convective thermal resistance, as well as enabling a direct comparison with the work of Brunschwiler et al. [54]. Lastly, an extended 1000-hour testing was used to address common (practical) concerns with microjet impingement including the effects of microjet clogging and backside erosion.

7. Conclusions

Moore's Law, which posits that the number of transistors on integrated circuits doubles every two years, has accurately described developments in Si fabrication technologies since 1965. Constraints imposed by material and economic factors suggest that Moore's Law may be approaching an end. A new class of semiconductors, including gallium nitride (GaN), offer electrical properties that enable higher power and higher frequency operation than their Si counterparts. GaN high electron mobility transistors (HEMTs) in RF power amplifiers offer unmatched power densities of 40 W/mm. The increased power densities create a significant challenge in managing the heat generated in the small area footprints of the devices. Reducing the operating temperature in these devices improves both performance and reliability. Traditional thermal management techniques such as natural convection cooling with air are not suitable for removing the quantity of heat generated at these length scales. Embedded liquid cooling, directly on the backside of the electronic device, offers improved device performance.

7.1. Thesis Summary

In this thesis, a microjet cooler was fabricated using standard silicon micro-fabrication technologies. The design of the cooler was based on insight from previous experimental studies that considered the impact of jet diameter, pitch, and standoff distance on heat transfer performance. The microjet cooler was then bonded to an integrated heater, designed to match the power dissipation geometry of a HEMT. A fully conjugate numerical model of the fluid dynamics and heat transfer was used to visualize the fluid flow within the microjet assembly and predict the heat transfer coefficient at varying flow rates and power levels. The predicted heat transfer coefficients exceeded 350 kW/m^2-K.

An experimental setup probed the hydraulic performance by measuring the pressure drop across the microjet array, which was then used to calculate the ideal pumping power required for the system. The experimental setup was interfaced with a micro-Raman thermography setup offering 1 μm spatial resolution. The temperature of the device was measured using both the linewidth broadening and peak shift methods. Two-dimensional temperature scans of the integrated heater device were taken at various power levels with jet impingement cooling on the backside. Microjet cooling was demonstrated on a device of a heat flux of 6680 W/cm^2 and a temperature rise of 59 °C.

Practical concerns including microjet orifice clogging and backside erosion were also answered through completion of a 1000-hour extended lifetime test. Continuous monitoring of the pressure drop and total flow rate in the system and inspection of the microjet orifices before and after the testing indicated that microjet clogging did not occur. Additionally, inspection of the backside of the device (using SEM

imaging) after 1000 hours of runtime demonstrated that backside erosion of the silicon substrate was insignificant.

7.2. Future Work

Future work in this program's demonstration of microjet cooling include bonding the microjet array to a GaN HEMT and measuring the impact of cooling on RF performance, such as gain and total output power. The impact of microjet cooling on this HEMT device would also benefit from micro-Raman temperature measurements with and without microjet cooling. A useful performance comparison would show the HEMT output power profile and operating temperature of the HEMT device for both the microjet and commercial cold plate approaches. This study would explicitly demonstrate the need for using microjets.

Although the impact of geometrical factors, including jet diameter, pitch, and standoff, of microjet arrays has been explored in previous works, there are still design features that need to be considered before implementation. Flow visualization studies showed the effect of cross flow, where the adjacent jets interacted before impact with the wall. Design improvements, whether performed using the numerical model or in experiments, could minimize this effect with improved effluent routing or jet pitch. Another area to be explored before implementation is the selection of fluidic equipment, such as hosing, connections, and pumps, to reduce the Size, Weight, and Power (SWaP) of the system.

The two primary thermal resistances from the junction temperature to the inlet fluid are conduction through the substrate and convection with the liquid. The conduction resistance is governed by the thickness and thermal conductivity of the substrate material. The conduction term can be reduced by decreasing the substrate thickness to a minimum, while balancing the thermal spreading and structural benefits of an increased thickness. The thermal conductivity of the material (k = 150 W/m-K for Si) can be improved by maturing fabrication technologies for 4H-SIC (k = 380 W/m-K) and diamond (k = 2000 W/m-K).

Micro-Raman thermography offers a powerful analysis tool for understanding both heat generation in high power-density devices and the effectiveness of thermal management systems. Micro-Raman is especially useful in the analysis of GaN HEMTs because of the multiple Raman peaks available. Bagnall et al. offered physical insights into the peak shifts due to the effects of strain, electric field, and temperature. These insights could be incredibly useful in understanding the failure mechanisms within GaN HEMTs. Exploration of the Raman signatures of other materials could offer similar information regarding temperature, stress, and electric field for these materials during operation. Additional improvements in the experimental setups could improve the spatial resolution to the order of 100 nm. One improvement is an optical method known as the solid immersion lens (SIL) technique, where a lens with the same refractive

index as the material being measured (n = 2.4 for GaN) is attached to the device itself. The SIL technique has shown improved lateral resolutions of 150 nm and axial resolutions of 500 nm [82]. Another approach to improve spatial resolution is to use microparticles with a strong and temperature sensitive Raman response for in situ particle or thin film experiments. This technique has been demonstrated using anatase TiO_2 microparticles with a spatial resolution of 280 nm [83].

Micro-Raman thermography, despite offering higher spatial and temporal resolution than competing technologies, is not widely used due to the cost and complexity of micro-Raman systems. Commercial micro-Raman systems currently cost approximately $250,000, and they cannot be customized for optimal space for electrical probes and heating stages. The work in this thesis benefited greatly from a free-space micro-Raman system developed by a previous DRL member, Dr. Kevin Bagnall. Widespread adoption of this micro-Raman thermography requires refinement of the experimental setup and additional discussions on the capabilities and limitations of the technique.

Bibliography

[1] A.L. Moore and L. Shi, “Emerging challenges and materials for thermal management of electronics”, *Materials Today*, vol. 17, pp. 163-174, May 2014.

[2] R. Cavin, P. Lugli, V. Zhirnov, "Science and engineering beyond Moore's law", *Proc. IEEE Special Centennial Issue*, vol. 100, pp. 1720-1749, 2012.

[3] H. Bu, “5 nm transistors inching their way into chips.” IBM Think Blog, June 5, 2017. https://www.ibm.com/blogs/think/2017/06/5-nanometer-transistors/

[4] A. N. Smith, J. P. Calame, "Impact of thin film thermophysical properties on thermal management of wide bandgap solid-state transistors", *Int. J. Thermophys.*, vol. 25, no. 2, pp. 409-422, Mar. 2004.

[5] R. Pengelly, S. Wood, J. Milligan, S. Sheppard, W. Pribble, "A review of GaN on SiC high electron-mobility power transistors and MMICs", *IEEE Trans. Microw. Theory Tech.*, vol. 60, no. 6, pp. 1764-1783, Jun. 2012.

[6] J. P. Calame, R. E. Myers, S. C. Binari, F. N. Wood, M. Garven, "Experimental investigation of microchannel coolers for the high heat flux thermal management of GaN-on-SiC semiconductor devices", *Int. J. Heat Mass Transfer*, vol. 50, pp. 4767-4779, 2007.

[7] U. K. Mishra, L. Shen, T. E. Kazior, Y. F. Wu, "Gan-based RF power devices and amplifiers", *Proc. IEEE*, vol. 96, no. 2, pp. 287-305, Feb. 2008.

[8] K. R. Bagnall, Y. S. Muzychka, E. N. Wang, "Analytical Solution for Temperature Rise in Complex Multilayer Structures With Discrete Heat Sources", IEEE Trans. Components Packag. Manuf Technol., vol. 4, no. 5, pp. 817-830, 2014.

[9] M. Garven and J. P. Calame, “Simulation and optimization of gate temperatures in GaN-on-SiC monolithic microwave integrated circuits,” *IEEE Trans. Compon. Packag. Technol.*, vol. 32, no. 1, pp. 63–72, Mar. 2009.

[10] Y.-F. Wu, M. Moore, A. Saxler, T. Wisleder, P. Parikh, "40-W/mm double field-plated GaN HEMTs", *IEEE 64th Device Research Conference 2006 Conference Digest*, pp. 151-152.

[11] J. D. Albrecht, R. P. Wang, P. P. Ruden, M. Farahmand, K. F. Brennan, "Electron transport characteristics of GaN for high temperature device modeling", *J. Appl. Phys.*, vol. 83, no. 9, pp. 4777-4781, 1998.

[12] S. Nuttinck, E. Gebara, J. Laskar, H. M. Harris, "Study of self-heating effects temperature-dependent modeling and pulsed load-pull measurements on GaN HEMTs", *IEEE Trans. Microw. Theory Techn.*, vol. 49, no. 12, pp. 2413-2420, Dec. 2001.

[13] J. W. Lee, K. J. Webb, "A temperature-dependent nonlinear analytic model for AlGaN–GaN HEMTs on SiC", *IEEE Trans. Microw. Theory Tech.*, vol. 52, no. 1, pp. 2-9, Jan. 2004.

[14] J. Ditri, R. Cadotte, D. Fetterolf, and M. McNulty, “Impact of microfluidic cooling on high power amplifier RF performance,” in *Proc.15th IEEE Intersoc. Conf. Thermal Thermomech. Phenomena Electron.Syst. (ITherm)*, Las Vegas, NV, USA, 2016, pp. 1501–1504.

[15] J. A. del Alamo et al., "GaN HEMT reliability", *Microelectronics reliability*, vol. 49, pp. 1200-1206, 2009.

[16] T. Ohki, T. Kikkawa, Y. Inoue, M. Kanamura, N. Okamoto, K. Makiyama, K. Imanishi, H. Shigematsu, K. Joshin, and N. Hara, "Reliability of GaN HEMTs: Current status and future technology", *Proc. IEEE Int. Rel. Phys. Symp.*, pp. 61-70, Apr 2009.

[17] J. Joh, J. A. del Alamo, "Mechanisms for electrical degradation of GaN high electron mobility transistors", *IEDM Tech. Dig.*, pp. 415-418, 2006.

[18] D. Marcon et al., "A comprehensive reliability investigation of the voltage- temperature- and device geometry-dependence of the gate degradation on state-of-the-art GaN-on-Si HEMTs", *Proc. IEEE IEDM*, pp. 1-20, Jan 2010.

[19] N. Killat, T.-M. Chou, U. Chowdhury, J. Jimenez, M. Kuball, "Temperature assessment of AlGaN/GaN HEMTs: A comparative study by Raman electrical and IR thermography", Proc. IEEE Int. Rel. Phys. Symp., pp. 528-531, 2010.
[20] J. D. Blevins, G. D. Via, A. Bar-Cohen, and A. Sivananthan, "Developing a new thermal paradigm for gallium nitride (GaN) device technology", in *Proc. Compound Semicond. Mantech. Conf.*, Miami, FL, USA, May 2016, pp. 141-146.
[21] D. B. Tuckerman, R. F. W. Pease, "High-performance heat sinking for VLSI", *IEEE Electron Device Lett.*, vol. 2, no. 5, pp. 126-129, May 1981.
[22] S.G. Kandlikar, S. Colin, Y. Peles, S. Garimella, R.F. Pease, J.J. Bradner, D.B. Tuckerman, "Heat Transfer in Microchannels-2012 Status and Research Needs", *Journal of Heat Transfer*, vol. 135, pp. 091001-1, 2012.
[23] F. P. Incropera, *Liquid Cooling of Electronic Devices by Single-Phase Convection*, 1st ed. New York, NY, USA: Wiley-Interscience, 1999.
[24] M. K. Sung and I. Mudawar, "Single-Phase and Two-Phase Hybrid Cooling Scheme for High-Heat-Flux Thermal Management of Defense Electronics," *ASME J. Electron. Packag.*, vol. 131 , p. 021013, Jun. 2009.
[25] S. J. Kim, I. C. Bang, J. Buongiorno, and L.W. Hu, "Surface wettability change during pool boiling of nanofluids and its effect on critical heat flux," *International Journal of Heat and Mass Transfer*, vol. 50, pp. 4105-4116, Sep. 2007.
[26] S.M. You and J. H. Kim, "Effect of nanoparticles on critical heat flux of water in pool boiling heat transfer," *Applied Physics Letters*, vol. 83, pp. 3374-3376, Oct. 2003.
[27] R. Chen, M. Lu, et al. "Nanowires for Enhanced Boiling Heat Transfer," *Nano Letters*, vol. 9, pp. 548-553, Jan. 2009.
[28] S. Adera, D. Antao, R. Raj, E. N. Wang, "Design of micropillar wicks for thin-film evaporation", *Int. J. Heat Mass Transf.*, vol. 101, pp. 280-294, Oct. 2016.
[29] J. D. Sircar et al., "High Heat Flux Evaporation from Nanoporous Silicon Membranes", *Fifteenth Intersociety Conference on Thermal and Thermomechanical Phenomena in Electronic Systems (ITherm)*, 2016.
[30] T. Zhang, T. Tong, Y. Peles, R. Prasher, et al. "Ledinegg instability in microchannels," *International Journal of Heat and Mass Transfer*, vol. 52, pp. 5661-5674, Sep. 2009.
[31] S. Kakac and B. Bon, "A Review of two-phase flow dynamic instabilities in tube boiling systems," *International Journal of Heat and Mass Transfer*, vol. 51, pp. 399-433, Dec. 2007.
[32] T.R. Salamon, "Challenges and Opportunities for thermal management of information and communications technologies equipment: a telecommunications perspective", *IEEE Trans. on Comp., Pack., and Manu. Tech.*, vol. 7, no. 8, pp. 1212-1227, Aug. 2007.
[33] A. Bar-Cohen, Joseph J. Maurer, Abirami Sivananthan, "Near-junction microfluidic thermal management of RF power amplifiers", *2015 IEEE International Conference on Microwaves Communications Antennas and Electronic Systems (COMCAS)*, 2015.
[34] A. Bar-Cohen, J. J. Maurer, and J. G. Felbinger, ''DARPA's intra/interchip enhanced cooling (ICECool) Program,'' in Proc. CS MANTECH Conf., New Orleans, LA, USA, May 2013, pp. 171–172.
[35] V. Gambin, B. Poust, D. Ferizovic, M. Watanabe, and G. Mandrusiak, "Impingement cooled embedded diamond Multiphysics co-design," in *Proc.15th IEEE Intersoc. Conf. Thermal Thermomech. Phenomena Electron.Syst. (ITherm)*, Las Vegas, NV, USA, 2016, pp. 1518-1529.
[36] D. Altman, A. Gupta, and M. Tyhach, "Development of a diamond microfluidics-based intra-chip cooling technology for GaN", in *Proc. ASME Internat. Tech. Conf. and Exhibition on Packaging and Integration of Electronic and Photonic Microsystems (InterPACK)*, San Francisco, CA, USA, 2015, pp. 1-7.
[37] J. Ditri, M. McNulty, and S. Igoe, "Embedded Microfluidic Cooling of High Heat Flux Electronic Components," in *Lester Eastman Conference on High Performance Devices*, 2014, pp. 1-4.

[38] J. Ditri, J. Hahn, R. Cadotte, M. McNulty, and D. Luppa, “Embedded cooling of high heat flux electronics utilizing distributed microfluidic impingement jets,” in *Proc. ASME Internat. Tech. Conf. and Exhibition on Packaging and Integration of Electronic and Photonic Microsystems (InterPACK)*, San Francisco, CA, USA, 2015, pp. 1-10.
[39] J. Joh et al., "Measurement of channel temperature in GaN high-electron mobility transistors", *IEEE Trans. Electron Devices*, vol. 56, no. 12, pp. 2895-2901, Dec. 2009
[40] M. Kuball and J. W. Pomeroy, "A review of Raman thermography for electronic and optoelectronic device measurement with submicron spatial and nanosecond temporal resolution," *IEEE Trans. Device and Materials Reliability*, vol. 16, no. 4, pp. 667-684, Dec. 2016.
[41] K. Maize, G. Pavlidis, E. Heller, *et al.*, “High resolution thermal characterization and simulation of power AlGaN/GaN HEMTs using micro-Raman thermography and 800 picosecond transient thermoreflectance imaging,” *Proc. IEEE Compound Semiconductor Integrated Circuit Symposium*, La Jolla, CA, 2014, pp. 1-8.
[42] T. Beechem, S. Graham, S. P. Kearney, et al., "Invited article: Simultaneous mapping of temperature and stress in microdevices using micro-Raman spectroscopy," *Review of Scientific Instruments*, vol. 78, p. 061301, Jun. 2007.
[43] N. Zuckerman and N. Lior, “Impingement Heat Transfer: Correlations and Numerical Modeling,” *Journal of Heat Transfer*, vol. 127, pp. 544-552, May 2005.
[44] J. Ferrari, N. Lior, and J. Slycke, “An evaluation of gas quenching of steel rings by multiple-jet impingement,” *Journal of Materials Processing Technology*, vol. 136, pp. 190-201, Jan. 2003.
[45] N. D. Francis and W. J. Wepfer, “Jet impingement drying of a moist porous solid,” *International Journal of Heat and Mass Transfer*, vol. 39, no. 9, pp. 1911-1923, Jul. 1995.
[46] B. Agostini, M. Fabbri, J. E. Park, L. Wojtan, J. R. Thome, and B. Michel, ‘‘State-of-the-Art of High Heat Flux Cooling Technologies,’’ Heat Transfer Engineering, vol. 28, no. 4, pp. 258–281, 2007.
[47] S. V. Garimella, R. A. Rice, "Confined and submerged liquid jet impingement heat transfer", *J. Heat Transf.*, vol. 117, pp. 871-877, 1995.
[48] D.J. Womac, S. Ramadhyani , and F.P. Incopera, “Correlating equations for impingement cooling of small heat sources with single circular liquid jets”, *J. Heat Transfer*, vol. 115, no. 1, pp. 106–115, Feb. 1993.
[49] E.A. Browne, G.J. Michna, M.K. Jensen, and Y. Peles, “Microjet array single-phase and flow boiling heat transfer with R134a,” *International Journal of Heat and Mass Transfer*, vol. 53, pp. 5027-5034, 2010.
[50] B. A. Lindeman, T. A. Shedd, "Comparison of empirical correlations and a two-equation predictive model for heat transfer to arbitrary arrays of single-phase impinging jets", *Int. J. Heat Mass Transf.*, vol. 66, pp. 772-780, Nov. 2013.
[51] H. Martin, "Heat and mass transfer between impinging gas jets and solid surfaces", *Adv. Heat Transf.*, vol. 13, pp. 1-60, 1977.
[52] D.J. Womac, F.P. Incopera, and S. Ramadhyani, “Correlating equations for impingement cooling of small heat sources with multiple circular liquid jets”, *J. Heat Transfer*, vol. 116, no. 2, pp. 482–486, May 1994.
[53] M. Fabbri and V. K. Dhir, “Optimized Heat Transfer for High Power Electronic Cooling Using Arrays of Microjets,” *J. Heat Transfer*, vol. 127, no. 7, pp. 760–769, Nov. 2004.
[54] T. Brunschwiler, H. Rothuizen, M. Fabbri, U. Kloter, B. Michel, R.J. Bezama, and G. Natarajan, “Direct liquid jet-impingement cooling with micron-sized nozzle array and distributed return architecture, in *Proc.10th IEEE Intersoc. Conf. Thermal Thermomech. Phenomena Electron.Syst. (ITherm)*, San Diego, CA, USA, 2006, pp. 196– 203.
[55] A.J. Robinson and E. Schnitzler. “An experimental investigation of free and submerged miniature liquid jet array impingement heat transfer,” *Experimental Thermal and Fluid Sciences*, vol. 32, no. 1, pp. 1-13, Oct. 2007.
[56] E. A. Browne, G. J. Michna, M. K. Jensen, and Y. Peles, “Experimental Investigation of Single-Phase Microjet Array Heat Transfer,” *Journal of Heat Transfer*, vol. 132 , p. 041013, Apr. 2010.

[57] G. J. Michna, E. A. Browne, Y. Peles, and M. K. Jensen, "The effect of area ratio on microjet array heat transfer." *International Journal of Heat and Mass Transfer*, vol. 54, pp. 1782-1790, 2011.
[58] K. R. Bagnall, "Multiphysics Characterization of GaN HEMTs via Micro-Raman Spectroscopy." *PhD Dissertation*, May 5, 2017.
[59] K. R. Bagnall, "Device-level Thermal Analysis of GaN-based Electronics." *Master's Thesis*, May 10, 2013.
[60] A. Manoi et al., "Time-dependent thermal crosstalk in multifinger AlGaN/GaN HEMTs and implications on their electrical performance", *Solid State Electron.*, vol. 57, no. 1, pp. 14-18, Mar. 2011.
[61] Zuckerman, N. and Lior, N., "Jet impingement: physics, correlation, and numerical modelling," *Advances in Heat Transfer*, Vol. 39 (2006), pp. 565-631.
[62] G. M. Carlomagno and A. Ianiro. "Thermo-fluid-dynamics of submerged jets impinging at short nozzle-to-plate distance: A review.," *Experimental Thermal and Fluid Science*, vol. 58, pp. 15-35, 2014.
[63] K. J. McNaughton, C. G. Sinclair, "Submerged Jets in Short Cylindrical Flow Vessels", *J. Fluid Mech.*, vol. 25, no. 2, pp. 367-375, 1966.
[64] W. Frie, "Which Turbulence Model Should I Choose for My CFD Application?", *COMSOL Blog*, Jul. 2017
[65] B. A. Lindeman, T. A. Shedd, "Predictive model for heat transfer performance of oblique and normally imping jet arrays", *Int. J. Heat Mass Transf.*, vol. 62, pp. 612-619, 2013.
[66] S. Kline and F. Mcclintock, "Describing Uncertainties in Single-Sample Experiments," *Mechanical Engineering*, vol. 75, pp. 3-8, 1953.
[67] T. Jankowski, E. Schrierer, C. Prenger, and S. Ashworth, "A Series Pressure Drop Representation for Flow Through Orifice Tubes." *Journal of Fluids Engineering,* vol. 130, p. 051204, 2008.
[68] A. Sarua, H. Ji, M. Kuball, M. J. Uren, T. Martin, K. P. Hilton, R. S. Balmer, "Integrated micro-Raman/infrared thermography probe for monitoring self-heating in AlGaN/GaN transistor structures", *IEEE Trans. Electron Devices*, vol. 53, no. 10, pp. 2438-2447, Oct. 2006.
[69] S. P. Kearney, L. M. Phinney, and M. S. Baker, "Spatially resolved temperature mapping of electro-thermal actuators by surface Raman scattering," *J. Microelectromech. Syst*., vol. 15, no. 2, pp. 314–321, Apr. 2006.
[70] K. R. Bagnall, E. A. Moore, S. C. Badescu, L. Zhang, and E. N. Wang, "Simultaneous measurement of temperature, stress, and electric field in GaN HEMTs with micro-Raman spectroscopy," *Review of Scientific Instruments*, vol. 88, p. 113111, Nov. 2017.
[71] T. Beechem, A. Christensen, S. Graham, and D. Green, "Micro-Raman thermometry in the presence of complex stresses in GaN devices," *J. Appl. Phys*., vol. 103, p. 124501 Jun. 2008.
[72] C.V. Raman and K.S. Krishnan, "A New Type of Secondary Radiation", Nature 121, 31 March 1928.
[73] T. E. Beechem and J. R. Serrane, "*Raman thermometry of microdevices*: *comparing methods to minimize error*," Spectroscopy vol. 26, no. 11, pp. 36–44, 2011.
[74] M. Kuball,M, J. M. Hayes, M. J. Uren, I. Martin, J. C. Birbeck, R. S. Balmer, and B. T. Hughes, "Measurement of Temperature in Active High-Power AlGaN/GaN HFETs Using Raman Spectroscopy," *IEEE Electron Device Letters*, vol. 23, no. 1, 7-9, 2002.
[75] T. Batten, J. W. Pomeroy, M. J. Uren, T. Martin, M. Kuball, "Simultaneous measurement of temperature and thermal stress in AlGaN/GaN high electron mobility transistors using Raman scattering spectroscopy", *J. Appl. Phys.*, vol. 106, no. 9, pp. 094509-1-094509-4, Nov. 2009.
[76] S. Choi, E. R. Heller, D. Dorsey, R. Vetury, S. Graham, "Thermometry of AlGaN/GaN HEMTs using multispectral Raman features", *IEEE Trans. Electron Devices*, vol. 60, no. 6, pp. 1898-1904, Jun. 2013.
[77] K. R. Bagnall, C. E. Dreyer, D. Vanderbilt, and E. N. Wang, "Electric field dependence of optical phonon frequencies in wurtzite GaN observed in GaN high electron mobility transistors," *Journal of Applied Physics*, vol. 120, p. 155104, Oct. 2016.

[78] T. R. Hart, R. L. Aggarwal, and B. Lax, “Temperature dependence of Raman scattering in silicon,” *Phys. Rev. B Solid State*, vol. 1, no. 2, pp. 638–642, Jan. 1970.
[79] M. R. Abel, T. L. Wright, W. P. King, S. Graham, "Thermal metrology of silicon micro-structures using Raman spectroscopy", *IEEE Transactions Components and Packaging Technologies*, vol. 30, no. 2, pp. 200-208, June 2007.
[80] W. Escher, T. Brunschwiler, B. Michel, D. Poulikakos, "Experimental investigation of an ultrathin manifold microchannel heat sink for liquid-cooled chips", *J. Heat Transf.*, vol. 132, no. 8, pp. 081402-1-081402-10, 2010.
[81] N. Kaminski, O. Hilt, "SiC and GAN devices—Wide bandgap is not all the same", *IET Circuits Devices Syst.*, vol. 8, no. 3, pp. 227-236, May 2014.
[82] J. W. Pomeroy and M. Kuball, “Solid immersion lenses for enhancing the optical resolution of thermal and electroluminescence mapping of GaN-on-SiC transistors,” *J. Appl. Phys.*, vol. 118, no. 14, pp. 144501-1–144501-9, Oct. 2015.
[83] N. Lundt, S. T. Kelly, T. Rödel, B. Remez, A. M. Schwartzberg, A. Ceballos, C. Baldasseroni, P. A. F. Anastasi, M. Cox, F. Hellman, S. R. Leone, M. K. Gilles, "High spatial resolution Raman thermometry analysis of TiO2 microparticles", *Rev. Sci. Instrum.*, vol. 84, no. 10, 2013.

Appendix A: Detailed Solidworks Drawing of Interface Plate

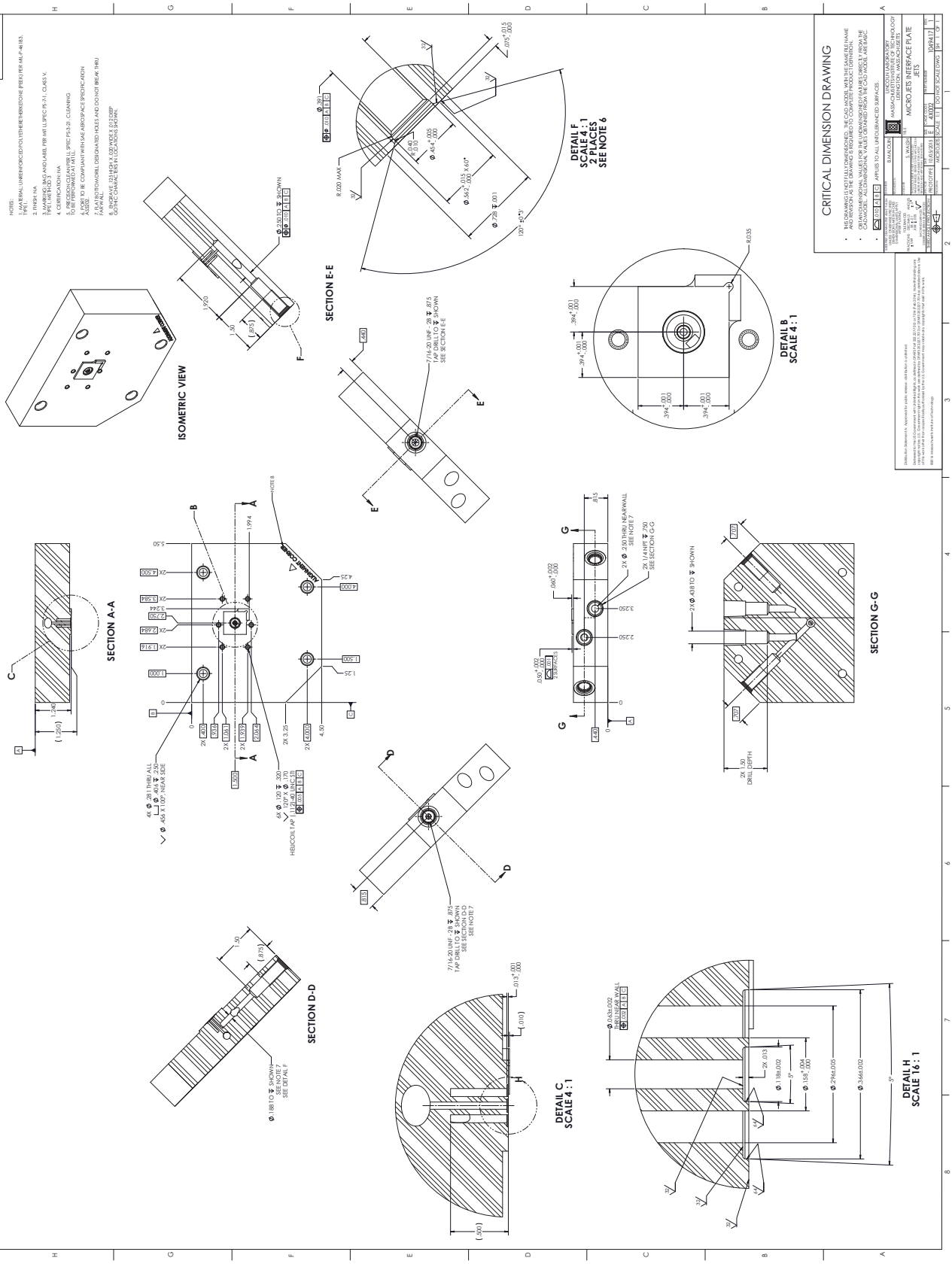

Appendix B: Detailed Solidworks Drawing of Cover Plate

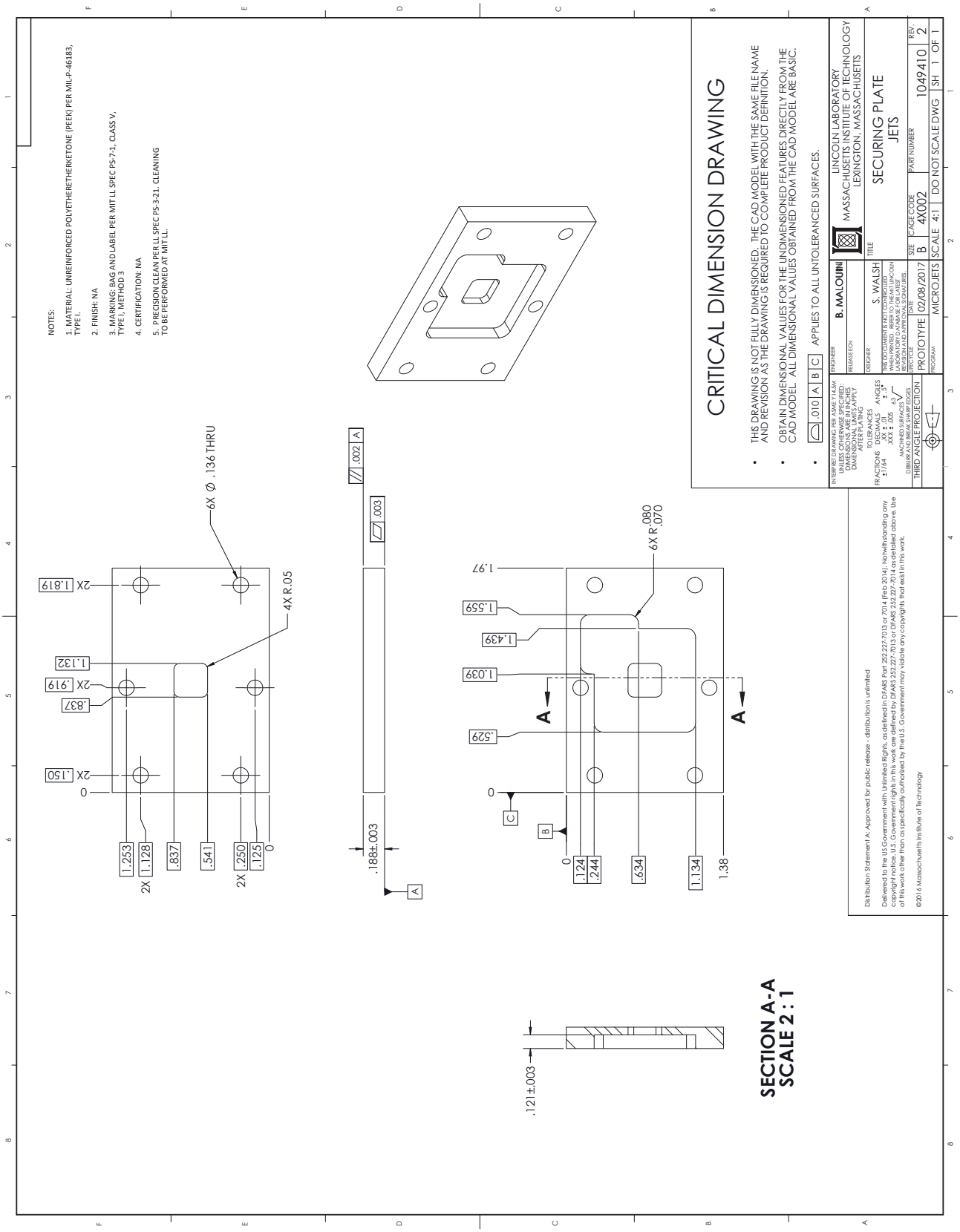

Appendix C: Sample Matlab Code of Temperature Analysis

```
% Stephen Walsh 9 April 2018
% Fit the temperature dependent Raman peak of Silicon
clear;clc;
% Read in the experimental data file with peak position, linewidth and x position
data= xlsread('08092017_RamanExpMap.xlsx');

% Create arrays for peak position, peak std, linewidth, linewidth std, spatial position
muSiAvg = data(4:44,9);
muSiStdev = data(4:44,10);
fwhmSiAvg= data(4:44,11);
fwhmRef= 2.814;
xposition = data(4:44,7);

% Read in the reference Raman peak position
muSiReferencePeak = data(1,9);

% Read in the Model Data
ModelData= xlsread('03262018_CFDXSlice.xlsx','Map1');
Modelxposition = ModelData(1:860,12);
ModelTemp = ModelData(1:860,13);

% From the Si calibration analysis
SiTempCoeff = -0.0235;
SiTempCoeffStdev = 3.33e-04;
B=8.51e-06;
C=9.18e-03;

% Calculate the temperature from the peak shift, calculate uncertainty sqrt[ ((w-wo)/A^2 dA)^2 + ((1/A)dw)^2  ]
Temperature = 1/SiTempCoeff*(muSiAvg-muSiReferencePeak);
TemperatureStdev = sqrt(((muSiAvg-
muSiReferencePeak)/SiTempCoeff.^2*SiTempCoeffStdev).^2+(muSiStdev/SiTempCoeff).^2);

%Linewidth Temp Cal
TemperatureLinewidth1= abs((-C+sqrt(C^2-4*B*(fwhmSiAvg-fwhmRef)))/(2*B));
% TemperatureLinewidth2= (-C-sqrt(C^2-4*B*(fwhmSiAvg-fwhmRef)))/(2*B);

figure (1)
plot(xposition,Temperature,'o','MarkerEdgeColor','b','MarkerSize',5,'LineWidth',1)
hold on;
plot(xposition,TemperatureLinewidth1,'x','MarkerEdgeColor','k','MarkerSize',6,'LineWidth',1)
plot(Modelxposition,ModelTemp,'-r','LineWidth',1);
set(gca,'Box','on','FontSize',15);
legend('Peak Based','Linewidth Based','Model','Location','southwest');
xlabel('X Position (\mum)');
ylabel('Temperature Rise (^{\circ}C)');
axis([0 200 0 50]);
print(figure(1),'Lifetime','-dpng','-r600')
```

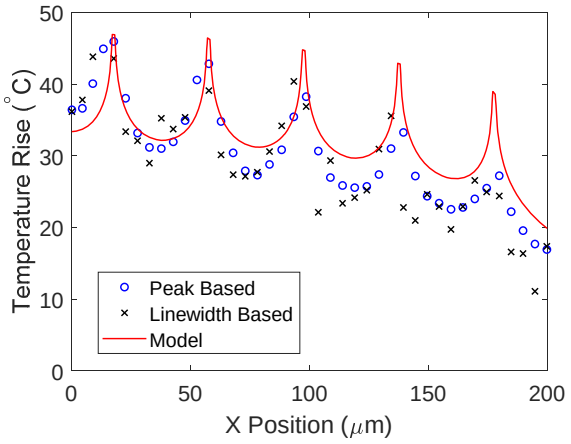

Published with MATLAB® R2017b